Near-field Multi-slice Ptychography

Ziyang Hu

A thesis submitted in partial fulfilment of the requirements for the degree of Doctor of Philosophy

The University of Sheffield
Faculty of Engineering
Department of Electronic & Electrical Engineering

Submission Date

August 2024

Declaration

I, Ziyang Hu, hereby declare that the work presents in this thesis is my own original work, except where clearly indicated and reference. I am aware of the University's Guidance on the Use of Unfair Means (www.sheffield.ac.uk/ssid/unfair-means). This work has not previously been presented for an award at this, or any other, university.

Parts of Chapter 2, 3, 4 and 5 are adapted from the following publications, with permission granted from © Optical Society of America:

Ziyang Hu, Yiqian Zhang, Peng Li, Darren Batey, and Andrew Maiden, "Near-field multi-slice ptychography: quantitative phase imaging of optically thick samples with visible light and X-rays," Opt. Express 31, 15791-15809 (2023)

Ziyang Hu, Yiqian Zhang, and Andrew Maiden, "Optical slicing via near-field multi-slice ptychography microscopy," Opt. Letter, to be published (2024)

Ziyang Hu

August 2024

Abstract

Ptychography is a form of computational microscopy that has risen to prominence in the past 20 years. Despite achieving record breaking resolution[1], Depth-of-Field (DoF) is a significant limiting factor for the technique. Recently, scientists have pioneered a propagation-based computational three-dimensional (3D) imaging method to break through the DoF limit, called "multi-slice ptychography", which has now been implemented in both far-field and Fourier ptychography configurations at a wide range of wavelengths [2] [3] [4]. This work explores a third implementation of multi-slice ptychography operating not in the Fourier or far-field configuration but in the optical near-field. The main aim of this work is to combine near-field ptychography and multi-slice ptychography for the first time, to address the multi-scattering effect that limits ptychography's DoF, in order to maximise the sample volume for ptychographic imaging.

This thesis introduces Near-field Multi-slice Ptychography (NMP) through both theoretical and experimental investigations in both X-ray and optical applications. The work started with modification of the reconstruction framework, the multi-slice algorithm called 3PIE [2], which is then implemented for NMP. In addition, the proof-of-principle optical bench experiments for NMP was demonstrated using a lensless cone-beam configuration, showing the feasibility of the approach.

Subsequently, NMP was successfully demonstrated with coherent hard X-rays at the synchrotron facility, achieving sub 100 nm lateral resolution, 300 µm depth resolution and extending the DoF to image samples exceeding 1 mm thickness. The validation of NMP in the hard X-ray regime paves the way for high-resolution large volume imaging and the potential to combine with tomographic reconstruction in future research.

Furthermore, the development of an optical near-field multi-slice ptychography microscope system is presented, where the DoF is extended by a factor of 10s, compared to conventional microscopy methods. The work demonstrates the potential of NMP as a new label-free imaging tool for research in biological science for transmissive samples, as an alternative to fluorescence-based optical sectioning methods such as confocal microscopy.

Acknowledgement

First of all, I would like to thank my supervisor Dr. Andrew Maiden, for your patience, support and guidance over the past few years. I have thoroughly enjoyed our discuss on research topic, experiment work in our basement optics lab and at the diamond light source and of course the conference trip in Los Angeles and touring around the Santa Monica and walk of fame for “science”!

I would also like to thank my colleague Dr. Yiqian Zhang, Dr. Wenjie Mei, Dr. Shenbo Yo and Dr. Fredrick Allars for the invaluable discussions and helps throughout my PhD journey. In addition, I would like to thank the beamline scientist Dr. Batey Darren and Dr. Peng Li in the DLS I13-1 for the technical support over the busy weeks. I would like to thank Institution of Pure and Applied Math, University California Los Angeles and National Science Foundation for hosting and funding me to attend the computational microscopy long programme, which brought me a lot more “sunshine” and unique experiences for my research.

I would like to express my gratitude to my parents Hong Yang and Kunshu Hu, for the unconditional support during the 11 years journey I have been away from home on the other side of the world.

Last but not least, to my lover, my best friend, also my family, Adam Hudson. Thank you for always being patient and supportive to me and give me a home where I feel happy, safe, and loved. Sorry that you had to deal with an “emotionally unstable” PhD student over the past few years! I cannot wait to start a new life chapter with you.

Publication

Journal papers

Z. Hu, Y. Zhang, A. Maiden “Optical slicing via near-field multi-slice ptychography,” (Opt. Letter, accepted for publication, 2024)

Z. Hu, Y. Zhang, P. Li, D. Batey, A. Maiden**,** "Near-field multi-slice ptychography: quantitative phase imaging of optically thick samples with visible light and X-rays," Opt. Express 31, 15791-15809 (2023)

H. Ya, **Z. Hu**, R. Saad. “Breaking Barriers: Promoting Inclusive Research Culture among PGR Engineering Students,” Exchanges: The Interdisciplinary Research Journal (accepted, 2024)

White paper: “Computational Microscopy” (IPAM Long Program, Fall 2022), https://www.ipam.ucla.edu/news/white-paper-computational-microscopy/

Conference presentation and proceedings

A. Maiden, **Z. Hu,** Y. Zhang. “Near-Field Multi-Slice Optical Ptychography,” *Optica Imaging Congress 2024*, (Optica Publishing Group, 2024)

Z. Hu, et al. “Optical near-field multi-slice ptychography,” Institution Pure Applied Math (IPAM), University California Los Angeles, June 2024

Z. Hu, et al. "Near-field multislice ptychography – demonstration using visible light and x-ray experiment," in *Microscience Microscopy Congress 2023*, Technical Digest Series (MMC, 2023).

Z. Hu, “Near-field multi-slice ptychography” (IPAM Long Program, Seminar series, Fall 2022).

Z. Hu, "Step Size Influence on Defocused Beam Ptychography," in *Imaging and Applied Optics Congress 2022 (3D, AOA, COSI, ISA, pcAOP)*, Technical Digest Series (Optica Publishing Group, 2022), paper CTh3C.3.

List of Abbreviations

Abbreviation	Meaning
ADMM	Alternating Directions Method of Multipliers
ASF	Amplitude Spread Function
CCD	Charge-coupled Device
CDI	Coherent Diffractive Imaging
DM	Difference Map
DoF	Depth of Field
ePIE	Fextend Ptychographic Iterative Engine
ER	Error Reduction
FFT	Fast Fourier Transform
FMP	Fourier Multi-slice Ptychography
FoV	Field of View
FST	Fresnel Scaling Theorem
GS	Gerchberg-Saxton
GUI	Graphical User Interface
ML	Maximum Likelihood
MLB	Multi-layer Born
NA	Numerical Aperture
NMP	Near-field Multi-slice Ptychography
NMPM	Near-field Multi-slice Ptychography Microscopy
OSA	Order Sorting Aperture
PIE	Ptychographic Iterative Engine
PSF	Point Spread Function
RAAR	Relaxed Averaged Alternating Reflections
rPIE	Regularised Ptychographic Iterative Engine
SSE	Sum of Squared Errors
WASP	Weighted Average of Sequential Projections

List of Contents

Introduction

In the past few centuries, lens-based microscopy techniques have continuously evolved and played an indispensable role in the advanced modern scientific research, allowing scientists to explore the world from the milli-scale down to sub-ångström resolution. Imaging with lenses becomes increasingly difficult below this resolution due to imperfect optical components at very short wavelengths (X-rays) and in the electron microscope [5] [6] [7]. While aberration correction techniques have significantly improved the performance of microscopic imaging, particularly in electron microscopy, fundamental limitations such as photon scattering, depth of field constraints, and radiation damage continue to pose challenges for achieving high-resolution imaging. To image beyond the limits of these imperfect optics, in the late 1990s a breakthrough in microscopy called Coherent Diffractive Imaging (CDI) was developed, where the diffraction pattern of an object can be directly measured without lenses and transformed into a high-resolution image [8]. This method overcomes the phase problem, caused by the loss of phase information from the diffracted intensity measurement, by combining the coherent illumination with computational reconstruction algorithms. Ptychography, also known as scanning probe CDI, has been developed rapidly in the past 20 years. It is based on the phase retrieval reconstruction via overlapping diffraction patterns, that has further advanced the development of CDI [9] [10] [11]. Ptychography has distinguished itself from other CDI methods through the unique advantages [12]: it does not require a reference beam, is capable of super-resolution imaging, and is dose efficient. Ptychography has been widely implemented in most of the synchrotron facilities as an advanced imaging technique. In optical regime, ptychography has been adopted for the application of biomedical research, especially with the development of Fourier ptychography, which enables imaging with both high resolution and large FoV [13]. More recently, electron ptychography achieved record-breaking resolution at sub-ångström level [1].

Despite the achievement in spatial resolution, there remains a strong desire to obtain three-dimensional (3D) information of a sample for research from biological to nano techniques. Conventionally, tomography is one non-invasive solution to gather the 3D information of a sample [14] [15] [16]. By taking images of the sample from various angles using a rotational

method, a comprehensive 3D visualisation can be constructed by integrating those 2D projections. However, each 2D projection from tomography, along with other conventional 2D imaging systems, are constrained by the depth of field (DoF) limit, which describes the maximum extend of a sample thickness that can be resolved accurately along the beam propagation direction. If a sample falls within the acceptable DoF range, all the features of the sample remain in focus. However, the higher the target resolution, the thinner sample needs to be.

What is the solution to extend this DoF and allow us to "see" further into the sample without compromising resolution, or having to physically slice the sample?

One method to achieve 3D imaging and to extend DoF is optical sectioning. Most common optical sectioning methods rely on the excitation of specific fluorescent dyes on the specimen. The detector of the microscope will only focus and record a thin section of the sample, where the fluorescence is excited. The process is repeated at different depths across the sample to produce a series of in-focus images. Those images contain thin slices of the sample that can later be assembled into a 3D image and thereby extend DoF. Such imaging techniques includes confocal microscopy [17], multiphoton microscopy [18] and light sheet fluorescence microscopy [19].

In this thesis, a label-free optical slicing method called **Multi-slice Ptychography** is introduced to address the DoF problem [2]. Instead of the mechanical optical slicing approach, a thick sample is divided into multiple thin layers that are computationally reconstructed via a "multi-slice" propagation model. The reconstruction of each slice can be solved using an inverse multi-scattering back-propagation. Furthermore, another focus of this work is on **Near-field Ptychography**, a variation of conventional ptychography [20]. Instead of a confined probe, the full sample is illuminated by a structured beam, just like in in-line holography, therefore the benefits of field of view (FoV) and high degree of relaxation in experiment and scattering property are inherited. By combing the multi-slice approach with near-field ptychography, a new method call **Near-field Multi-slice Ptychography** (NMP) is proposed in the work, where the sample volume can be significantly extended both laterally and axially.

The proposed NMP method builds upon recent advances in near-field ptychographic and multi-slice imaging, addressing key limitations of existing ptychographic approach. Traditional ptychography relies on the single-slice approximation, limiting its ability to recover depth information from thick samples due to multiple scattering effects. Recent developments in multi-slice ptychography have improved depth sectioning but have primarily been implemented in far-field regime [2]. The main advantages of NMP compared to existing methods are:

- Unlike far-field multi-slice ptychography, which requires a tightly focused probe and small scan steps to achieve high-resolution imaging, NMP illuminates the full sample with structured near-field patterns. This enables a significantly larger FoV while maintaining high spatial resolution, making it ideal for imaging extended samples without sacrificing detail.
- Traditional multi-slice ptychography demands thousands of diffraction patterns due to the requirement of a confined probe. Whereas the full field illumination in NMP can significantly reduce the number diffraction patterns required while still achieving accurate 3D reconstructions. This leads to faster data collection and lower computational burden.
- The near-field implementation allows for reduced experimental complexity and sample misalignment as it eliminates the need of a confined probe, which can be critical in practical applications, especially in X-ray and electron imaging where precise control over experimental parameters is challenging.

The key contributions of this thesis are:

1. First demonstration of NMP in both optical and synchrotron X-ray facility: This work develops and experimentally validates a novel imaging technique that extends multi-slice ptychography to the near-field domain, enabling high-resolution, depth-resolved, large FoV phase imaging without physical sectioning.
2. Systematic optimisation of experimental configurations and reconstruction algorithms: This study investigates the optimisation between experimental parameters (e.g., probe structure, propagation distances, and step size) for

reconstruction quality, leading to improved robustness, accuracy, and scalability of NMP.

3. The synchrotron X-ray implementation of NMP achieves sub-100 nm resolution over a cubic millimetre sample volume, a scale previously unattainable due to X-ray scattering limitations. This method has the potential to enable nanoscale imaging of large biological samples for a wide range of applications. In neuroscience, it facilitates nanoscale imaging of brain tissue, enabling the study of intricate neural structures and their pathological changes over a thick volume. In correlative microscopy, it provides high-fidelity 3D phase images to guide targeted electron microscopy (EM) analysis, reducing the need for destructive sample preparation.

Chapter 1 starts with the background theory of Fourier transform and its discrete form. Then the mathematical framework for the wave propagation model for coherent X-ray imaging is introduced, followed by the Fresnel scaling theorem for cone-beam propagation geometry, implementation of the near-field propagator and the derivation of projection approximation. In the end of this chapter, the diffraction limit resolution is introduced.

Chapter 2 presents a historical review of coherent diffraction imaging methods. Then the recent development of ptychography is reviewed – both experimental work and the reconstruction algorithm with the emphasis of the implementation of near-field ptychography and the PIE family of algorithms. In addition, the implementation of some common experimental configurations for multi-slice ptychography and the implementation of multi-slice models are detailed.

The first result chapter, Chapter 3, starts with the modification and implementation framework of the 3PIE algorithm for a cone-beam near-field configuration. Following this is the experimental implementation and reconstruction results of lensless near-field multi-slice ptychography on an optical bench as an initial testing and simulation tool for the later X-ray experiments presented in Chapter 4.

Chapter 4 demonstrates two X-ray near-field multi-slice ptychography experiments using a coherent hard X-ray source at a synchrotron facility. This chapter starts with an overview of the I13 coherent branch at Diamond Light Source, where both experiments in this chapter were performed. The experiment configuration and the multi-slice reconstruction results for

first experiments are presented to show the successful implementation of X-ray NMP. Then the follow up X-ray NMP experiment with an alternative configuration explores further and shows the potential improvement in both lateral and depth resolution.

In the final result chapter, Chapter 5, the multi-slice ptychography is implemented with an optical microscopy system. This work starts with the introduction to the experimental configuration and additional modification of the 3PIE algorithm. The result section demonstrates the versatility of NMP and its potential as an optical slicing method and a 3D phase imaging tool for application on a wide range of biological samples.

The thesis concludes with a summary of the experimental work for NMP and the potential improvement building upon current work for the future application.

1. Background and theoretical framework

In this chapter, the mathematical theory and physical concepts directly associated to work presented in this thesis are summarised. The chapter begins with the exploration of the two-dimensional Fourier transform and its discrete form [21], which are critical tools for the digital implementation of wave propagation. This is followed by the revision of linear system theory and its application to linear imaging systems. Then the fundamentals of coherent X-ray imaging are introduced, based on the textbook written by D. Paganin [22], and in particular, the primary focus for this thesis is discussed - the "near-field" propagation and wavefront recovery using the so-called angular spectrum method. Additionally, Fresnel and Fraunhofer diffraction are discussed as the other two important free-space diffraction used in conventional coherent diffraction imaging methods. This chapter also includes the derivation of the Fresnel scaling theorem, as an important extension theorem for the near-field (Fresnel) paraxial propagation, highlighting its significance in establishing the geometric relationship between cone-beam and parallel-beam projections. Furthermore, the sampling and implementation requirements for the discrete near-field propagator are introduced [23] [24] [25]. Finally, two-dimensional multiplicative equation of a wave field interaction with matter is derived using the projection approximation [22], providing a mathematical framework that supports the subsequent chapters, and the Rayleigh resolution of diffractive imaging will be analysed [26].

1.1. Fourier transform and Fourier theorems

The Fourier transform reveals the relationship between the real-space (spatial) domain and the corresponding Fourier (frequency) domain of a signal [21]. An image can be seen as a 2D signal with real-space coordinate $g(x, y)$ and its corresponding frequency representation is denoted as $G(f_x, f_y)$, where (f_x, f_y) is the frequency domain coordinates,

$$G(f_x, f_y) = \iint g(x, y) \exp\left[-j2\pi(f_x x + f_y y)\right] dxdy\,. \tag{1.1}$$

The inverse Fourier transform essentially decomposes the original "image" into a sum of 2D orthogonal basis functions [21], where each of those basis function corresponds to a specific frequency component of the "image",

$$g(x,y) = \iint G(f_x, y_x) \exp\left[-j2\pi\left(f_x x + f_y y\right)\right] df_x df_y \,. \tag{1.2}$$

Eq. 1.1. and Eq. 1.2. can also be described in a direct formulation:

$$G(u,v) = \mathcal{F}\{g(x,y)\} \tag{1.3}$$

$$g(x,y) = \mathcal{F}^{-1}\{G(f_x, f_y)\}. \tag{1.4}$$

Some important Fourier theorems are summarised in **Table 1**.

Table 1: Summary of important Fourier theorems [21] [22]

Theorem	Formulation
Linearity	$\mathcal{F}\{Ag(x,y) + Bh(x,y)\} = A\mathcal{F}\{g(x,y)\} + B\mathcal{F}\{h(x,y)\}$
Similarity	$\mathcal{F}\left\{g\left(\frac{x}{a}, \frac{y}{b}\right)\right\} = \lvert ab\rvert G(af_x + bf_x)$
Shift	$\mathcal{F}\{g(x-a, y-b)\} = G(f_x, f_y)\exp\left[-j2(af_x + bf_y)\right]$
Convolution	$\mathcal{F}\left\{\iint g(u,v)h(x-u, y-v)dudv\right\} = G(f_x, f_y)H(f_u, f_v)$

The convolution of two signals in the spatial domain corresponds to the element-by-element multiplication of their Fourier transforms in the frequency domain. Mathematically, this is expressed as:

$$g(x,y) * h(u,v) \leftrightarrow G(f_x, f_y)H(f_u, f_v) \tag{1.5}$$

Where * denotes to the convolution operator.

An optical system can be modelled as a combination of basic functions and the Fourier transform of these individual or combined functions can be used as a convenient tool to model the corresponding diffraction limits. For instance, a signal $g_1(x_1, y_1)$ input through an

optical system S, results in the output signal g_2, which can be described by the system's response to the original input signal:

$$g_2(x_2, y_2) = S\{g_1(x_1, y_1)\}. \quad (1.6)$$

From the property of system linearity, this output of the system can then be decomposed into the sum of sub- impulse responses using superposition integral,

$$g_2(x_2, y_2) = \iint g_1(u, v)h(x_2, y_2; u, v)dudv\,. \quad (1.7)$$

Where h represents the impulse response of the system and it can be modelled as

$$h(x_2, y_2; u, v) = S\{\delta(x_1 - u, x_2 - v)\}. \quad (1.8)$$

Eq. 1.6. can be further simplified from space invariance property of a system, where

$$g_2(x_2 - u, y_2 - v) = S\{g_1(x_1 - u, y_1 - v)\}. \quad (1.9)$$

Therefore, the impulse response of the system is

$$h(x_2, y_2; u, v) = h(x_2 - u, y_2 - v). \quad (1.10)$$

Consequently, the system can be rewritten into the form of a convolution integral

$$g_2(x_2, y_2) = \iint g_1(u, v)h(x_2 - u, y_2 - v)dudv\,, \quad (1.11)$$

Or simply the representation via a direct convolution formulation

$$g_2(x_2, y_2) = g_1(x_1, y_1) * h(u, v). \quad (1.12)$$

The corresponding system transfer function can be derived by taking a direct Fourier transform of Eq. 1.12,

$$G_2(f_x, f_y) = G_1(f_x, f_y)H(f_u, f_v). \quad (1.13)$$

The transfer function described by Eq. 1.13 is crucial for modelling a linear optical system and can be used to approximate its diffraction limit [21] [27]. As an example, if an optical system is fully illuminated by a coherent light source, represented by a complex wave function $\psi_{in}(x_1, y_2)$, where amplitude of the image system is assumed to be linear, the output of the system can be represented by the following expression,

$$\psi_{out}(x_2, y_2) = \psi_{in}(x_1, y_1) * h(u, v) \quad (1.14)$$

Where impulse response h is the amplitude-spread function (ASF) or coherent spread function for such coherent system.

However, in practice, most image systems operate with an incoherent illumination and the detector system measures only the intensity of light. Therefore, the complex wave function output in Eq. 1.14 is no longer accurate. Instead, the Point Spread function (PSF) is the correct representation in this case [27]. The PSF directly describes the formation of an image in relation to the distribution of light intensity and characterises how a point-like object is blurred through an image system [28] [21]. The output image from such system with linear intensity can be expressed as

$$I_{out} = I_{in} * |h|^2 \equiv I_{in} * PSF \quad (1.15)$$

Where, the PSF is equal to the amplitude squared of the ASF.

$$PSF = |h|^2 \quad (1.16)$$

The PSF of the whole complex image system can be decomposed into individual components described by the PSF. As an example, in a most basic optical microscope system consisting of an illumination source, optics and a detector, the output image is:

$$I_{out} = I_{in} * PSF_{source} * PSF_{optics} * PSF_{detector} \equiv I_{in} * PSF_{total} \quad (1.17)$$

1.2. Discrete Fourier transform

The introduction of a discrete version of the Fourier transform is fundamental for the implementation of computational wave propagators [23] [24]. For the clarity of the formulations presented in this thesis, the lateral coordinates in both real-space and reciprocal-space are reduced to one-dimension. Some common notations represent the relationship between continuous and discrete Fourier transform are listed in **Table 2** below.

Table 2: operational representation for continuous and discrete Fourier transform [23]

Terms	Continuous	Discrete
Real-space coordinate	x	$n\delta x$
Reciprocal-space coordinate	q	$p\delta q$
Fourier transform / inverse Fourier transform	$\mathcal{F}$ and $\mathcal{F}^{-1}$	F and f^{-1}
Integration	$\int dx$	$\sum \delta x$

The simplified formulations of the continuous Fourier transform are expressed below.

$$\mathcal{F}\{g(x)\} = G(q) = \frac{1}{\sqrt{2\pi}} \int g(x) \exp(-iqx)\, dx \tag{1.18}$$

$$\mathcal{F}^{-1}\{G(q)\} = g(x) = \frac{1}{\sqrt{2\pi}} \int G(q) \exp(iqx)\, dq. \tag{1.19}$$

The corresponding discrete forms are,

$$F\{g(n\delta x)\} = G(p\delta q) = \frac{1}{\sqrt{N}} \sum g(n\delta x) \exp\left(-\frac{i2\pi}{N} pn\right) \tag{1.20}$$

$$F^{-1}\{G(p\delta q)\} g(n\delta x) = \frac{1}{\sqrt{N}} \sum G(n\delta x) \exp\left(\frac{i2\pi}{N} pn\right). \tag{1.21}$$

The exponential term in Eq. 1.18 and Eq. 1.20 are set to be equivalent and N is total number of pixels in reciprocal-space.

$$\exp(-iqx) = \exp(-ip\delta qn\delta x) = \exp\left(-\frac{i2\pi}{N} pn\right). \tag{1.22}$$

Therefore, the relationship between the discrete sample in real-space and reciprocal-space can be derived as

$$\delta q \delta x = \frac{2\pi}{N} \tag{1.23}$$

The Fourier transform is the essential mathematical tool for computational imaging and digital signal processing. In the next section, the fundamental application to mathematical model for the wave propagation and along with its physical phenomena will be introduced.

1.3. Fundamentals of coherent X-ray imaging

1.3.1. Coherence

Coherence is a fundamental requirement of CDI imaging techniques, as it is the description of the correlation between two wavefields [28]. If an illumination wavefield exhibits sufficient coherence, the resulting interference pattern can be observed as diffraction fringe. The degree of coherence directly influences the visibility and contrast of the patterns resulting from the wave interference. In this section, two fundamental properties - temporal and spatial coherence are introduced.

1.3.1.1. Temporal coherence

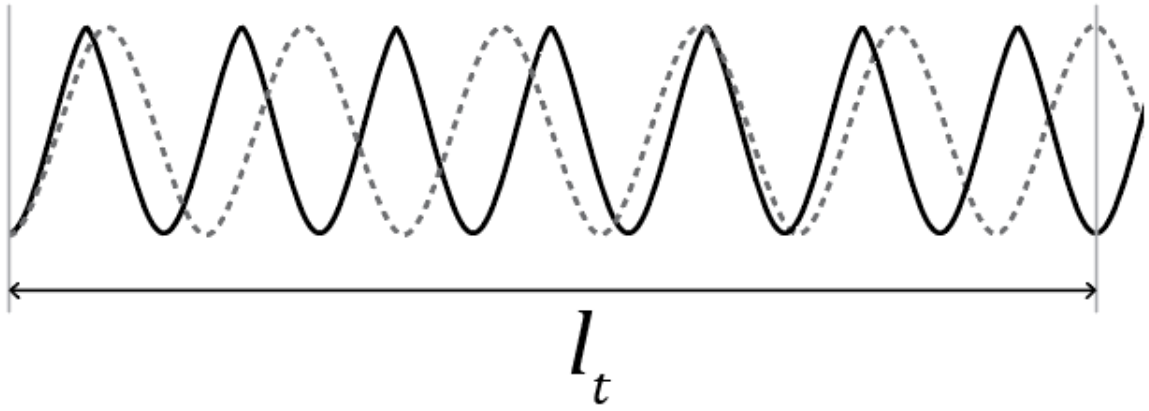

Figure 1.1: Illustration of temporal coherence length. l_t is the temporal coherence length, at which the two incident waves with different wavelength becomes anti-phase [29] .

Temporal coherence is used to quantify the correlation between two wavefields with different wavelengths in the same propagation direction. Consider two wavefields, one with a wavelength of λ with the other differing by $\Delta\lambda$. The temporal coherent length l_t measures the distance travelled before the two wavefronts become out of phase by $\frac{\lambda}{2}$:

$$l_t \approx 0.5\frac{\lambda^2}{\Delta\lambda}. \qquad (1.24)$$

Therefore, according to Eq. 1.24, the degree of temporal coherence can be directly linked to the power spectral density of the illumination source. For instance, in order to achieve a highly temporal coherent X-ray beam, monochromators are commonly installed to form a narrower source bandwidth [22] [30].

1.3.1.2. Spatial coherence

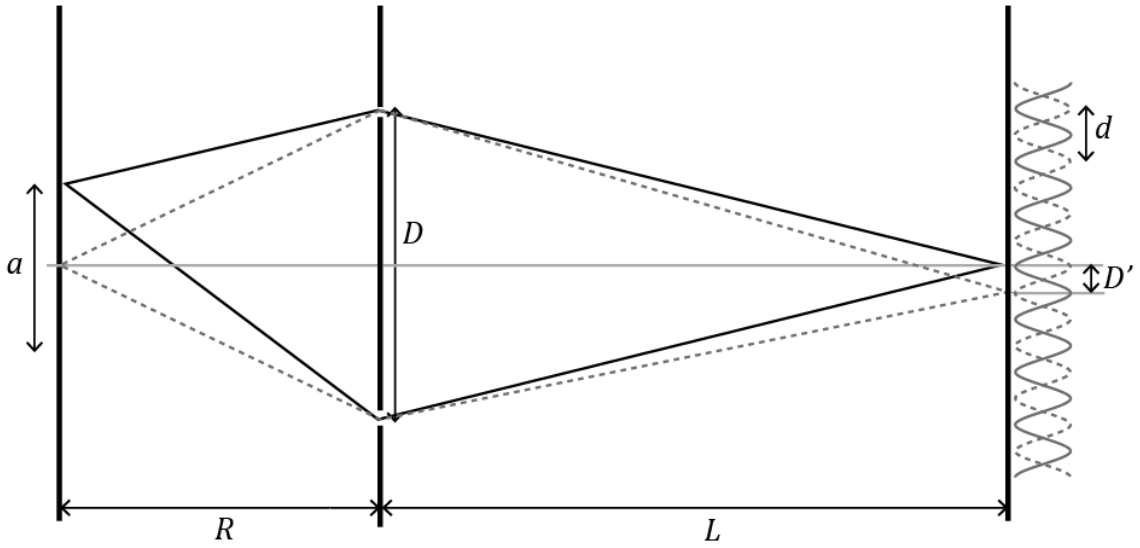

Figure 1.2: Illustration of spatial coherence length from Young's double-slit experiment. The lateral coherent length is the distance between the two small pinholes [29].

Two wavefields are considered spatially coherent, if their wavefronts exhibit a constant phase relationship. Similarly to the concept of temporal coherence, the degree of spatial coherence can be quantified using the spatial coherence length $l_{x,y}$. Spatial coherent length is determined by the maximum distance between two points where the inference of two wavefields can still be observed. As shown in Figure 1.2, d represents the distance from the maximum of the first interference fringe to the minimum of the second interference fringe:

$$d = \frac{1}{2}\frac{\lambda}{D}L = \frac{a}{2}\frac{L}{R}. \tag{1.25}$$

The transversal coherent length $l_{x,y}$ is:

$$l_{x,y} = D = \frac{\lambda R}{\mathrm{a}}. \tag{1.26}$$

Where λ is the wavelength of the illumination source, a indicates the size of source, D is the distance between two pinholes, R is the distance between the source and the pinhole plane, L is the distance between source and image plane.

As indicated by equation 1.26, the spatial coherence length is directly proportional to the source to image plane distance and inversely proportional to source size. Achieving high spatial coherence typically requires positioning the source at a considerable distance from the aperture, with a small source size. Therefore, the equation also suggests that high spatial coherence imaging techniques are more feasible with lower energy beams, which correspond to longer wavelength.

1.3.2. X-ray free-space propagation

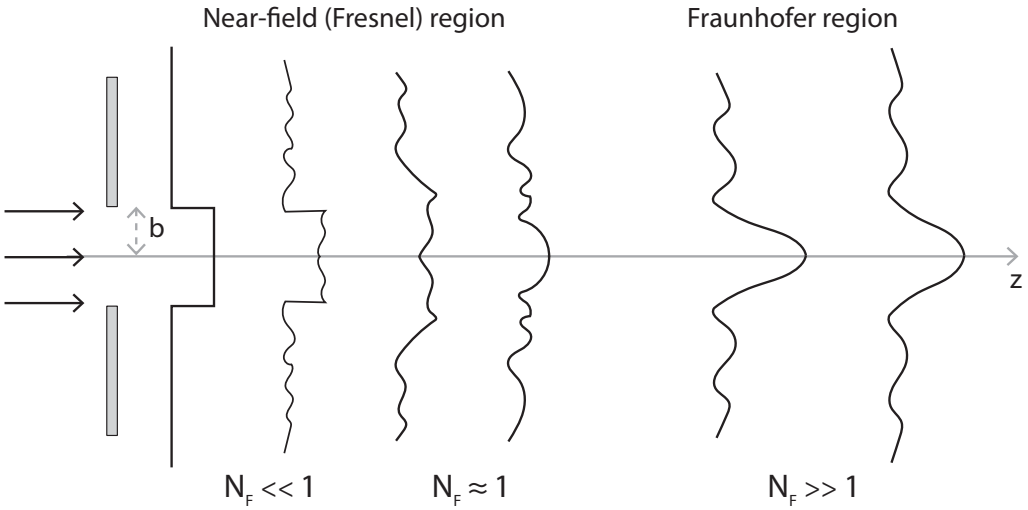

Figure 1.3: Physical diffraction effects observed from a small aperture.

Consider the case where an opaque screen with a small pinhole is illuminated by a point source of single-wavelength light. Figure 1.3 illustrates the fundamental physical principles of different types of diffraction as the propagation distance increases. If this wavefront is observed from a plane positioned very close to this screen, a defocused image of the pinhole

appears, which is termed near-field or Fresnel diffraction. As the observation plane moves further away, the diffraction fringes around the pinhole image become increasingly more prominent. However, as this distance continues to increase, the diffraction pattern becomes more defocused, indicating the transition to Fraunhofer/far-field condition [22]. One of the most direct methods to determine the diffraction condition is based on a parameter called the Fresnel number, shown in Eq. 1.26.

$$N_F = \frac{b^2}{\lambda z}, \tag{1.27}$$

where, b is the radius of the small aperture demonstrated in **Figure 1.3**.

A small Fresnel number ($N_F \ll 1$) indicates the far-field propagation of a wave field. Conversely, for $N_F \gg 1$ (typically larger than 100), near-field propagation occurs. When $N_F \approx 1$ (typically around 1-100), it is considered as the Fresnel diffraction region.

1.3.2.1. Free space propagation and angular spectrum

The complex scalar representation of a wave-field in free space, denoted as $\Psi(x,\ y,\ z,\ t)$, can be decomposed spectrally using the Fourier integral:

$$\Psi(x,\ y,\ z,\ t) = \frac{1}{\sqrt{2\pi}} \int_0^\infty \psi_\omega(x,\ y,\ z)\ \exp(-i\omega t)\ d\omega. \tag{1.28}$$

Each monochromatic component is represented as the evolution of spatial wave-function with respect to time t, where ω represents the angular frequency of the radiation source.

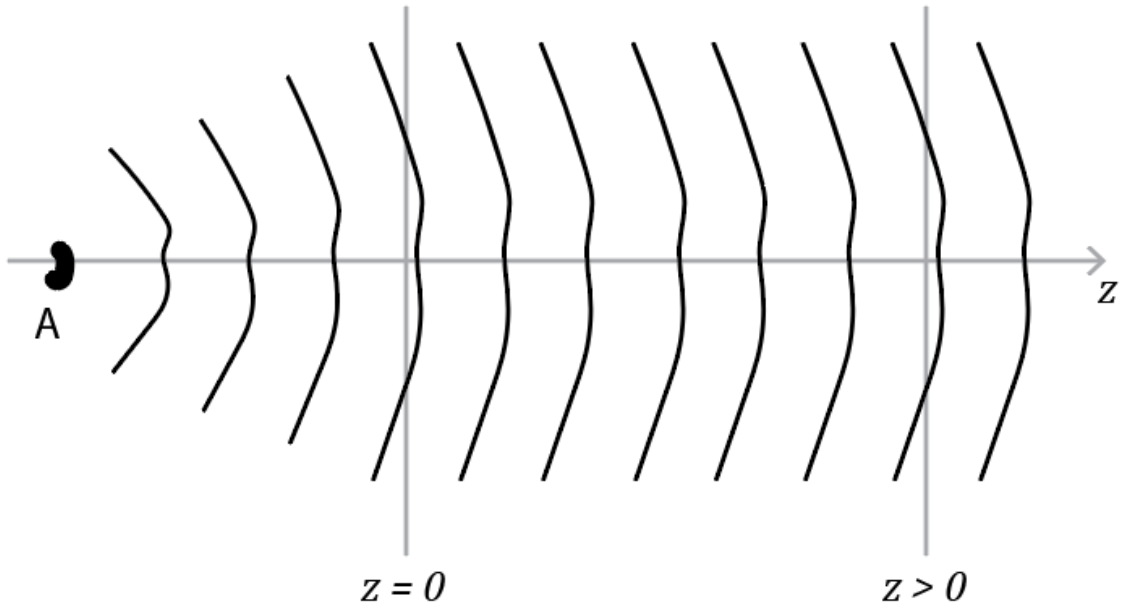

Figure 1.4: Free-space propagation of a plane wave originated from A in the optic axis direction of z. While a point source does not directly emit plane waves, at sufficiently large distances or when observing a small localised region, the emitted wave can be well approximated as a plane wave.

As demonstrated in **Figure 1.4**, in the z-direction, two parallel planes at distances $z = 0$ and $z = \Delta$ can be expressed as their forward-propagation fields $\psi_\omega(x,\, y,\, z\, =\, 0)$ and $\psi_\omega(x,\, y,\, z\, =\, \Delta)$. The corresponding wavefront of this plane wave can be expressed as:

$$\psi_\omega^{PW}(x,\, y,\, z) = \exp\left[i\left(q_x x + q_y y + q_z z\right)\right]. \tag{1.29}$$

The term (q_x, q_y, q_z) represent the x, z, y components of the wave-vector q of the plane-wave. k is the wave number, given by $k = \frac{2\pi}{\lambda}$, where λ is the wavelength of the radiation.

The z component from the q vector can then be rewritten in the following expressions,

$$q_x^2 + q_y^2 + q_z^2 = k^2, \tag{1.30}$$

$$q_z = \sqrt{k^2 - q_x^2 - q_y^2}. \tag{1.31}$$

As a result, the expression of plane wave from Eq. 1.29 can be rewritten:

$$\psi_\omega^{PW}(x,\, y,\, z) = \exp\left[i\left(q_x x + q_y y\right)\right] \exp\left[iz\sqrt{k^2 - q_x^2 - q_y^2}\right]. \tag{1.32}$$

At the distance $z = 0$, this unpropagated wavefield can be written as

$$\psi_{\omega}^{PW}(x,\, y,\, z = 0) = \exp\left[i\left(q_x x + q_y y\right)\right]. \tag{1.33}$$

To propagate the initial wavefield a distance of $z = \Delta > 0$, a "free-space" propagator is introduced, expressed as $\exp\left[i\Delta\sqrt{k^2 - q_x^2 - q_y^2}\right]$. This term accounts for the wave's phase evolution as it travels through free space.

The corresponding 2D Fourier integral of this unpropagated wave-field can be written in the following term,

$$\psi_{\omega}(x,\, y,\, z\, =\, 0) = \frac{1}{2\pi}\iint \mathcal{F}\psi_{\omega}\left(q_x,\, q_y,\, z\, =\, 0\right)\exp\left[i\left(q_x x + q_y y\right)\right]dq_x dq_y\,. \tag{1.34}$$

Similarly to its operator formulation, the Fourier representation of the propagated angular spectrum wave-field at distance z can also be expressed by the multiplication of free-space propagator and the reciprocal representation of the 2D plane-wave.

$$\begin{aligned}\psi_{\omega}(x,\, y,\, z\, =\, \Delta)\\ &= \frac{1}{2\pi}\iint \mathcal{F}\left\{\psi_{\omega}\left(q_x,\, q_y,\, z\, =\, 0\right)\right\}\exp\left[i\Delta\sqrt{k^2 - q_x^2 - q_y^2}\right]\\ &\quad\times\exp\left[i\left(q_x x + q_y y\right)\right]dq_x dq_y\,,\ \Delta \geq 0\\ &\approx \exp(ik\Delta)\,\mathcal{F}^{-1}\left\{\mathcal{F}\{\psi_{\omega}(x,\, y,\, z = 0)\}\exp\left(\frac{-i\Delta\left(q_x^2 + q_y^2\right)}{2k}\right)\right\}.\end{aligned} \tag{1.35}$$

However, it must be noted that if the condition under $k^2 < q_x^2 + q_y^2$ is met, the plane wave is then considered as 'evanescent wave'. In this scenario, the sub-wavelength information will be lost as the wave decays in z-direction.

To summarise, the angular spectrum propagator of a wavefield ψ_{ω} can be expressed in a simplified formulation as,

$$D_{AS} = \mathcal{F}^{-1}\left\{\mathcal{F}\{\psi_{\omega}\}\exp\left(\frac{-i\Delta\left(q_x^2 + q_y^2\right)}{2k}\right)\right\}. \tag{1.36}$$

This expression for Angular spectrum propagator will be used consistently throughout this thesis. Furthermore. the free-space propagation over a distance $z\, =\, \Delta$ can be express as,

$$\psi_{\omega}(x,\, y,\, z\, =\, \Delta)\, =\, \mathcal{D}_{AS\Delta}\{\psi_{\omega}(x,\, y,\, z\, =\, 0)\},\ \Delta \geq 0. \tag{1.37}$$

1.3.2.2. Fresnel diffraction

Fresnel diffraction is a specific case occurring at the transition point between the near-field and far-field region. Fresnel propagator can be directly derived using approximation theory from angular spectrum formulation under the assumption of "paraxial" condition. The term paraxial implies that all the plane-wave components along the optic axis are considered to have small angles.

Under the condition, where both q_x and q_y are << q_z , and $q_z \geq 0$. Eq. 1.30 can be approximated via binomial approximation:

$$\sqrt{k^2 - q_x^2 - q_y^2} \approx k - \frac{q_x^2 + q_y^2}{2k}, \tag{1.38}$$

Consequently, the Fresnel diffraction operation $D_\Delta^{Fresnel}$ can be derived from the angular spectrum/near-field propagator,

$$D_{AS\Delta} \approx D_\Delta^{Fresnel} = \exp(ik\Delta)\,\mathcal{F}^{-1} \exp\left[\frac{-i\Delta(q_x^2 + q_y^2)}{2k}\right]\mathcal{F} \tag{1.39}$$

$$\psi_\omega(x,\, y,\, z\, =\, \Delta)\, \approx D_\Delta^{Fresnel}\, \psi_\omega(x, y, z\, =\, 0)$$

$$= \exp(ik\Delta)\,\mathcal{F}^{-1} \exp\left[\frac{-i\Delta(q_x^2 + q_y^2)}{2k}\right]\mathcal{F}\psi_\omega(x,\, y,\, z\, =\, 0),\ \Delta \geq 0 \tag{1.40}$$

where $\mathcal{F}$ denotes a forward Fourier transform.

Additionally, the convolution integral form of Fresnel diffraction can be expressed as:

$$\psi_\omega(x,\, y,\, z\, =\, \Delta \geq 0)$$

$$= -\frac{ik\exp(ik\Delta)}{2\pi} \iint_{-\infty}^{\infty} \psi_\omega(x',\, y', z = 0) \times \exp\left\{\frac{ik}{2\Delta}[(x - x')^2 + (y - y')^2]\right\} dx'dy'$$

$$= -\frac{ik\exp(ik\Delta)}{2\pi} \exp\left[\frac{ik}{2\Delta}(x^2 + y^2)\right] \times$$

$$\iint_{-\infty}^{\infty} \psi_\omega(x',\, y', z = 0) \exp\left[\tfrac{ik}{2\Delta}(x'^2 + y'^2)\right] \times \exp\left[\tfrac{-ik}{\Delta}(xx' + yy')\right] dx'dy' \tag{1.41}$$

Where $\psi_\omega(x',\, y', z = 0)$ denotes the unpropagated original wavefield.

1.3.2.3. Fraunhofer diffraction

Mathematically, Fraunhofer or far-field diffraction can be considered as the limiting case of the Fresnel diffraction integral in Eq. 1.41. If the propagation distance is far enough, then this wavefront is now propagated to the "far-field" regime. The resulting diffraction pattern is known as a Fraunhofer (far-field) diffraction pattern. The corresponding Fraunhofer diffraction integral can be expressed in the form below,

$$\psi_\omega(x,\, y,\, z\, =\, \Delta) = -\frac{ik\exp(ik\Delta)}{2\pi}\exp\left[\frac{ik}{2\Delta}(x^2+y^2)\right] \times \iint_{-\infty}^{\infty}\psi_\omega(x',\, y', z=0)\exp\left[\frac{-ik}{\Delta}(xx'+yy')\right]dx'dy'. \quad (1.42)$$

The simplified formation can be approximated into the following expression,

$$\psi_\omega(x,\, y,\, z\, =\, \Delta) = -\frac{ik\exp(ik\Delta)}{2\pi\Delta}\exp\left[\frac{ik}{2\Delta}(x^2+y^2)\right]\mathcal{F}[\psi_\omega(x',\, y',\, z\, =\, 0)]. \quad (1.43)$$

Where $\psi_\omega(x',\, y',\, z\, =\, 0)$ denotes the initial wavefront. This implies that the far-field propagation essentially produces a wavefront directly proportional to the Fourier transform of the original wavefront.

1.3.2.4. Fresnel scaling theorem

The Fresnel scaling theorem facilitates the conversion of a cone-beam projection into an equivalent parallel-beam geometry with an effective coordinate system [22], as shown in **Figure 1.5**.

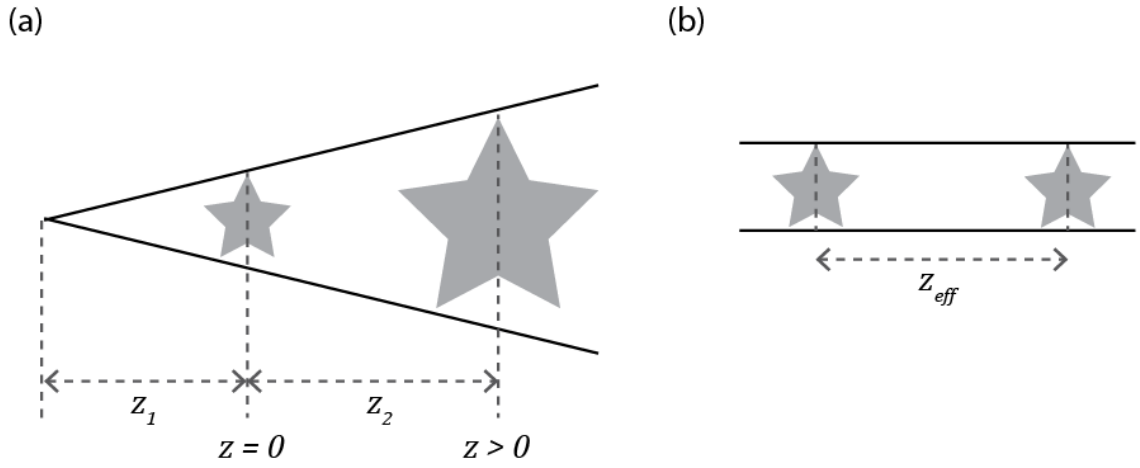

Figure 1.5: Demonstration of Fresnel scaling theorem (not to scale). (a) cone-beam geometry and (b) the equivalent parallel-beam geometry.

Under the condition of both paraxial and projection approximation, the exit wave from the sample point at distance $z = 0$ for the parallel illumination ψ_ω^{plane} is equivalent to the point illumination ψ_ω^{cone} following the expression below

$$\psi_\omega^{cone}(x, y, z = 0) = \psi_\omega^{PW}(x, y, z = 0)\exp\left[\frac{ik}{2z_1}(x^2 + y^2)\right]. \qquad (1.44)$$

By substituting Eq. 1.44 in Eq. 1.41,

$$\psi_\omega^{cone}(x,\ y,\ z = \Delta \geq 0) = -\frac{ik\exp(ikz_2)}{2\pi z_2}\exp\left[\frac{ik}{2z_2}(x^2 + y^2)\right] \times \iint_{-\infty}^{\infty} \psi_\omega^{PW}(x',\ y', z = 0)$$

$$\times \exp\left[\frac{ik}{2\left(\frac{1}{z_1} + \frac{1}{z_2}\right)^{-1}}(x'^2 + y'^2)\right] \times \exp\left[\frac{-ik}{\left(\frac{1}{z_1} + \frac{1}{z_2}\right)^{-1}}(xx' + yy')\right] dx'dy'. \qquad (1.45)$$

The geometric magnification M in **Figure 1.5(a)** is given by:

$$M = \frac{z_1 + z_2}{z_1}. \tag{1.46}$$

The effective propagation distance can therefore be derived as,

$$z_{eff} = \left(\frac{1}{z_1} + \frac{1}{z_2}\right)^{-1} = \frac{z_2}{M}. \tag{1.47}$$

Subsequently, the final representation of Fresnel Scaling Theorem can be derived as:

$$\psi_\omega^{cone}(x,\, y,\, z\, =\, \Delta \geq 0)\, = -\frac{ik\exp(ikz_2)}{2\pi z_2}\exp\left[\frac{ik}{2z_2}(x^2 + y^2)\right] \times \iint_{-\infty}^{\infty} \psi_\omega^{PW}(x',\, y', z = 0)$$

$$\times \exp\left[\frac{ikM}{2z_2}(x'^2 + y'^2)\right] \times \exp\left[\frac{-ik}{z_2}(xx' + yy')\right] dx'dy'. \tag{1.48}$$

In addition, the relationship of corresponding intensity representation between the cone beam and parallel beam can be formulated as

$$I_\omega^{cone}(x,\, y,\, z\, =\, \Delta \geq 0) = M^{-2} I_\omega^{PW}\left(\frac{x}{M},\, \frac{y}{M},\, z\, =\, \frac{\Delta}{M} \geq 0\right). \tag{1.49}$$

1.4. Discrete near-field propagation and sampling condition

So far, wave propagation has been described using continuous Fourier transforms. To model wave propagation computationally, it requires discrete equivalents. The digital implementation of the Fresnel propagation model based on single Fourier transform, Fresnel transfer function and impulse response will be described in this Section [23] [24] [25].

1.4.1. Single Fourier transform

In Section 1.3.2.2, the formulation of a continuous expression for Fresnel-Kirchhoff integral was introduced. For convenience, Eq. 1.41 is simplified into the one-dimensional representation,

$$\psi(x, \Delta) = \frac{1}{\sqrt{i\lambda\Delta}}\exp\left[\frac{ik}{2\Delta}x^2\right]\int \psi(x', 0)\exp\left[\frac{ik}{2\Delta}x'^2\right]\exp\left[\frac{-ik}{2\Delta}xx'\right]dx'. \tag{1.50}$$

The corresponding discrete form of Eq. 1.50 can be rewritten

$$\psi(m\delta x, \Delta) = \frac{1}{\sqrt{i\lambda\Delta}} \exp\left[\frac{ik}{2\Delta} m^2 \delta x^2\right] \sum_{n=0}^{N-1} \psi(n\delta x', \Delta) \exp\left[\frac{ik}{2\Delta} n^2 \delta x'^2\right] \exp\left[\frac{-ik}{2\Delta} m\delta x\, n\delta x'\right] dx'. \quad (1.51)$$

Where, x' corresponds to the real space coordinate, and x is the coordinate at output plane. Their equivalent discrete expressions are $n\delta x'$ and $m\delta x$ respectively.

The exponential functions in both continuous and discrete Fourier transform are equivalent, as shown in Eq. 1.52,

$$\exp\left[\frac{-ik}{2\Delta} m\delta x n\delta x'\right] = \exp\left[\frac{-i\pi}{N} mn\right]. \quad (1.52)$$

The equivalence condition is necessary to ensure that discrete Fourier propagation correctly approximates the continuous physics of wave propagation and maintains phase consistency between the two formulations.

This gives the relationship between the pixel sizes in real space δx and the corresponding destination plane $\delta x'$

$$\delta x \delta x' = \frac{\lambda\Delta}{N}. \quad (1.53)$$

Where, the observation plane is considered as a square grid consisting of $N \times N$ pixels.

The discrete Fresnel Kirchhoff integral can be represented using a direct Fourier transform:

$$\psi(m\delta x, \Delta) = \frac{1}{\sqrt{i\lambda\Delta}} \exp\left[\frac{i\pi\lambda\Delta m^2}{N^2 \delta x'^2}\right] F\left\{\psi(n\delta x', \Delta) \exp\left(-\frac{ik}{2\Delta}\, n^2\, \delta x'^2\right) \delta x'\right\} \quad (1.54)$$

1.4.2. Fresnel transfer function and impulse response

The one-dimensional angular spectrum propagator can be rewritten from Eq. 1.36 to the expression below

$$\psi(x, \Delta) = \mathcal{F}^{-1}\left\{\mathcal{F}\{\psi(x, 0)\} \exp\left(-\frac{i\Delta}{2k}\, q^2\right)\right\}. \quad (1.55)$$

The corresponding discrete form of Eq. 1.55 is,

$$\psi(m\delta x, \Delta) = F^{-1}\left\{F\{\psi(n\delta x, 0)\} \exp\left[-\frac{i\Delta}{2k}\, p^2 q^2\right]\right\}. \tag{1.56}$$

The discrete transfer function that represents the propagation of each frequency component is given:

$$\breve{H}_{\Delta}(p\delta q) = \frac{1}{\sqrt{2\pi}} \exp\left[-\frac{i\Delta}{2k}\, p^2 q^2\right]. \tag{1.57}$$

Accordingly, Eq. 1.54 can be written in the form using impulse response and convolution theorem,

$$\psi(x, \Delta) = \sqrt{2\pi}\mathcal{F}^{-1}\left\{\mathcal{F}\{\psi(x, 0)\}\mathcal{F}\left[\frac{1}{\sqrt{i\lambda\Delta}} \exp\left(-\frac{ikx^2}{2\Delta}\right)\right]\right\}. \tag{1.58}$$

Which gives the discrete form of

$$\psi(m\delta x, \Delta) = F^{-1}\left\{F\{\psi(n\delta x, 0)\}\, F\left\{\frac{1}{\sqrt{i\lambda\Delta}} \exp\left(-\frac{ikm^2\delta x^2}{2\Delta}\right)\right\}\delta x\right\}. \tag{1.59}$$

The discrete impulse response is

$$\breve{h}_{\Delta}(m\delta x) = \frac{1}{\sqrt{i\lambda\Delta}} \exp\left[\frac{ikm^2\delta x^2}{2\Delta}\right]. \tag{1.60}$$

Eq. 1.52 implies the maximum spatial frequency of the propagator at observation plane,

$$k_{max} = \frac{\lambda\Delta}{2N^2\delta x'^2}. \tag{1.61}$$

1.4.3. Sampling condition for Near-field propagator

Consider the one-dimensional Nyquist-Shannon sampling theorem as shown in **Figure 1.6** [31].

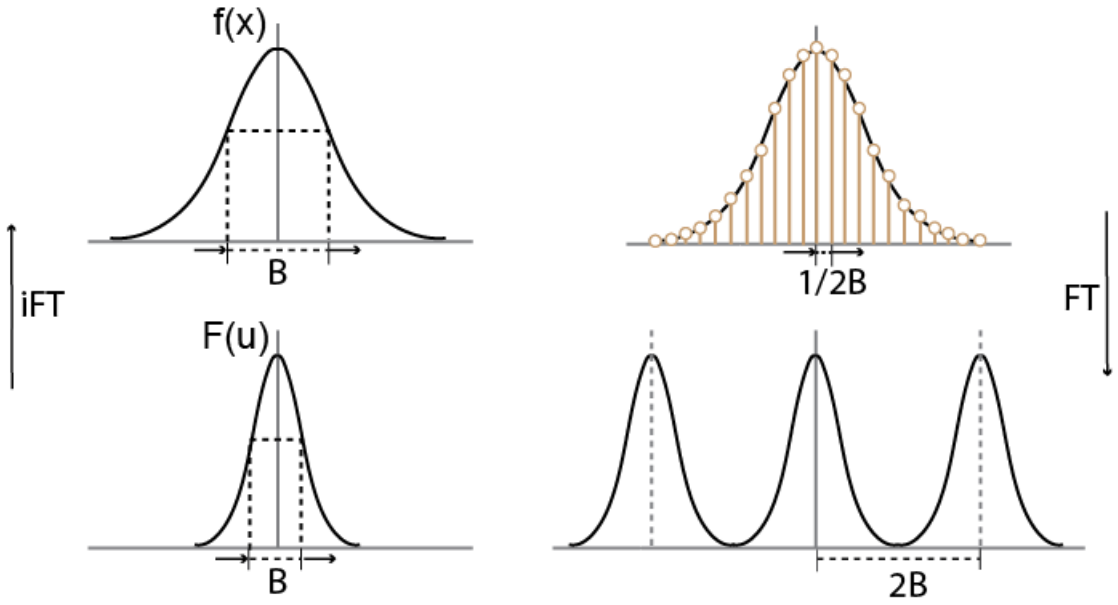

Figure 1.6. Shannon sampling theorem for a 1D signal in real space $f(x)$ and the corresponding Fourier domain $F(u)$. For a continuous signal with bandwidth of B, the minimal sampling rate is $1/2B$ in real space and 2B in Fourier space. FT: Fourier transform. iFT: inverse Fourier transform [31].

In order to avoid aliasing arising in sampling a real space signal $f(x)$, the minimal sampling rate is required to be $1/2B$. In reciprocal space, the separation between two signal spectrums needs to be larger than the width of each spectrum $2B$ to avoid aliasing. i.e. The minimal sampling pixel spacing is inversely proportional to doubled cut-off frequency, which is equivalent to twice the signal's bandwidth in reciprocal space [31].

The sampling condition according to Shannon's theorem is

$$N > \frac{1}{2k_{max}}. \tag{1.62}$$

Substitute Eq. 1.61 in Eq. 1.62, the near-field propagation sampling requirement is derived,

$$N < \frac{\lambda\Delta}{\delta x'^2} = \frac{\lambda\Delta}{\delta x^2}. \quad (1.63)$$

The derivation stated in Eq.1.63 is based on the assumption that the magnification between sample plane and observation plane remains unity. In the actual implementation for the near-field propagation, the geometrical scaling also needs to be carefully considered for the sampling condition.

1.5. Projection approximation - contrast formation in X-ray image

The projection approximation is used to model the interaction between a radiation and matter, where the scattering effect is neglected within the object. The derivation of the project approximation in regard to the phase and amplitude shifts is introduced in this section [22].

The complex refractive index n_ω models the interaction between a radiation source and matter,

$$n_\omega(r,z) = 1 - \delta(r,z) + i\beta(r,z), \quad (1.64)$$

where r represents the lateral coordinate (x,y).

Assuming that the source energy is higher than the electron binding energy, δ is a function related the electron density of the object,

$$\delta(r,z) = \frac{r_e\lambda^2}{2\pi} n_e(r), \quad (1.65)$$

Where λ is the wavelength of the radiation and r_e is the Bohr radius, n_e is the sum of electron densities of all atoms.

$$n_e = Zn_a(r), \quad (1.66)$$

n_a is the number density of the atoms, and Z is the number of electrons.

The term β in Eq. 1.64 is directly related to the linear attenuation due to photoelectric effect,

$$\beta(r,z) = \frac{\lambda}{4\pi}\mu(r,z), \quad (1.67)$$

where μ is the photoelectric attenuation coefficient.

The interaction between a radiation beam with matter can also be expressed in the form of the inhomogeneous Helmholtz wave equation propagation in z direction,

$$(\nabla^2 + n_\omega^2(r,z)k^2)\psi_\omega(r,z) = 0, \tag{1.68}$$

where

$$\nabla^2 = \nabla_\perp^2 + \partial_z^2, \tag{1.69}$$

Where the transverse Laplacian $\nabla_\perp^2$ is equivalent to $\partial_x^2 + \partial_y^2$

Under paraxial approximation the scattered wave field can be expressed as a plane wave propagate in z direction with the disturbance from an envelope function ψ'_ω.

$$\psi_\omega(r,z) = \psi'_\omega(r,z)\exp(ikz). \tag{1.70}$$

Now the inhomogeneous paraxial wave equation can be derived, with the neglecting of ∂_z^2,

$$(2ik\partial_z + \nabla_\perp^2 + (n_\omega^2(r,z) - 1)k^2)\,\psi'_\omega(r,z) = 0. \tag{1.71}$$

The wave equation here assumes that the original wavefield continues to propagate in z-direction, and as the scattering is sufficiently weak which implies that there is no further interaction for any other neighbouring ray trajectories. Consequently, the Laplacian term of the wave equation can be neglected.

$$\partial_z\,\psi'_\omega(r,z) \approx \frac{ik}{2}\big(1 - n_\omega^2(r,z)\big)\psi'_\omega(r,z). \tag{1.72}$$

The wavefield exiting a surface at z_0 can be approximated as:

$$\psi'_\omega(r, z = z_0) \approx \exp\left(\frac{k}{2i}\int_0^{z=z_0}[1 - n_\omega^2(r,z)]dz\right)\psi'_\omega(r, z = 0)\,. \tag{1.73}$$

As the refractive index of a radiation source represented in Eq. 1.64, both δ and β are significantly smaller than unity, therefore,

$$1 - n_\omega^2(r,z) \approx 2\big[\big(\delta(r,z) - i\beta(r,z)\big)\big]. \tag{1.74}$$

Which leads to the further approximation of the above equation to the expression below:

$$\psi'_\omega(r, z = z_0) \approx \exp\left(-ik\int_0^{z=z_0}[\delta(r,z) - i\beta(r,z)]dz\right)\psi'_\omega(r, z = 0). \tag{1.75}$$

The exponential term of the function in Eq. 1.75 is also known as the object's complex transmission function

$$o(r) = \exp\left(-ik\int_0^{z=z_0}[\delta(r,z) - i\beta(r,z)]dz\right). \quad (1.76)$$

Where the phase shift $\Delta\phi$ can be derived from the first term of the exponential function,

$$\Delta\phi = k\int[\delta(r,z) - i\beta(r,z)]dz\,. \quad (1.77)$$

However, for the scattering through a homogenous material, the phase shift is directly dependent on the thickness of the material Δz.

$$\Delta\phi = -k\delta(r,z)\Delta z. \quad (1.78)$$

The second term of the exponential function in Eq. 1.75, $\exp\left(-ik\int_0^{z=z_0}[i\beta(r,z)]dz\right)$ indicates the absorption of the radiation along the z-direction.

Finally, the exit wave $\psi'_\omega(r, z = z_0)$ can be approximated as the wavefield before entering the object, modulated by the object's transmission function, which leads to the expression of projection approximation:

$$\psi'_\omega(r, z = z_0) = o(r)\,\psi'_\omega(r, z = 0). \quad (1.79)$$

1.6. Resolution

Resolution refers to the measurement that quantifies how small an object can be visualised through a microscope, which also effectively defines the limitation of an optical system. In this section, the diffraction limit to the resolution defined by the Rayleigh criterion will be introduced.

1.6.1. Rayleigh resolution

Two main factors that limit the resolution in a CDI system arise from the finite size of a lens or the diffraction limit determined by ray optics [26].

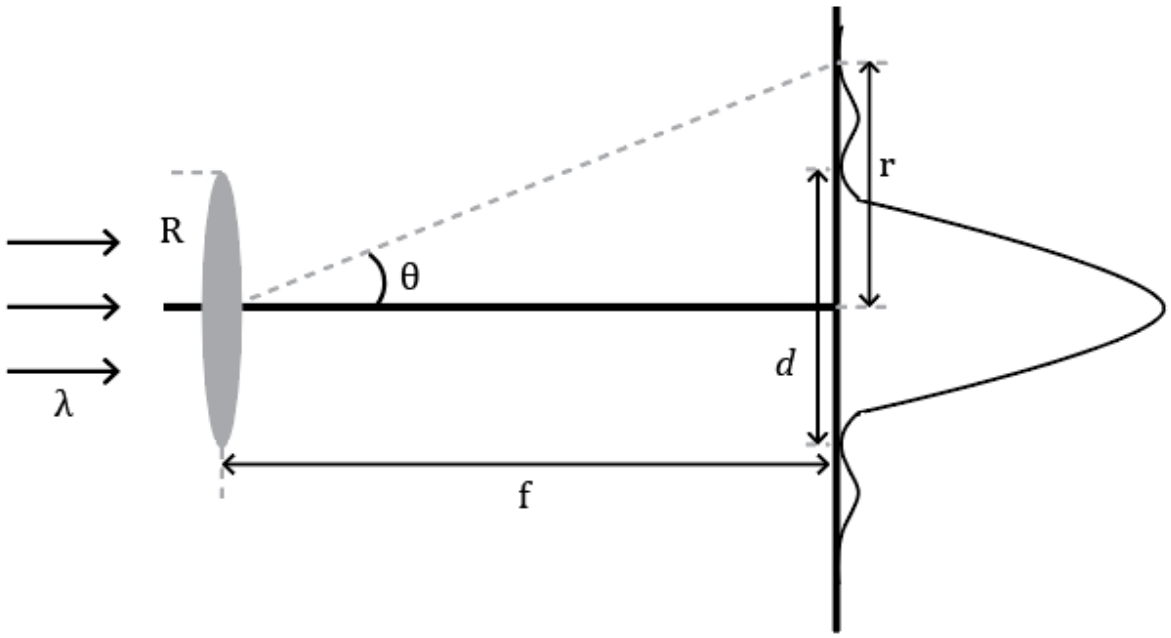

Figure 1.7: illustration of diffraction limit due to the finite aperture

Consider the case of far-field diffraction, an airy disc like diffraction pattern is formed by a circular finite aperture with focal length f and radius R, as shown in **Figure 1.7**. The width d of the central spot of the diffraction pattern is

$$d = 1.22\frac{\lambda f}{R}. \qquad (1.80)$$

The Rayleigh criterion defines the minimum resolvable distance between two point sources, which is called Rayleigh resolution $\Delta\delta$ [21] which is determined by the distance between the peak of the diffraction pattern from the first point source coincides with the first minima of the diffraction pattern formed by the secondary point source. Therefore, the Rayleigh resolution $\Delta\delta$ or this minimal resolvable distance is given by,

$$\Delta\delta = \frac{1}{2}d = 0.61\frac{\lambda f}{R}. \tag{1.81}$$

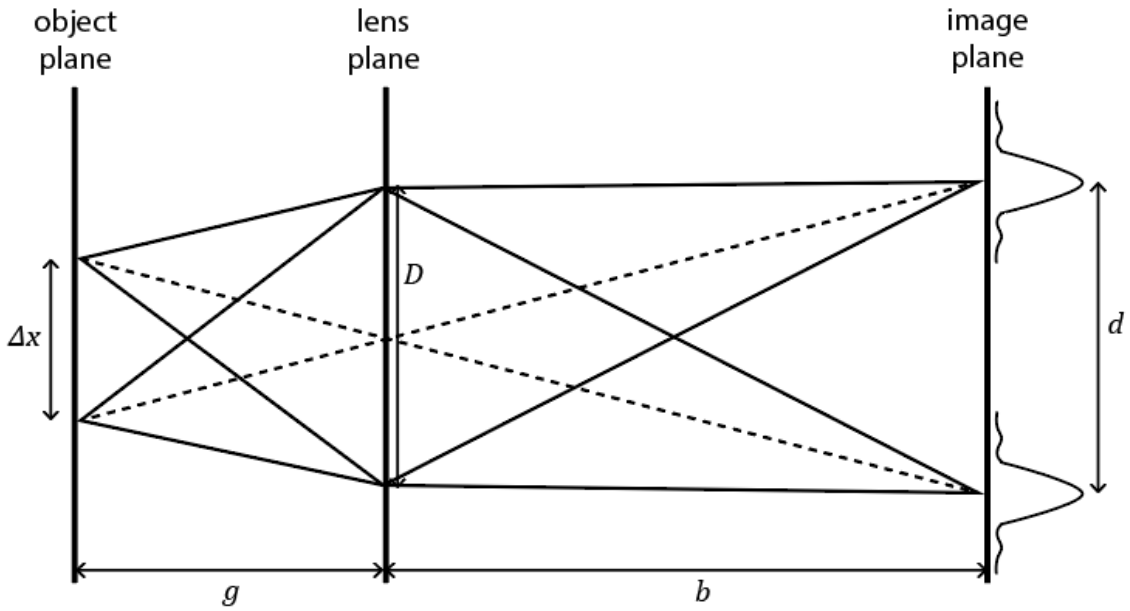

Figure 1.8: Illustration of the diffraction limit of a microscope system.

For an ideal and aberration free microscopy system, the output image formed by the imaging system can be summarised as the convolution of far-field diffraction of the lens and (de-)magnified image [21]. However, in the reality, the resolution of an image system is often constrained by diffraction limit and consequently results in a blurring effect.

As shown in **Figure 1.8**. The minimal solvable distance d between the two points indicated in the image plane set by diffraction is,

$$d = 1.22\frac{\lambda b}{D}. \tag{1.82}$$

Subsequentially, the corresponding minimal resolvable distance between two points in the object plane is, assuming the sample is placed at the focal plane of the lens,

$$\Delta x_{min} = 1.22\frac{\lambda g}{D} = 1.22\frac{\lambda f}{D}. \quad (1.83)$$

This can be rewritten in the form in terms of the numerical aperture of the imaging system, which is maximum half angle θ that light can be collected by a lens,

$$NA = nsin(\theta). \quad (1.84)$$

The term $\frac{f}{D}$ in Eq. 1.83 can be substituted by half of inversed NA value, which determines the highest resolution can be achieved by a microscopy system.

$$\Delta\delta = \Delta x = 0.61\frac{\lambda}{NA}. \quad (1.85)$$

2. Ptychography

This chapter commences with an historical review of coherent diffractive imaging methods, highlighting the phase problem with those conventional techniques. It delves into the development of iterative phase retrieval algorithms and ptychography, one of the key solutions to this “phase problem” and explains the various configuration of ptychography. Finally, the development and implementation of near-field ptychography and multi-slice ptychography are reviewed and explored in depth. These two techniques together build up the groundwork for the rest of the thesis.

2.1. Development of Coherent Diffractive Imaging

The pursuit of atomic resolution in microscopy has been hindered by the inherent limitations of conventional electron microscopes due to spherical aberration of the lens, which distorts electron wavefronts and reduces image resolution, although aberration correction techniques have significantly mitigated these limitation. In 1947, D. Gabor introduced a ground-breaking concept – holography (the term holography has become an increasingly common term, and it was called hologram and holoscope in his original proposal) [5] [6]. Instead of relying on imperfect lenses, D. Gabor proposed to record the entire field information of a sample using coherent illumination. To achieve this, a two-step method was introduced. Firstly, a coherent illumination was required to interfere with a sample, called the object wave. Then this object wave interferes with a coherent background field, known as the reference beam. The resulting interference pattern, captured by a photographic plate, is called a hologram, and encodes both important phase and amplitude information. The progress of holography faced significant challenges due to technological limitations during its early stages, leading D. Gabor to eventually set it aside. However, with the development of stable and coherent light sources in the 1960s [32], such as lasers, this once "forgotten" technique experienced a resurgence and regained its prominence within the scientific community.

Traditionally, X-ray diffraction techniques were developed to determine the three-dimensional atomic structures of crystalline materials, known as crystallography [33]. The groundwork for Coherent Diffractive Imaging (CDI) can be traced back to the work by W. Bragg in the late 1930s, where the crystal structure can be observed from the X-ray diffraction generated by the crystal lattices [33].

However, with the expansion of scientific exploration and interests into diverse fields such as physics, materials science, and biology, the need to image non-crystalline structures has grown. Along with the development of highly coherent X-ray sources, efficient detectors and computational power, D. Sayre finally proposed the concept of CDI in 1980 as an alternative to X-ray crystallography for non-crystalline samples [7] [34], and his idea was later validated by J. Miao in 1999 with the successful imaging of a non-crystalline sample for the first time [8] [35].

The modern CDI method (as shown in **Figure 2.1**) offers a robust approach for studying the structure of both crystalline and non-crystalline samples [8]. Essentially, CDI involves illuminating a sample with a highly coherent and high flux X-ray beam. The beam is scattered by a sample and the X-ray then propagates to and is recorded by a detector in the far-field, resulting in a diffraction pattern directly proportional to the Fourier transform of the object.

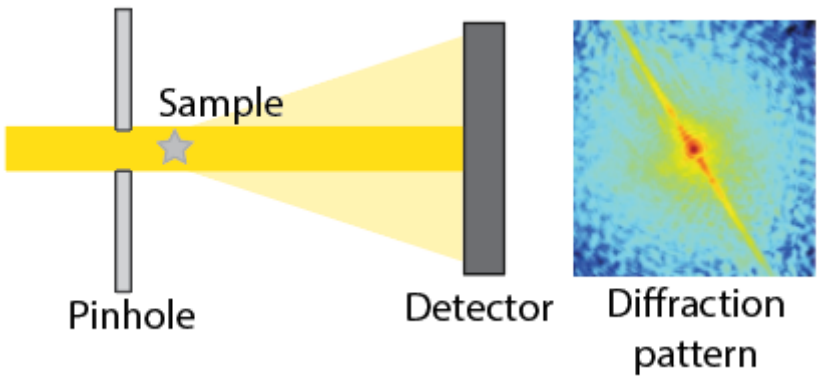

Figure 2.1. Conventional CDI configuration with a typical far-field coherent diffraction pattern shown on the right. The image on the right is reproduced from [36] permission from ©Elsevier

This process, however, presents a challenge known as the "phase problem", where crucial phase information is lost during the process of recording diffraction patterns. Fortunately,

the later development in iterative algorithms (**Figure 2.3**) can be employed to recover this lost phase information, enabling the reconstruction of a high-resolution image from the diffraction pattern.

2.2. The phase problem

Waves are characterised by two fundamental properties - amplitude and phase. These properties can be mathematically represented by a complex scalar function consisting of a real valued amplitude and the complex exponential of phase.

$$\psi(x,y) = |\psi(x,y)| \exp\big(i\varphi(x,y)\big) \tag{2.1}$$

The propagation of a wavefield can only be accurately predicted if both modulus and the phase of this function are known. However, a major challenge has arisen: detectors are only able to record the intensity of a wavefield, which corresponds to the square of the wave modulus,

$$I(x,y) = |\psi(x,y)|^2 = \psi(x,y)\psi^*(x,y) \tag{2.2}$$

The important phase information $\varphi(x,y)$ is discarded in this process. And this inability in directly measuring phase information is known as the "**phase problem**".

Two common methods to overcome the phase problem are interferometry based techniques and phase retrieval algorithms. Interferometric methods require prior knowledge of a reference beam. Then the phase information of a sample can be retrieved from the interference pattern with the reference beam [6] [37]. Phase retrieval algorithms usually leverage the recorded intensity with additional constraints, so that the missing phase information can be estimated iteratively with these algorithms.

Ptychography is a technique developed upon the principle of phase retrieval method. It provides a unique and powerful solution to the phase problem by exploiting the redundant information present in overlapping diffraction patterns [11] [38]. A detailed discussion on ptychography and phase retrieval algorithms will be presented later in this chapter.

2.3. History of ptychography

Ptychography is a word coming from Greek - ptycho, means “convolution” and “to fold”. This original concept was initially proposed by Walter Hoppe back in 1969 to retrieve the phase information for solving crystal structures through Bragg peaks [39] [40] [41] [42]. The interference of a confined coherent electron probe illumination on a crystalline specimen can be modelled as a convolution between the Bragg peaks (reciprocal-space sharp intensity maxima structure of the crystal) and the Fourier transform of the probe. As demonstrated in **Figure 2.2**., the schematic of the first “crystallographic ptychography” configuration, if the size of the illumination is small enough to match with the crystal lattice spacing, the corresponding width in its reciprocal space will be comparable to the distance between Bragg peaks [43] [44]. Consequently, the convolution of the crystal structure and the beam in reciprocal space will overlap and interfere with each other. The phase information encoded in the diffraction fringes (**Figure 2.2(b)**) can then be then retrieved from those overlaps.

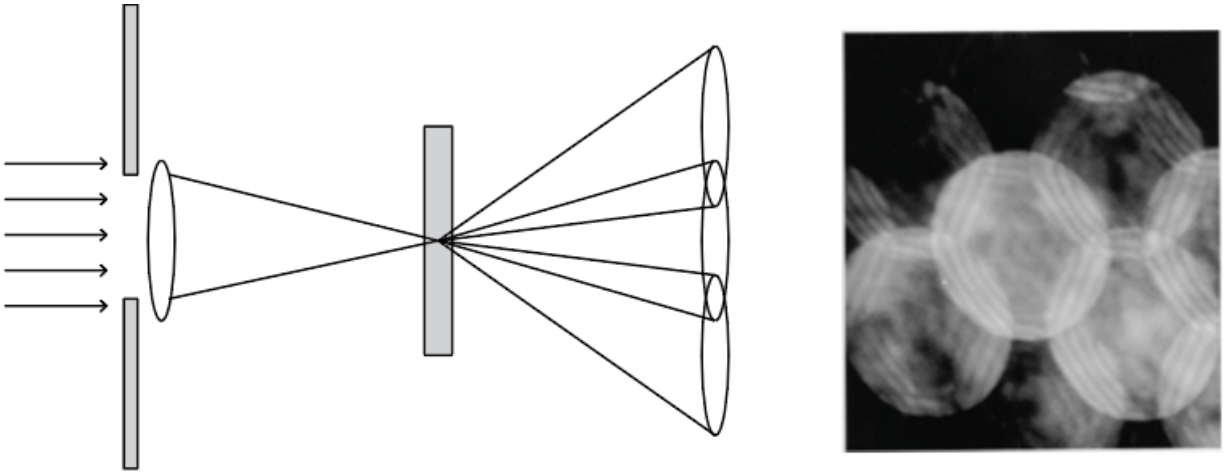

Figure 2.2. Experimental configuration for the original ptychography for observing crystal structure. The illumination probe interferences with a crystalline sample and the diffraction orders are convoluted in the reciprocal plane with aperture function. An example diffraction pattern from a thin silicon structure is shown on the right and is reproduced from [44] permission from ©Elsevier.

2.4. Development of iterative algorithm and modern ptychography

At its inception, ptychography posed significant challenges due to computational inefficiency and the limitations of available computer memory and processing power. A breakthrough came in 1972 with the introduction of the first iterative phase retrieval framework called the Gerchberg-Saxton (GS) algorithm (**Figure 2.3**) developed by R. Gerchberg and O. Saxton [45]. It begins with an initial guess of a wavefield, and the algorithm iteratively propagates this wave field back and forward via Fourier transform between the "object guess" and "intensity measurement, $\mathrm{I}(r) = |\Psi(u)|^2$ ", where the intensity measured from the Fourier space is then used to replace the intensity of the real space object estimation. Subsequentially, the modulus projector $\mathcal{P}_M$ of the current iteration can be updated by replacing the current estimation with the intensity measurement, given by:

$$\mathcal{P}_M\{\psi(r)\} = \sqrt{\mathrm{I}(r)}\frac{\Psi(u)}{|\Psi(u)|}, \tag{2.3}$$

where $\Psi(u)$ is the direct Fourier transform of $\psi(r)$. The iterative process continues until a specific constraint is met and the algorithm is then deemed to have converged to a "solution".

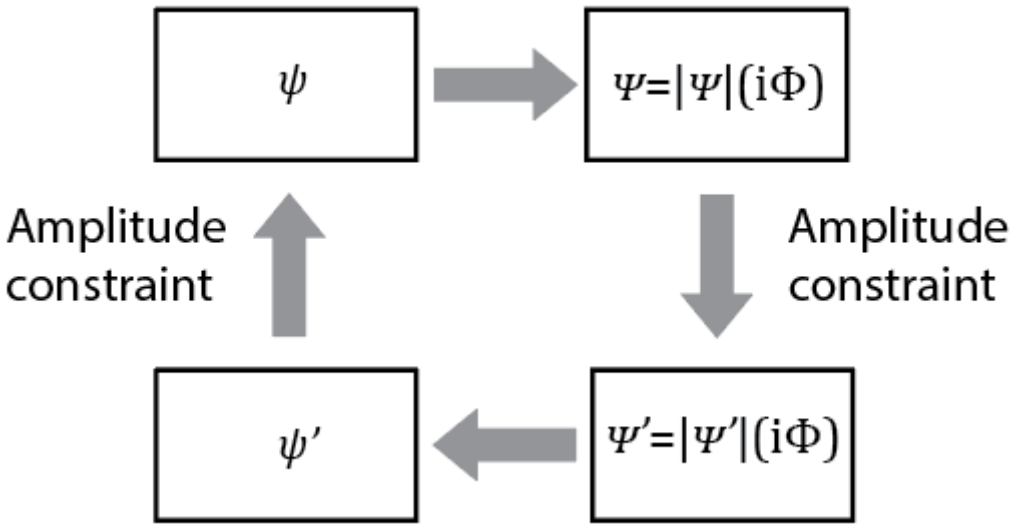

Figure 2.3. the flow chart of generalised iterative reconstruction algorithm.

In 1982, J. Fienup further advanced the GS algorithm by generalising it and introduced the concept of error reduction (ER) algorithm [46] [47]. The ER algorithm applies the support constraint in object domain instead of the modulus constraint, which means any value outside the area set by S will be zeros [47]. The support projector $\mathcal{P}_S$ can be express by Eq. 2.4.

$$\mathcal{P}_S\{\psi(r)\} = \begin{cases} \psi(r) & r \in S \\ 0 & r \notin S. \end{cases} \quad (2.4)$$

The ER algorithm essentially alternates between both modulus and support project. If the current estimation is $\psi_j(r)$ with iteration number j, the next estimation $\psi_{j+1}(r)$ can be updated as

$$\psi_{j+1}(r) = \mathcal{P}_M\{\mathcal{P}_S\{\psi(r)\}\}. \quad (2.5)$$

These advancements marked a pivotal moment in the development of ptychography, paving the way for more efficient and accurate reconstruction algorithms.

Later, this iterative framework has been further adopted by J. Rodenburg for ptychographic reconstruction in 2004, in an algorithm known as the Ptychographic Iterative Engine (PIE) [9] [48], which laid the foundation for modern ptychography. The working principle and the reconstruction process are very similar to the original idea introduced in the GS algorithm, where the phase information is recovered from the intensity measurement. As shown in **Figure 2.4**, a flowchart demonstrates the basic concept and the process of ptychography, and its iterative reconstruction strategy. An object is translated through a confined probe illumination with overlapping positions and the resulting diffraction patterns are then recorded in reciprocal space [9]. The reconstruction process includes two sets of constraints for both real space and reciprocal space. And the iterative process will repeat and update the object estimation until the constraints are met from the diffraction measurement. However, due to the inability in probe update, the performance PIE algorithm is largely dependent on the prior knowledge of the probe [9]. The development iterative phase retrieval algorithm enabled the further advancing of ptychography. The details for the implementation of a ptychography experiment and the iterative reconstruction framework are introduced in Section 2.6.

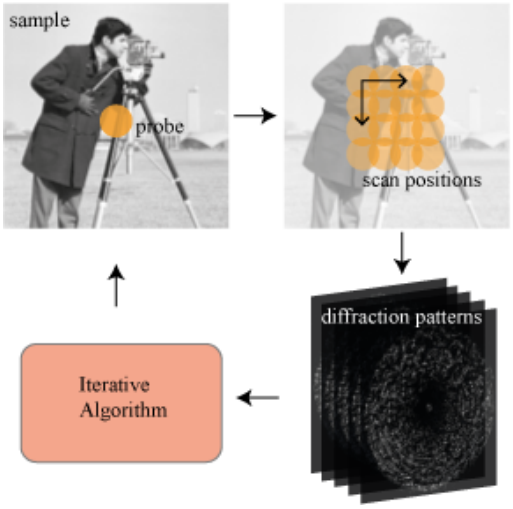

Figure 2.4. Flowchart of the basic principle for ptychography experiment.

The main drawback of PIE algorithm is the requirement of an accurate probe estimation, which can be difficult to obtain. In 2008, M. Guizar-Sicairos and J. Fienup piloted a non-linear optimization approach that enabled the simultaneous recovery of both probe and object [49]. Around the same time, P. Thibault proposed a set projection method based on the Difference Map technique [36] [50]. Shortly thereafter, A. Maiden extended the probe recovery capabilities of the PIE algorithm, resulting in the development of the ePIE algorithm [51].

Since the groundwork of X-ray ptychography demonstrated by J. Rodenburg in 2007 [10] and P. Thibault in 2008 [52], coupled with the ongoing advancement of all those robust reconstruction strategies mentioned above and rapid development of computational power, ptychography has shown great potential in producing high resolution images, and has therefore garnered significant attention within the wider research community.

M. Dierolf's work in 2010 successfully merged X-ray ptychography with X-ray tomography, achieving nano-resolution [14]. This powerful combination allowed the first 3D reconstruction of samples using the so-called ptycho-tomography method. In 2012, A. Maiden adopted a multi-slice model for ptychography [2]. This pioneering approach enabled the reconstructions of 3D volume with extended depth from single projection and addressed complex multi-scattering process. This will be discussed in detail in Section 2.9.2.

In 2013, two new ptychography variants were introduced. M. Stockmar demonstrated X-ray ptychography in the near-field regime utilising speckled illumination, as an alternative to X-ray inline holography [20], and G. Zheng introduced Fourier ptychography, which shifts data collection and the reconstruction process to the Fourier domain. Notably, Fourier ptychography surpasses the diffraction limit and enables super-resolution image reconstruction [13] [53].

More recently, major developments have been reported via electron ptychography microscopy. Y. Jiang's work in 2018 achieved sub-ångström resolution for 2D material using electron ptychography for the first time [54]. In 2021, Z. Chen demonstrated the ability of electron ptychography to overcome the resolution limited by atom lattice vibration, even for a thick sample, via the multi-slice method [1]. As recently as 2024, K Nguyen achieved sub-half-ångström resolution using electron ptychography without the need for aberration correctors [55].

2.5. Common ptychography experimental configurations

Generally speaking, the formation of diffraction patterns or the intensity measurements in ptychography can be modelled in relation to its object and probe functions [12]. In this section, the three most common ptychographic experiment configurations are introduced [12]. Then the recent development and implementation of near-field ptychography will be introduced.

2.5.1. Conventional ptychography with modulated illumination

Figure 2.5(a) shows one of the most conventional configurations for ptychography – far-field ptychography [11]. A confined probe is formed and projected onto a sample. A detector is then placed in the "far-field" region for data collection. During data acquisition process, the object $O(r)$ is moved laterally to the jth position $O(R_j)$, with overlap in the illuminated region to the previous position. Here, r represents real space coordinate (x, y) and u is the corresponding the 2D reciprocal coordinate. The resulting exit wave from the sample then

propagates to the far-field. Consequently, the corresponding jth diffraction pattern $I_j(u)$ is measured in by the detector, and can be described as the complex transfer function in Eq. 2.6:

$$I_j(r) = \left|\mathcal{F}\{O(r - R_j) \cdot P(r)\}\right|^2. \quad (2.6)$$

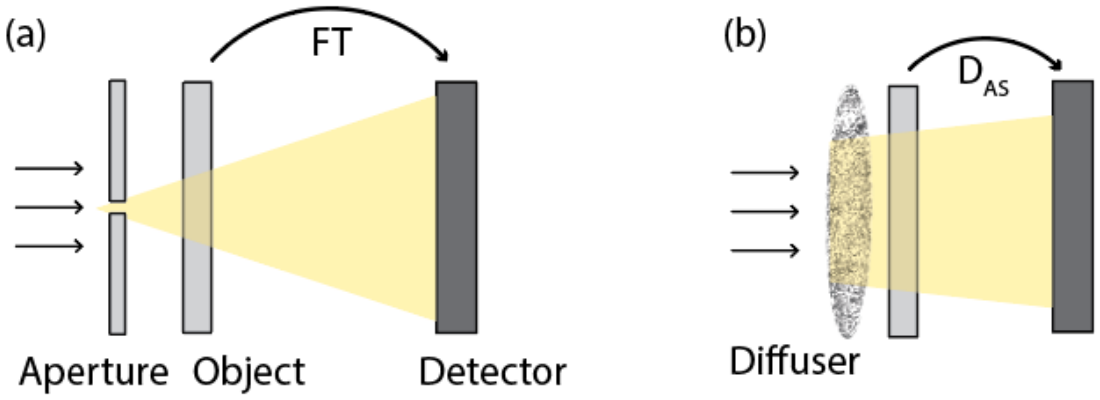

Figure 2.5: Experimental configuration type 1 - modulated illumination ptychography. a) conventional far-field ptychography. b) near-field ptychography with modulated illumination.

Near-field ptychography [20] is alternative form of modulated illumination ptychography, as shown in **Figure 2.5(b)** can be adapted from far-field ptychography by replacing the small aperture with a diffuser, similar to in-line holography. Additionally, the detector is positioned much closer to the sample to capture full-field near-field diffraction patterns. Detailed discussion for near-field ptychography can be found in Section 2.8.

2.5.2. Ptychography with modulated detection

An example experiment configuration for "modulated detection" ptychography is demonstrated in **Figure 2.6** [56] [57]. In this setup, the positions of the object $O(r)$ and the diffuser $S(r)$ are swapped, such that the sample information is modulated by the diffuser speckles. The main benefit of this configuration is the ability to divert the large angle diffraction from the object into smaller, detectable angles, which are redirected by the

speckle field [12] [56]. Essentially, the high-frequency information in the object is physically down-sampled by the diffuser modulation into low-frequency components.

In this configuration, instead of direct recovery of the illumination probe, the wavefront exiting the diffuser plane is recovered. The transmission function of the speckle field is $S(r')$, and the corresponding forward model of the recorded intensity is:

$$I_j(r'') = \left|D_{AS_{d2}}\{D_{AS_{d1}}\{O(r - r_j)\} \cdot S(r')\}\right|^2, \tag{2.7}$$

where D_{AS} is the angular spectrum propagator over distance d_1 or d_2, r' and r'' are coordinates at the initial and secondary propagation planes. The secondary propagation from the modulator to detector can be adapted for far-field configuration. However, it is crucial that the diffuser layer is required to be sufficiently thin in order to satisfy the projection approximation model. In this case, the diffuser plane can also be treated as an equivalent probe in conventional ptychographic reconstruction [12].

Typical implementations for this configuration include aperture-plane modulation ptychography [58], and detector modulation ptychography [56] [59].

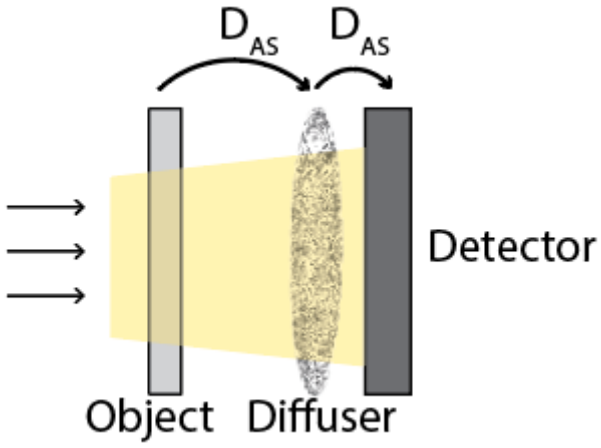

Figure 2.6: An example experimental configuration type 2 - modulated detection ptychography. The transmission function of the sample is propagated and modulated by a diffuser. Then the exit wave from the diffuser is propagated to the detector plain.

Both modulated illumination and modulated detection ptychography can be implemented on a conventional microscope [12]. In such setup, the original transmission function convolutes with the PSF of the objective lens. An example of such a configuration with modulated ptychography is shown in **Figure 2.6**. The intensity measured at the detector plane is derived from the forward propagation and can be expressed as

$$I_j(r) = \left|\left\{D_{AS}\left\{O\left(r - r_j\right)\right\} \cdot\ S(r')\right\} * PSF_{obj}\right|^2. \qquad (2.8)$$

Where "*" denotes to the convolution operator.

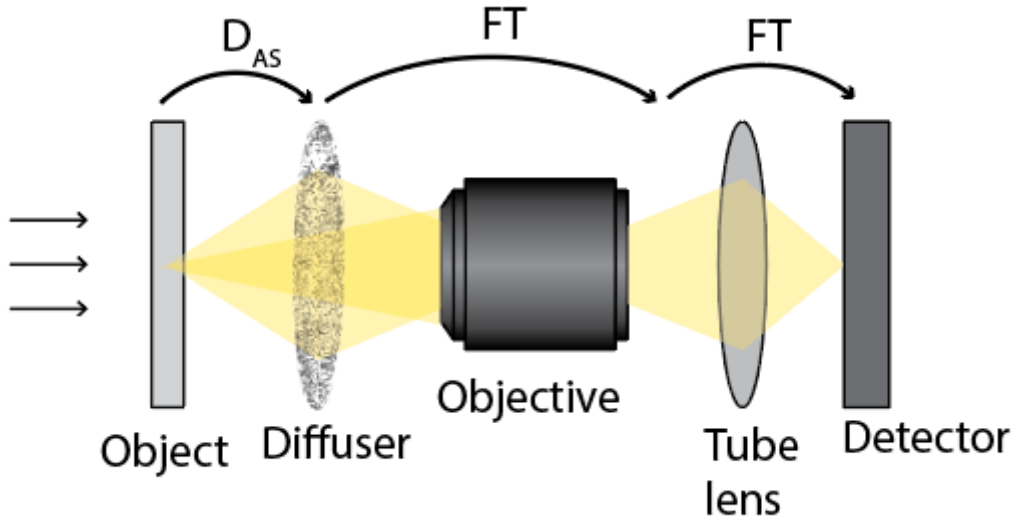

Figure 2.7: An example experimental configuration type 3 - modulated detection ptychography with additional microscopy system.

Example implementations of this configuration include selected area ptychography [60] and optical near-field ptychography [61].

2.5.3. Fourier ptychography

Fourier ptychography is an alternative ptychographic system built upon a regular microscope system, with the systematic configuration shown in **Figure 2.7** [12] [13] [53]. Unlike conventional ptychography, Fourier ptychography involves the conversion of reciprocal space and real space through a microscopy system [13] [53].

In Fourier ptychography, the illumination source usually comprises a programmable LED array. The sample is positioned at the object plane $O(r)$ and object is transformed by the objective lens into its Fourier spectrum, where an aperture is placed, represented by a pupil function $Pupil(u)$. Then a secondary Fourier transform occurs, and propagates the object's spectrum exiting the aperture to the real-space image plane (r).

The object $O^j(r)$ is illuminated by each sequential jth position of the LED, the resulting image can be model as

$$I_j(r) = \left|\mathcal{F}^{-1}\left\{\mathcal{F}\left\{O^j(r)\right\} \cdot Pupil(u)\right\} * PSF_{obj}\right|^2. \quad (2.9)$$

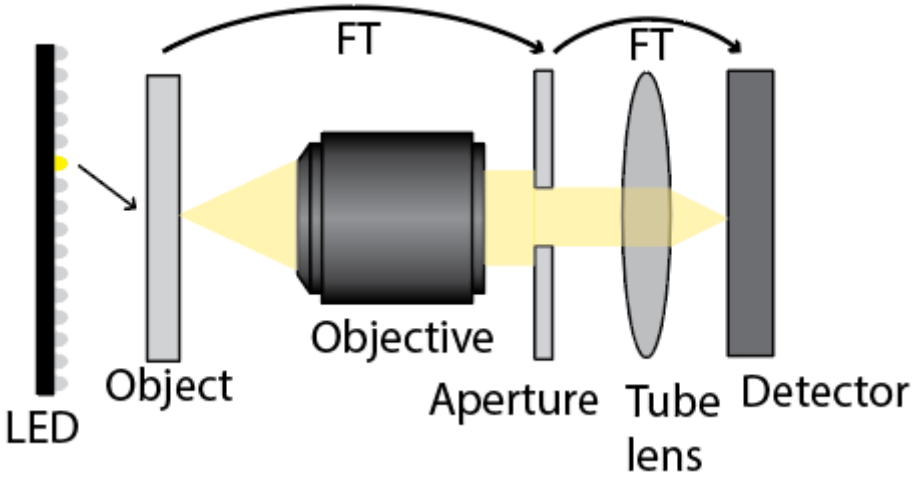

Figure 2.8: Experimental configuration type 4 - Fourier ptychography.

In Fourier ptychography, the space-bandwidth product is determined by both the NA of the illumination and the NA of the objective lens [62] [63]. Consequently, the achievable resolution exceeds the limitations imposed by the NA of the objective lens alone. This property enables Fourier ptychography to achieve high resolution even when using an objective lens with a low NA. Additionally, Fourier ptychography benefits from a large FoV of the low NA objective lens, further enhancing its versatility and applicability in imaging tasks.

2.6. Ptychographic Iterative Engine

With recent advancements in ptychography, a multitude of reconstruction techniques have been developed to extract phase images from ptychographic data. Among the most widely implemented algorithms are ePIE [51], Difference Map (DM) [50], Conjugate Gradient (CG) [49], Relaxed Averaged Alternating Reflections (RAAR) [64], Alternating Directions Method of Multipliers (ADMM) [65], and Maximum Likelihood (ML) [66]. However, only PIE family algorithm is implemented and discussed in this thesis.

In this section, the detailed implementation of the PIE family algorithm is introduced, which forms the backbone of many ptychographic reconstruction methodologies. For a comprehensive understanding, readers can refer to the original ePIE paper [51]. Additionally, two further variations are introduced in this section: regularised Ptychographic Iterative Engine (rPIE) [67] and Weighted Average of Sequential Projections (WASP) [68], each offering unique advantages in the realm of ptychographic reconstruction.

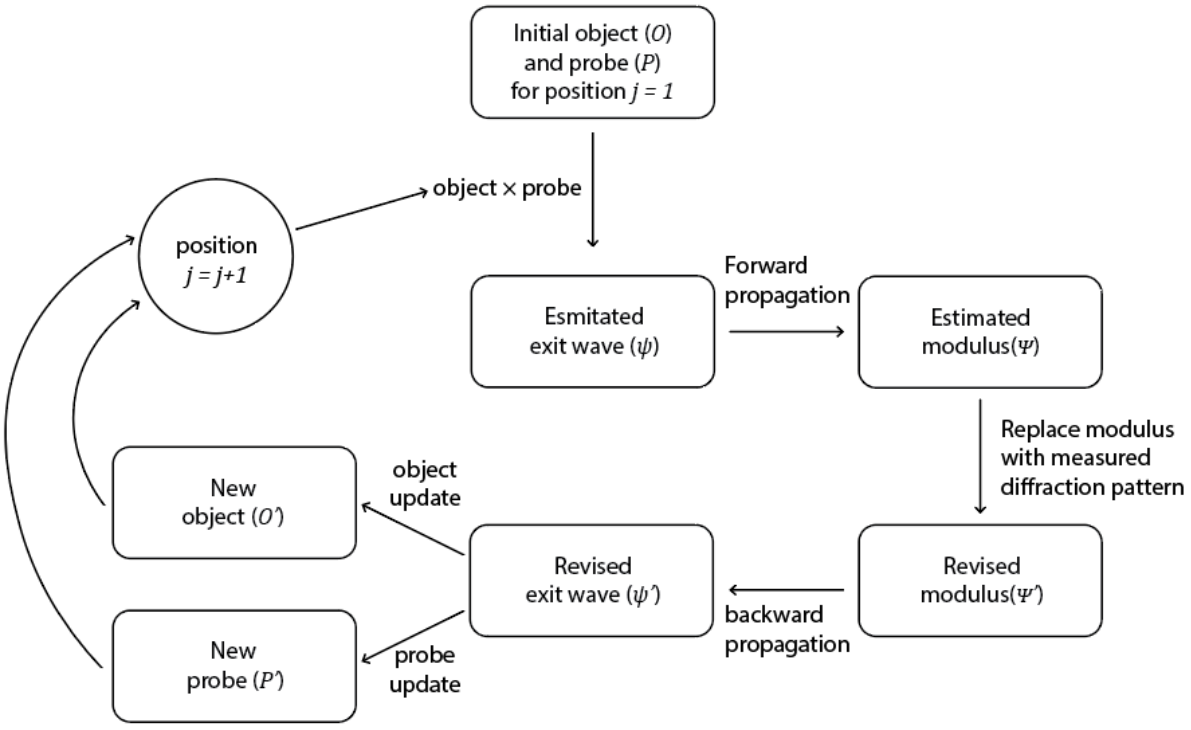

Figure 2.9: The flow chart of ePIE algorithm. PIE algorithm follows the same process but without the probe update part of the flow chart.

In comparison to the PIE algorithm, the main difference and improvement of ePIE is the ability to achieve blind deconvolution, where both probe and object function can be reconstructed simultaneously [51]. Hence, the prior knowledge of the probe no longer significantly affects the reconstruction performance. The flowchart of ePIE algorithm is demonstrated in **Figure 2.9**.

The typical ptychography experimental procedure follows the below steps [68]:

1. A transparent specimen is illuminated by a coherent radiation source.
2. The exit wave from the specimen propagates a distance to the detector plane and form a diffraction pattern (either far-field or near-field).
3. The intensity measurement of the corresponding diffraction pattern is recorded by a pixellated detector.
4. The sample is transited laterally to the next position with overlap to the previous illuminated region.
5. Step 1-4 are repeated until all the diffraction patterns corresponding to the region of interest on the object are recorded.

The forward model for a ptychographic experiment is demonstrated in **Figure 2.10** [11] [68]. The exit wave from the object can be modelled as the multiplication of a probe matrix $P(r)$ and the object box $o(r)$, where $r = (x, y)$. A larger object matrix O_X is used to represent the full sample size of $[X, Y]$ and the position of the top left pixel of the object box is defined as $[1,1]$. The position of the top left pixel of the object box is denoted by R^{tl} and the position corresponding bottom right pixel of the object box is denoted by $R^{br} = R^{tl} + [x, y] - [1,1]$.

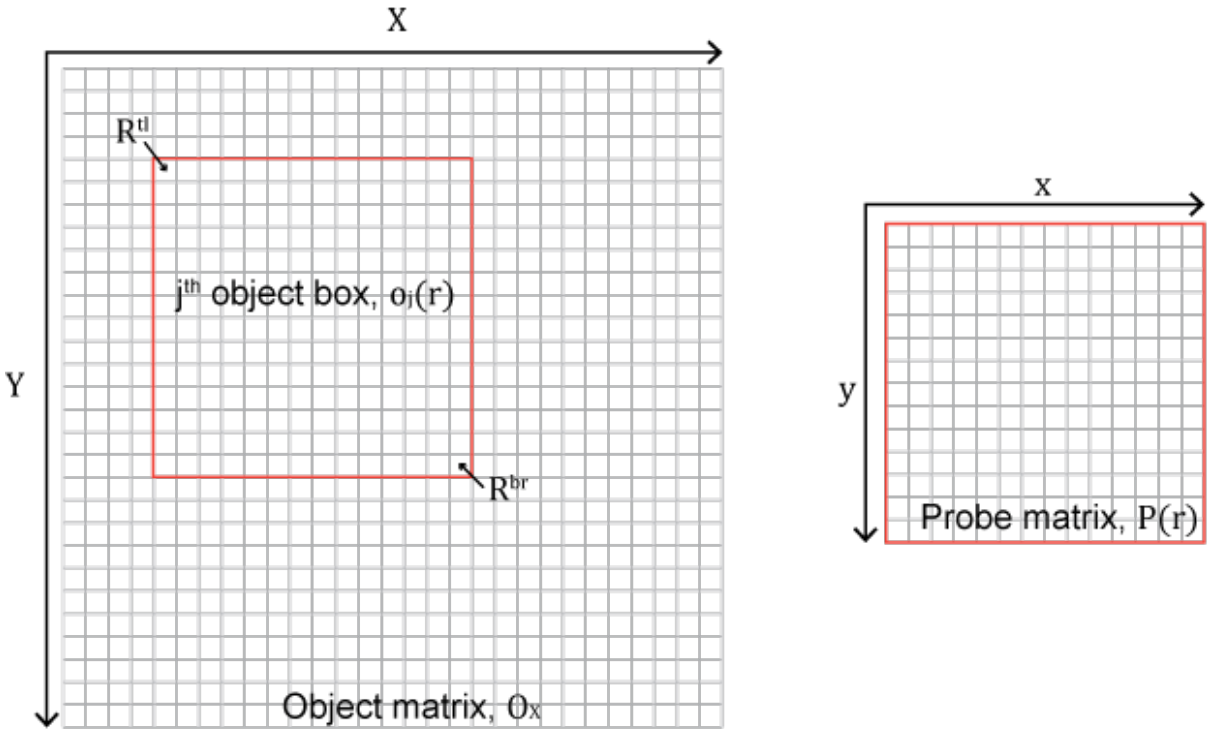

Figure 2.10. Implementation of the computational model for a ptychography experiment

For the jth ptychographic scan, the position of the object box is translated to lateral distance offset of R_j^{tl}, corresponding to the region $O\left(r + R_j^{tl}\right)$ of the object matrix. Following the flowchart in **Figure 2.9**., the iteration of ePIE algorithm is described below.

1. The process initiates with a randomly selected diffraction pattern recorded at a sample position j to avoid any bias toward the initial condition at the specific location or anomaly (e.g. weak signal or missing frequencies) from the first probe position. The exit wave at this position is modelled as a product of the object and probe's complex function, known as the multiplicative approximation for 2D ptychography:

$$\psi_j(r) = P(r)O\left(r + R_j^{tl}\right). \qquad (2.10)$$

2. Subsequently, this exit wave is propagated to the detector plane:

$$\Psi_j = D_\Delta\{\psi_j\}, \tag{2.11}$$

where D_Δ is either the near-field or Fourier propagator and Ψ is the corresponding wavefront at the detector plane.

3. Then the first constraint is applied, where the estimated modulus is corrected by the measured diffraction pattern $I_j(u)$

$$\Psi_j'(u) = \sqrt{I_j(u)}\frac{\Psi_j(u)}{|\Psi_j(u)|}. \tag{2.12}$$

4. This corrected wavefront is then back-propagated to the object plane and a revised estimation of the original wavefront can be computed as:

$$\psi_j'(r) = D_\Delta^{-1}\{\Psi_j'(u)\}. \tag{2.13}$$

5. Then the new estimation of both object and probe are updated using the **ePIE** update functions. The update function is shown in a combined form with a single tuning parameter α for simplified presentation:

$$U[f(r), g(r), \Delta\psi(f)] = f(r) + \alpha\frac{g^*(r)}{|g(r)|^2_{max}}\Delta\psi(r), \tag{2.14}$$

$$\Delta\psi(r) = \psi_j' - \psi_j. \tag{2.15}$$

Where $f(r)$ and $g(r)$ represent either probe or object function and "*" denotes the complex conjugate of its original value.

The updated probe and object are:

$$P'(r) = U\big[P(r), O\big(r - R_j\big), \Delta\psi(r)\big], \tag{2.16}$$

$$O'\big(r - R_j\big) = U\big[O\big(r - R_j\big), P(r), \Delta\psi(r)\big]. \tag{2.17}$$

One iteration of the process involves repeating the aforementioned steps for all recorded diffraction patterns. The entire process repeats for any desired number of iterations or until the error, evaluated by sum of squared errors (SSE) (see Section 2.7.3) becomes sufficiently small.

rPIE:

Regularised Ptychographic Iterative Engine (rPIE) is further improved upon ePIE algorithm[67], where the weighting function of the update function was regularized. As a result, rPIE shows its superiority through quick convergence and better stability in comparison to the PIE and ePIE algorithms.

The combined form of the rPIE update function is shown below:

$$U[f(r), g(r), \Delta\psi(f)] = f(r) + \frac{g^*(r)}{(1-\alpha)|g(r)|^2 + \alpha|g(r)|^2_{max}} \Delta\psi(r), \qquad (2.18)$$

where the tunning parameter α can adapt to different value for probe and object update.

WASP:

Weighted average of sequential projections (WASP) is a newly developed algorithm which benefits from the advantages from both sequential projection algorithms and weighted average or ptychographic error reduction (ER) algorithms [68]. It shows robust initial convergence, and it can be operated in parallel. The main idea of WASP is to utilise the outputs - revised exit waves, from sequential projection algorithms, such as ePIE and rPIE, to accelerate and enhance the performance of ER algorithms [68].

For the implementation of the "ER" part of the algorithm [47] [68], it is useful to embedded probe matrix into the larger matrix $[X, Y]$ as shown in **Figure 2.10**, to calculate the accumulation of probe intensity for all the illuminated pixels in the object matrix. Similar to the embedding process for the object box mentioned previously, the jth embedded probe matrix P_{jX} can be modelled as:

$$P_{jX} = \begin{cases} P\left(r - R_j^{tl}\right) & R_j^{tl} \le x \le R_j^{br} \\ 0 & otherwise. \end{cases} \qquad (2.19)$$

The update functions for this ER algorithm are summarised below:

$$P'(r) = \frac{\sum_j o_j^*(r) \cdot \psi'(r)}{\sum_j |o_j(r)|} = \frac{\sum_j |o_j(r)|^2 \cdot \left(\frac{\psi_j'(r)}{o_j(r)}\right)}{\sum_j |o_{jr}|^2}, \qquad (2.20)$$

$$O'_X = \frac{\sum_j P^*_{jX} \cdot \psi'(r)}{\sum_j |o_j(r)|} = \frac{\sum_j |P_{jX}|^2 \cdot \left(\frac{\psi'_j(r)}{P_{jX}}\right)}{\sum_j |P_{jX}|^2}. \quad (2.21)$$

Where the $\frac{\psi'_j(r)}{P_{jX}}$ and $\frac{\psi'_j(r)}{o_j(r)}$ are equivalent to the estimation of jth object box and probe estimation from the jth diffraction pattern measurement respectively.

2.7. Extension for ptychography reconstruction

2.7.1. Position correction

The relative position change between the object and the illumination is one of the key requirements for ptychographic reconstruction. The position acquisition is determined by feedback from the translation stage used in the experiment. However, achieving an accurate position record can be challenging due to various factors such as optic axis misalignment, system magnification discrepancies, sample stage drift, and inherent inaccuracies in the stage itself. To mitigate these challenges, ptychography often employs an annealing algorithm, sometimes referred to as the "Jiggle" method, for position correction [69]. This algorithm operates iteratively, systematically exploring different potential positions within a small search radius for each diffraction pattern. During each iteration, the algorithm evaluates the error associated with each tested position and compares it to the original position. The position yielding the lowest estimated error is then selected as the correct position. This process of evaluating and adjusting positions can be repeated over multiple iterations until the changes in position become negligible, ensuring optimal alignment between the object and the illumination. By employing such iterative position correction algorithms, ptychography can effectively compensate for positional inaccuracies and improve the overall effectiveness of the reconstruction process.

2.7.2. Reconstruction for state mixtures

The success of conventional coherent diffractive imaging (CDI) techniques hinges largely on the availability of a highly coherent and stable radiation source, necessitating stringent experimental conditions. In ptychography reconstruction there are three main factors that contribute to decoherence, which are partial coherence of the radiation source, object interaction and the point spread of the detector. These factors introduce challenges to the coherence of the imaging process, potentially leading to inaccuracies or ambiguities in the reconstructed images.

Mixed-state reconstruction for ptychography was initially introduced by P. Thibault in 2013 [70] and it is one of the mostly implemented methods for ptychography reconstruction [71] [72]. By decomposing the original probe illumination into multiple sub-probes, the imaging system gains increased robustness against fluctuations or instabilities in the illumination source.

As an example [70], the measure intensities with the implantation of k probe modes with jth scan position is

$$I_j = \sum_{k,l} \left| D\{\varphi_j^{k,l}\} \right|^2 \qquad (2.22)$$

Where φ_j^k represents the new sets exit waves $\varphi_j^k(r) = P^k(r)O^l(r - R_j)$, P^k and O^l is the corresponding probe states and object states; D represents either near-field or far-field propagator.

The implementation of state mixture reconstruction for ptychography effectively leverages the versatility of ptychographic techniques to achieve improved imaging performance in various experimental conditions [70] [72].

2.7.3. Error metric

The accuracy and the performance of ptychographic iterative algorithm reconstruction can be monitored using an error metric – the sum squared error (SSE) [67], which is used to

evaluate the error induced between the diffraction pattern recovered with estimation and the measured diffraction pattern at the jth position after each iteration.

$$SSE = \sum_j I_j(u) - \left|\Psi_j(u)\right|^2 \quad (2.23)$$

The lower value calculated from the SSE indicates a more accurate result in comparison to the measured intensity. However, in reality the noise induced during the diffraction pattern measurement in unavoidable, which means the measurement itself may pose degrees of error, such as the incoherent signal in the diffraction pattern measured due to inelastic scattering.

2.8. Near-field ptychography

Near-field ptychography amalgamates the principles of conventional far-field ptychography and inline-holography. It was pioneered by M. Stockmar in 2013 [20] [73]. The experimental configuration for near-field ptychography is shown in **Figure 2.5(b)**. In this configuration, the detector is moved much closer to the sample, to the near-field regime. Instead of using an aperture to form a confined illumination, this incident beam is now modulated by a speckle-field $P_m(r)$, where the subscript m denotes to a modulated field. In addition, the illumination extends to the full-field of the sample and usually covers the entire detector. Following the same data acquisition process, the intensity of the diffraction pattern is now recorded in the image plane positioned in the near-field region, which can be modelled via the angular spectrum propagator D_{AS} Therefore, similarly to conventional far-field ptychography, the intensity of the image with the near-field setup (modulated illumination) can be described as:

$$I_j(r) = \left|D_{AS}\{O(r - r_j) \cdot P_m(r)\}\right|^2. \quad (2.24)$$

As demonstrated in various ptychographic implementations, a strong speckle-modulated field can substantially enhance the signal-to-noise ratio and even offer the potential to

surpass the diffraction limit of a lens [12]. However, in near-field ptychography, the modulation introduced by speckle field is particularly crucial [20]. To see why this is important, imagine a ptychographic scan is performed using a completely uniform illumination – there would be no extra information apart from the lateral position changed between each scan [20]. In far-field ptychography, even with a uniform illumination, sufficient phase retrieval is possible due to the inherently rich angular diversity from Fraunhofer diffraction condition. In addition, the overlapping probe positions in real space translate to overlapping regions in Fourier space which also enhances the redundancy in the dataset. In near-field, the probe overlaps do not directly translate to Fourier redundancy. The diffraction intensities do not change significantly with small lateral shifts if the probe is uniform. The use of a diffuser creates speckle field that interferes with the sample and encodes more diverse frequency information in the diffraction patterns.

The main benefits of near-field ptychography are the large FoV and a successful reconstruction can be achieved with as few as 4 diffraction patterns, and that the relatively uniform illumination characteristic of the near-field regime relaxes the requirement for detector dynamic range, streamlining the experimental setup [74]. However, the main drawback of near-field ptychography is the limited resolution imposed by detector pixel size: near-field ptychography does not extend resolution beyond the probe-forming optics in the same way that far-field ptychography does.

Near-field ptychography is also commonly implemented in a modulated detection configuration, where the modulator functions as an effective probe. Such implementation was demonstrated by S. Jiang via an on-chip lensless near-field ptychography system [56], where the modulation layer is implemented in the fashion of configuration shown in **Figure 2.6**. S. McDermott incorporated a microscopy system for near-field ptychography and position the modulator at the corresponding microscope image plane [61]. Y. Zhang further adapted this configuration and demonstrated a near-field ptychography add-on, designed for a conventional microscope using a rotational diffuser [75]. Furthermore, H. Zhang demonstrated the possibility to implement Fourier ptychography in the near-field regime [76].

While showing success in both X-ray and optical setups, the near-field configuration has also been trialled in electron ptychography. The first implementation of electron near-field

ptychography was reported by A. Maiden in 2015, where select area aperture mode was used to form a “virtual” ptychographic probe [77]. However, the Fresnel number in this setup was relatively small – approximately 17.2, indicating that the system operates under conditions closer to the Fresnel regime. In 2020, F. Allars further improved the near-field condition by increasing the Fresnel number to approximately 412 by decreasing the sample detector distance via defocused probe configuration [78]. In addition, instead of using the selected aperture mode, the near-field diffraction patterns were formed using a defocused, full-field illumination, with a silicon nitride phase diffuser trialled to generate speckled illumination [78]. Later in 2023, S. You demonstrated near-field electron ptychography Lorentz mode using an amplitude diffuser. This configuration offers more experiential flexibility and reduces inelastic scatter effect [79]. The reconstruction results from his experiment exhibited several advantages over electron holography, including large FoV and relaxed experimental condition.

2.8.1. Implementation of near-field ptychography

In this section, several key elements particularly important for near-field ptychography experiments and reconstruction are introduced.

2.8.2. Experimental parameters for near-field ptychography:

1. **Scan patterns**. This is the term that refers to the specific path for the illumination to follow during a scan route through the sample. There are two commonly used scan patterns for regular step scans [80]:
    a. **Raster scan.** In this pattern, the probe moves in a regular line-by-line manner across the sample. However, the regular scan grid can induce stripes or grid like artifacts due to the periodic nature of the scan. In order to mitigate the artefact, random shifts between positions can be used to disrupt the grid pattern. Alternatively, these grid artefacts can also be removed with specific image processing procedures [81] [82].
    b. **Fermat spiral scan.** This type of scan pattern offers improved coverage uniformness and higher overlap ratio between each two adjacent scan points.

Furthermore, it inherits the aperiodicity from the normal spiral scan path which can eliminate the artefact which appears in regular grid scan [80]. However, due to the high overlap ratio, this scan pattern has a relatively smaller FoV and it is considered less dose efficient.

2. **Step size/ Overlap.** "Step size" refers to the distance moved between two adjacent scan points and overlap refers to the actual percentage of the overlaying diameter between each two illuminations. 0% overlap means each scan pattern is independent therefore no redundant information can be obtained. 100% overlap means there is no shift in position between each scan, therefore there is no "diversity". Generally speaking, an overlap over at least 70%-80% is required to achieve a high-quality ptychographic reconstruction [83] [84]. In near-field ptychography, a higher overlap scan typically results in a higher signal-to-noise ratio in the reconstruction and the choice of step size is directly related to the speckle size of the diffuser used in the experiment [74].

3. **Camera distance (Δ) and effective propagation distance** (Δ_{eff})**.** Camera distance is the absolute propagation distance between the most downstream sample plane and the detector. Effective propagation distance is calculated using Eq. 2.25, where the cone-beam geometry is converted into a parallel-beam geometry via Fresnel scaling theorem [22],

$$\Delta_{\mathrm{eff}} = \frac{\Delta}{\mathrm{M}}. \qquad (2.25)$$

4. **Pixel size (**dx**) and effective pixel size** (dx_{eff})**.** Pixel size is the physical dimension size of a single pixel on the detector. Similarly, to the effective propagation distance, the effective pixel size dx_{eff} is the equivalent pixel size calculated using cone-beam geometry with magnification M [22],

$$dx_{eff} = \frac{dx}{M}. \qquad (2.26)$$

5. **Exposure time and Frame averaging**. These two parameters can be considered together as important factors that determine the overall data quality and also the total radiation dose to which the sample is exposed. Exposure time refers to the time taken for the detector to record one diffraction pattern. Frame averaging means the number of times this process is repeated for each scan point, with the resulting series of frames averaged to produce a single lower noise diffraction pattern. Higher exposure time usually means the ability to capture a stronger signal (without over exposure). A higher number of averaging can help to stabilise and reduce the noise in the data. However, both parameters need to be considered within the time constraint of the experiment and the radiation sensitivity of the sample.

6. **Darkfield.** This is a measurement recorded for background correction, where the direct illumination source is blocked. This background measurement, known as the darkfield, helps to account for and eliminate any unwanted background noise. By subtracting the darkfield data from each individual diffraction pattern, the influence of the background is minimised, leading to cleaner, more accurate diffraction information. This technique is often used to enhance the signal-to-noise ratio in the data.

2.8.3. Equivalent geometry for cone-beam configuration

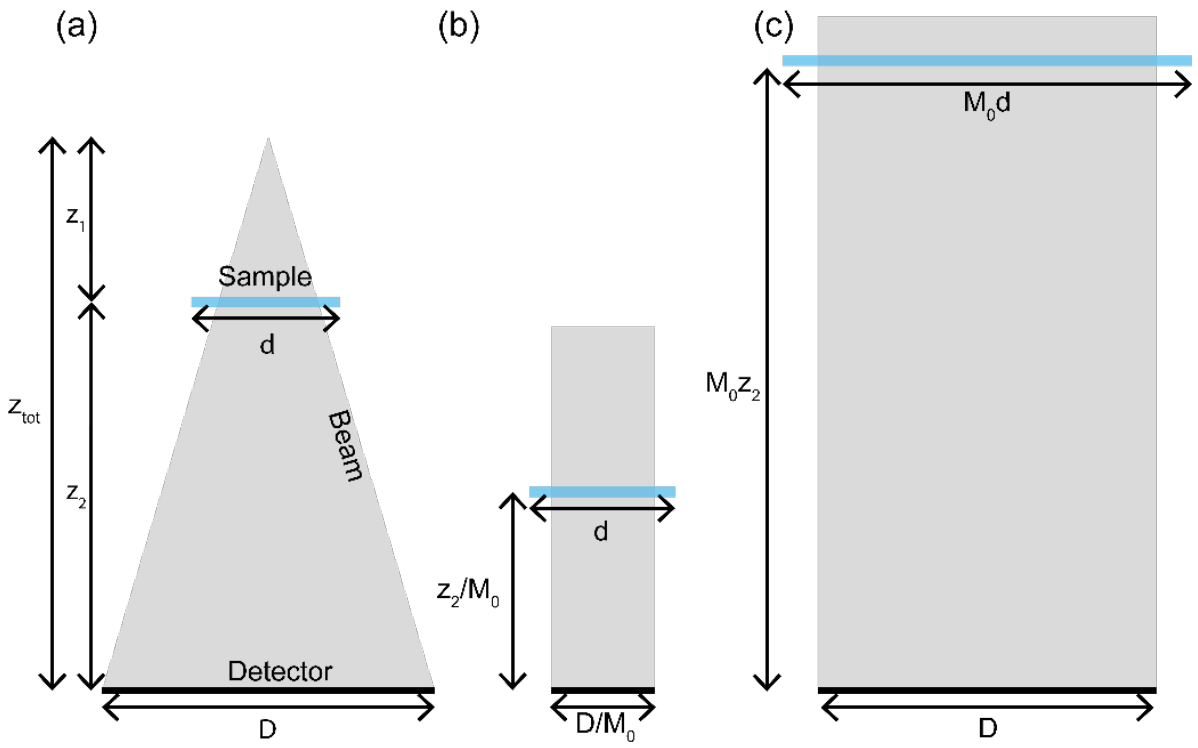

Figure 2.11: Two equivalent plane-illumination models for the cone beam geometry. a) the cone beam arrangement: the detector is of width D, d is a representative distance at the sample surface, z_1 is the distance from the cone beam focus to the sample, and z_2 is the distance from the sample surface to the detector. b) provided the small angle approximation is valid, the cone beam can be modelled by an equivalent plane-illumination setup, where the detector is imagined to be smaller and positioned nearer to the sample. Both the detector and the sample-detector distance are scaled down by the geometric magnification, given by $M_0 = \frac{z_1+z_2}{z_1}$.

In order to overcome the resolution limit imposed by the physical pixel size of the detector, near-field ptychography is usually performed in a cone-beam geometry, as shown in **Figure 2.11(a)**.

In this geometry, the beam propagates a distance z_1 from the cone apex (at the focus of up-beam optics) to the sample, passes through, and propagates a further distance z_2 to a detector. The detector records the resulting diffraction pattern, which in this regime extends across its entire width, D. As with conventional ptychography, a full near-field ptychographic data set comprises a series of these diffraction patterns, collected over a grid of sample

positions; work by Clare *et al* studied the technique in detail, assessing the effect of diffraction pattern speckle size and different position grids on eventual image quality [74].

The iterative algorithms that reconstruct images from data collected in this cone beam geometry require an appropriate forward model of the experiment, which can be derived from the Fresnel scaling theorem (FST) [22]. The FST shows that, subject to the paraxial approximation, the cone beam geometry produces data identical to an equivalent experiment where the incident beam is assumed planar, rather than curved, as shown in **Figure 2.11(b**). In this plane-illumination geometry, both the distance from the sample to the detector, z_2, and the size of the detector, D, are shrunk by the geometric magnification, M_0, of the cone beam, where:

$$M_0 = \frac{z_1 + z_2}{\mathrm{z}_1} = \frac{z_{tot}}{z_1}. \qquad (2.27)$$

This equivalence means that, as far as the reconstruction algorithm is concerned, it is as if the experiment were carried out with a structured, but flat (non-expanding) source of illumination and with a smaller detector placed closer to the sample. This is a straightforward model to implement digitally since it avoids the need to explicitly sample the beam curvature, which can cause aliasing. With the help of the FST, conventional ptychographic algorithms can reconstruct images from cone-beam data with only three minor modifications:

1. Replace the conventional far-field propagation model (a single FFT) with a two-FFT angular spectrum propagator [21],
2. Reduce the propagation distance used in that propagator by a factor of M_0, from z_2 to $\frac{z_2}{M_0}$,
3. Model the smaller camera by reducing the pixel pitch used in the reconstruction from dc, the real-world pixel pitch of the detector, to $\frac{dx}{M_0}$.

The first of these changes requires some small code changes to the algorithms, but the second and third are pre-processing steps requiring only changes to the algorithm input parameters.

Importantly for the work shown in this thesis, there is a less well-known second equivalent plane-illumination geometry, shown in **Figure 2.11(c)** [85]. Here, rather than shrinking the detector, the sample is expanded by M_0, and rather than reducing the sample-detector distance, z_2, it is increased by the same factor: it is now as if the experiment were carried out with a larger facsimile of the sample, placed further away from the detector. This second equivalent geometry requires similar minor adjustments to conventional ptychographic algorithms:

1. Replace the conventional far-field propagation model with the angular spectrum propagator as before,
2. Increase the propagation distance used in that propagator from z_2 to $z_2 M_0$,
3. Use Eq. 2.28 to convert the scan positions measured from the sample translation stage, $r_{x,y}$ (in metres), to pixel offsets $r_{m,n}$ in the matrix representing the reconstructed sample image:

$$r_{m,n} = \frac{M_0}{dx} r_{x,y} \tag{2.28}$$

Again, the first requirement involves small changes to the code whilst the second and third only involve changes to the algorithm input parameters.

There are no computational differences between the two methods of implementing the FST – their propagation kernels and thus their outputted images are identical. Only the frame of reference changes, with the first method using the sample as the reference frame and the second using the detector. This is inconsequential for 2D ptychography, but when it comes to multi-slice ptychography the less well-known method of keeping the detector as the fixed frame of reference, and therefore not having to change the pixel pitch, will prove easier to implement.

2.9. Ptychography for volume imaging

Volumetric ptychography is the extension of the conventional 2D ptychographic method to imaging for 3D volumes. Two primary configurations for volume ptychography are the rotation-based or tilt-based method - ptycho-tomography [14], and the propagation-based

method – multi-slice ptychography. Both methods will be introduced in the following sections, with the focus on multi-slice ptychography.

2.9.1. Ptycho-Tomography

Tomography is a non-invasive 3D imaging technique that uses set of 2D projection data recorded at different rotation angle to reconstruct a volumetric image of a sample. This technique is particularly popular among the X-ray community, due to its ability to retrieve the 3D information of a sample in a non-invasive manner. In a conventionally tomography setting, the 2D projections acquired are based on absorption contrast image, therefore, contrast is particularly poor when using highly penetrative X-ray sources as the illumination.

By combining tomography with ptychography, the advantage of high-resolution, high contrast phase image from conventional ptychography is inherited, and it is able to resolve the 3D complexed refract-index map of a sample. This combine technique is often known as Ptycho-tomography [14] [86] [87] .

The experimental configuration for ptycho-tomography is shown in **Figure 2.12** [14]. The data collection and reconstruction procedure of ptycho-tomography starts with acquiring a projection data set using ptychography method at a range of rotation angles, followed by ptychographic reconstruction of these data sets to form a series of projection images, then tomographic combination of these projections into a 3D volume. The following pre-processing steps are required in order to successfully carry out the tomography step:

1. Removing linear phase ramp and offset.
2. Phase unwrapping.
3. Projection position alignment.

Once these preprocessing steps are completed, the phase images reconstructed from various projection angle are processed using standard tomographic reconstruction techniques to generate the 3D sample volume. Detailed implementation and reconstruction framework can be referred to [14].

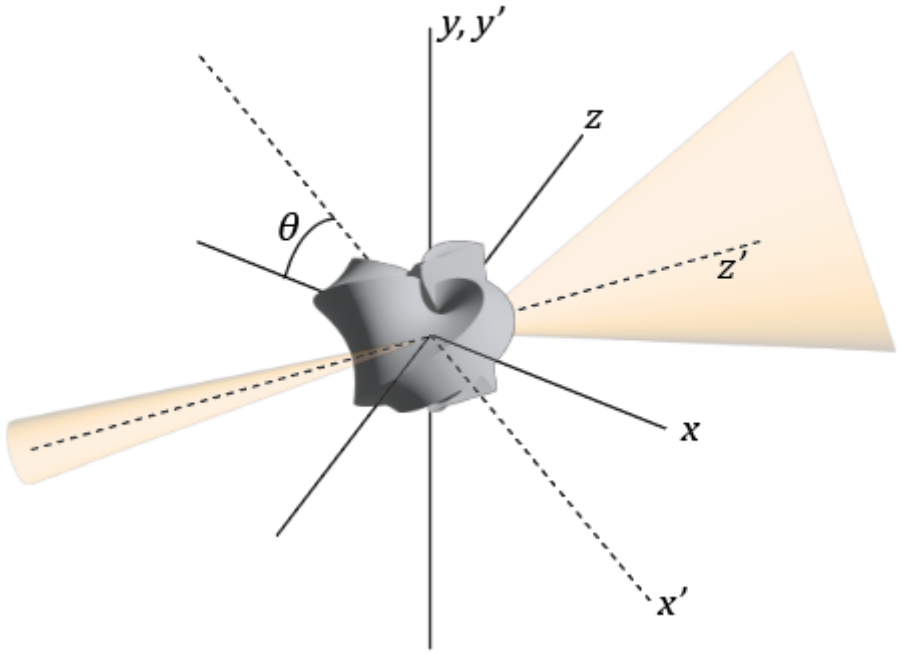

Figure 2.12: Experimental configuration for ptycho-tomography. The sample position is recorded with a real-space coordinate (x, y, z) and the for the tomographic data collection process, a series of ptychographic data set is collection at various projection angle θ and translate to the effective coordinate (x', y', z').

2.9.2. Multi-slice ptychography

The multi-slice model was originally proposed by Cowley and Moodie in 1957 to simulate the scattering of an electron beam for electron microscopy [88] [89]. In 2012, this multi-slice model was adopted by A. Maiden who introduced multi-slice ptychography [2]. Conventional ptychography reconstruction relies on a 2D multiplicative approximation to simulate the interaction between probe and object. However, this approximation is only valid if the sample is optically thin. If the sample is too thick, this approximation will fail due to the neglecting of multi-scattering effects. The multi-slice model essentially solves a complex multi-scattering process by breaking down a thick sample into thin slices in the direction of propagation, where each slice is assumed to be weakly scattering (subject to paraxial approximation) and satisfies the 2D multiplicative approximation. Passage of an X-ray beam through the slices is computed by multiplying the first (most up-beam) slice by the incident

illumination wavefront, to model its interaction with that volume of the sample, then propagating, as if through free-space, to the second slice, and so forth in a series of multiply-propagate steps until the final (down-beam) slice is reached. This approach enables the reconstruction of multiple slices of an object simultaneously along the direction of light propagation. It has drawn great attention in recent years for its ability to break through the DoF limit and achieve improved resolution in comparison to 2D ptychography.

Successful implementation of multi-slice ptychography has been shown with various wavelength. In 2014, T. Godden demonstrated the far-field multi-slice approach with an optical microscopy system and showed the potential to apply the multi-slice approach on an optically thick biological sample, achieving optical-sectioning at micron resolution [90]. In 2015, L. Tian adopted the multi-slice approach for Fourier ptychography and demonstrated the possibility of super-resolution multi-slice ptychography [3]. Later in 2019, S. Chowdhury further improved this work and realised the sub-micron in both lateral and axial resolution [91].

Proof-of-principle experiment of X-ray multi-slice ptychography has also been demonstrated by A. Suzuki in 2014 [4] and E. Tsai in 2016 [92]. However, due to the short wavelength of X-ray, the lateral resolution that can be achieved is significantly better than the axial resolution. Consequently, manipulating the data for the later 3D reconstruction becomes challenging.

The muti-slice model has demonstrated great potential in the field of material science when combined with electron ptychography, with the first proof-of-principle experiment conducted by S. Gao in 2017 [93]. In 2021, Z. Chen showcased the ability of multi-slice model to overcome lens aberrations and multiple scattering in transmission electron microscopy and to achieve the resolution set by thermal fluctuation [1].

In this section, multi-slice ptychography is segmented into two primary categories: the real-space and Fourier space configurations. The implementations for both configuration and reconstruction processes are discussed. Additionally, an alternative 3D scattering model, the multi-layer Born approximation, adapted from the first-Born approximation, is introduced.

2.9.2.1. Multi-slice model for ptychography

The process of multi-slice ptychography starts the same as in conventional 2D ptychography. An incident probe illumination $P(r - R_j)$ is project onto the first slice of the sample $O_1(r)$ with a position offset of R_j, and the exit wave $\psi_{ex,1}$ of this slice can be modelled using the multiplicative approximation of the incident probe illumination and the object's transmission function of the thin slice, where $\psi_{ex,1}(r) = P(r - R_j)O_1(r)$. Now this exit wave from the first slice propagates to the 2nd slice and becomes the new incident probe illumination this slice, and this procedure repeats until the final nth slice is reached.

$$\psi_{ex,n}(r) = D_{\Delta z_{n-1,n}} O_n(r) \left\{ D_{\Delta z_{n-2,n-1}} O_{n-1}(r) \left\{ \dots D_{\Delta z_{2,3}} O_2(r) \left\{ D_{\Delta z_{1,2}} O_2 \{ P(r - R_j) O_1(r) \} \right\} \dots \right\} \right\}, (2.29)$$

$D_{\Delta z_{n-1,n}}$ denotes the free-space propagation over the distance between the $(n-1)$th to the nth slice.

2.9.2.2. real-space multi-slice ptychography

The 3PIE algorithm incorporate this multi-scattering process with conventional ptychography iterative algorithm. **Figure 2.13** demonstrates both forward and backward model for 3PIE algorithm. The update procedure is similar to the conventional ptychography iterative reconstruction described previously.

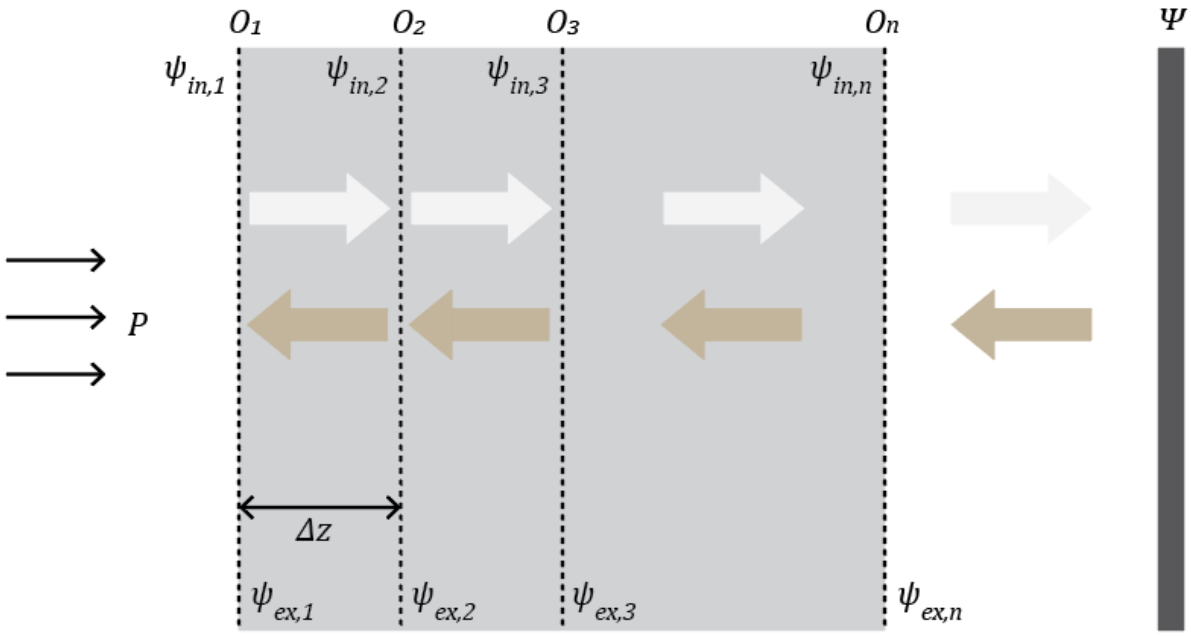

Figure 2.13: Schematic of multi-slice model for 3PIE algorithm. In the forward calculation, for each slice, the exit wave from the previous slice becomes the new incident wave front for the next slice.

1. Starting with a new diffraction pattern recorded at a random position j with a position offset of R_j. The exit wave from the first slice can be computed as

$$\psi_{ex,1}(r) = P\big(r - R_j\big)O_1(r) \tag{2.30}$$

2. This exit wave is propagated over distance Δz to the next slice and becomes the new subsequent incident wave $\Delta z_{n-1,n} = z_n - z_{n-1}$, where z_n denotes to the distance between the nth slice and the detector, and z_{n-1} denotes to the distance between the nth and $(n-1)$th slice correspondingly,

$$\psi_{in,2}(r) = D_{\Delta z_{1,2}}\{\psi_{ex,1}(r)\}. \tag{2.31}$$

3. This same propagation process repeats through all the subsequent slices until the exit wave of the final nth slice is computed as

$$\psi_{ex,n}(r) = D_{\Delta z_{n-1,n}}\{\psi_{in,n-1}(r)\}. \tag{2.32}$$

4. Then this exit wave at jth position is propagated to the detector plane with a propagator, D_Δ (either near-field or Fourier propagator) over distance Δ.

$$\Psi_j(u) = D_\Delta\{\psi_{ex,n}(r)\}. \tag{2.33}$$

5. Then the first constraint is applied, where the estimated modulus of the wavefront is corrected by the measured diffraction pattern $I(u)$

$$\Psi_j'(u) = \sqrt{I_j(u)}\frac{\Psi_j(u)}{\left|\Psi_j(u)\right|}. \tag{2.34}$$

6. This corrected wavefront then back-propagates to the object plane and a revised estimation of the original wavefront at n th slice

$$\psi_{ex,n}'(r) = D_{\Delta}^{-1}\{\Psi_j'(u)\}. \tag{2.35}$$

7. The newly revised approximation of incident probe and object at nth slice are updated using appreciated update function

$$\psi_{in,n}'(r) = U\left[\psi_{in,n}(r), O_n(r), \Delta\psi_n(r)\right], \tag{2.36}$$

$$O_n'(r) = U\left[O_n(r), \psi_{in,n}(r), \Delta\psi_n(r)\right], \tag{2.37}$$

With $\Delta\psi_n(r) = \psi_{ex,n}' - \psi_{ex,n}$.

8. This revised incident wave is then propagated back to $(n-1)$th slice and the exit wave of this slice can be computed

$$\psi_{ex,n-1}'(r) = D_{\Delta AS}^{-1}\{\psi_{in,n}'(r)\}. \tag{2.38}$$

9. The revised incident wavefront of n-1 slice now can be computed as

$$\psi_{in,n-1}'(r) = U\left[\psi_{in,n-1}(r), O_{n-1}(r), \Delta\psi_{ex,n-1}(r)\right], \tag{2.39}$$

$$O_{n-1}'(r) = U\left[O_{n-1}(r), \psi_{in,n-1}(r), \Delta\psi_{ex,n-1}(r)\right]. \tag{2.40}$$

10. Step 8 and 9 are then repeat until the incident wavefront (probe) and object slice corresponding to the 1st slice are updated

$$P'\left(r - R_j\right) = U\left[P\left(r - R_j\right), O_1(r), \Delta\psi_1(r)\right], \tag{2.41}$$

$$O_1'(r) = U\left[O_1(r), \psi_{in,1}(r), \Delta\psi_1(r)\right]. \tag{2.42}$$

All the object $O_n(r)$ is replaced with the updated O'_n and $P(r)$ is replaced with $P'(r)$.

All steps describe above are repeat for all the position recorded for one iteration of 3PIE algorithm.

Experimental configuration for far-field multi-slice ptychography

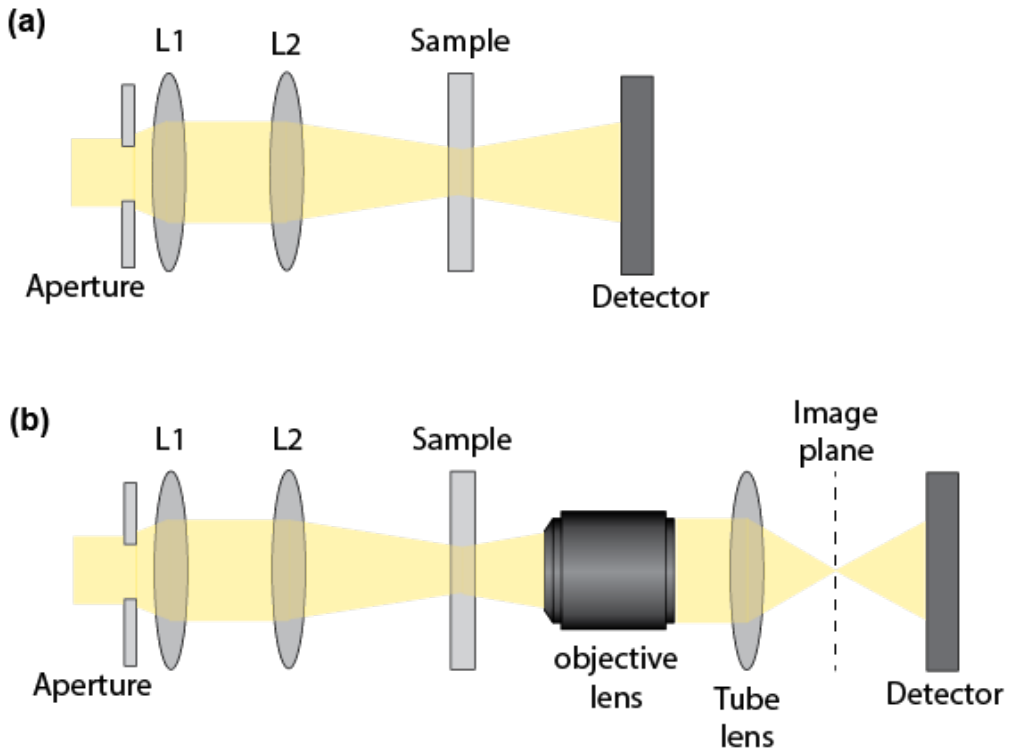

Figure 2.14 Experiment configuration for far-field multi-slice ptychography. (a) lensless configuration, (b) with added microscope system.

One advantage of multi-slice ptychography is the compatibility with any standard 2D ptychography imaging system [2], which can be implemented either in a lensless configuration [2] or with an additional microscope system [90], as discussed in Section 2.5. In this section, some optical far-field multi-slice ptychography configurations and results are reviewed.

a. Lensless configuration

The assembly of the imaging system is shown in **Figure 2.14(a)** was first demonstrated by A. Maiden [2]. The lensless conventional ptychography system is formed by a standard 4F configuration, where the optical system uses two doublet lenses L1 and L2 to perform Fourier transforms on the input image. A pinhole with diameter of 100 µm is placed at the upper focal point of L1 (f = 30 mm), while the sample is mounted at the down-beam focal point of L2 (10× objective). The 4F system projects the demagnified pinhole image (~60 µm)

onto the sample, forming the far-field diffraction patterns for ptychographic reconstruction, where a CCD camera is mounted 32 mm downstream to the sample. Each ptychographic data set is consisted of 400 diffraction patterns (128×128 pixels) with step size of 6 µm. The resulting pixel pitch of the configuration is approximately 1.4 µm. The corresponding best reconstruction result from this configuration consists of the 3 slices slice separated by 11 µm [2].

b. Additional microscope system

The resolution for optical far-field ptychography is primarily determined by the diameter of the aperture and the detector pixel size. In order to improve the resolution limit, Godden later added a microscope system to the optical multi-slice ptychography configuration, where a virtual detector with a demagnified pixel pitch size was formed for the collection of diffraction pattern data [90]. The schematic of the imaging system is shown in **Figure 2.14(b)** [90]. A 400 µm pinhole at the upper focal plane of L1 (f = 30 mm) was projected onto the sample, positioned at down-beam focal point of L2 (f = 3.1 mm) via a 4F system. This results in a demagnified diameter of approximately 75 µm. 400 far-field diffraction patterns (1024×1024 pixels) with step size of 5 µm were then collected via the virtual detector with magnification of 21× magnification, which is positioned 65 µm downstream from the sample. The resulted pixel pitch size of the configuration is 280 nm. The best reconstruction result from this configuration is consisted of a total number of 33 slices with separation distance of 4.7 µm [90]. A further experiment using 40× magnification virtual detector was reported to achieve 34 slices with 2 µm axial step.

Both high lateral and depth resolution can be achieved by far-field multi-slice ptychography in comparison to other optical imaging techniques, however, at least 400 far-field diffraction patterns were required to maintain a reasonable reconstruction FoV, due to the small illumination size, which is constrained by the small pinhole size. Therefore, in order to image a relatively large sample volume, the data size can be excessively large, which requires high computational power.

2.9.2.3. Fourier multi-slice ptychography (FMP)

Multi-slice model has also been implemented with Fourier ptychography. With the main benefit of the ability to achieve both lateral and depth resolution beyond diffraction limit of the microscope, and the large FoV is inherited from using a low NA objective lens [3].

Forward model:

Starting with one random initial probe illumination $P_n^j(r)$ angled from the jth LED, the wavefront exiting $\psi_{ex,n}^j$ the nth slice can be expressed by the following multi-propagation process, where the next incident field is $P_{n+1}^j(r)$:

$$\psi_{ex,n}^j(r) = O_n(r)P_n^j(r) \tag{2.43}$$

$$P_{n+1}^j(r) = D_{\Delta z_{n,n+1}}\{\psi_{ex,n}(r)\}. \tag{2.44}$$

Following by the steps described above, the complex transfer function of the Fourier spectrum $C^j(u)$ at the aperture plane can be denoted as the product of the spectrum of the exit wave $\Psi_{sp}(u)$ from the final nth slice and the pupil function $Pupil(u)$ of the aperture. The spatial frequency here is determined by the illumination angle θ, where $u = \left(\frac{sin\theta_{x,j}}{\lambda}, \frac{sin\theta_{y,j}}{\lambda}\right)$.

$$C^j(u) = \Psi_{sp}^{\mathrm{j}}(u)Pupil(u), \tag{2.45}$$

where the spectrum of the exit wave from the sample is

$$\Psi_{sp}^{\mathrm{j}}(u) = \mathcal{F}\{\psi_{ex,n}^j(r)\}, \tag{2.46}$$

The intensity measurement recorded at jth LED illumination is

$$I^j(r) = \left|\mathcal{F}\{C^j(u)\}\right|^2. \tag{2.47}$$

Backward model:

Similar to the conventional ptychography, the new estimate of the Fourier spectrum at detector plane is updated using the measured intensity:

$$C'^{j}(u) = \mathcal{F}^{-1}\left\{\sqrt{I_n}\frac{\mathcal{F}\{C^j\}}{|\mathcal{F}\{C^j\}|}\right\}. \quad (2.48)$$

The revised estimation of the exit wave spectrum and pupil function of the aperture using update functions:

$$\Psi'^{j}_{sp}(u) = U\left[\Psi_{sp,n}, Pupil, \Delta C^j\right], \quad (2.49)$$

$$P'^{j}_{n}(u) = U\left[Pulpil, \Psi_{\mathrm{sp}}, \Delta C^j\right]. \quad (2.50)$$

where $\Delta C^j(u) = C'^j - C^j$.

The corresponding real-space exit wave at nth slice can be computed using inverse Fourier transform,

$$\psi'_{ex,n}(r) = \mathcal{F}^{-1}\{\Psi'_{sp}(u)\}. \quad (2.51)$$

The transmissive function of the object $O^j_n(r)$ and the incident wavefront $P^j_n(u)$ at nth slice are then updated by the same process

$$O'^{j}_{n}(r) = U\left[O^j_n(r), P^j(r), \Delta\psi_{ex,n}\right], \quad (2.52)$$

$$P'^{j}_{n}(u) = U\left[P^j_n(r), O^j_n(r), \Delta\psi_{ex,n}\right], \quad (2.53)$$

where $\Delta\psi_{ex,n} = \psi'_{ex,n} - \psi_{ex,n}$.

Then the exit wavefront is updated by back-propagate $P'^{j}_{n}(u)$ from the last slice,

$$\psi'_{ex,n-1}(r) = D_{-\Delta z_{n-1,n}}\{P'^{j}_{n}(u)\}. \quad (2.54)$$

The process will repeat through the entire sample volume until the first slice is reached, where the probe illumination is the initial incident wavefront,

$$P'^{j}_{1}(u) = P^j_1(u).$$

One iteration includes repeats all procedure above for all illumination angles from each LEDs.

2.9.2.4. *Multi-layer Born model*

The Multi-layer Born (MLB) approximation is an alternative to conventional multi-slice model demonstrated by M. Chen to address the high-angle illumination by incorporating non-paraxial scattering in the model, where the 3D potential field for each individual slice is considered (shown in **Figure 2.15**) [94].

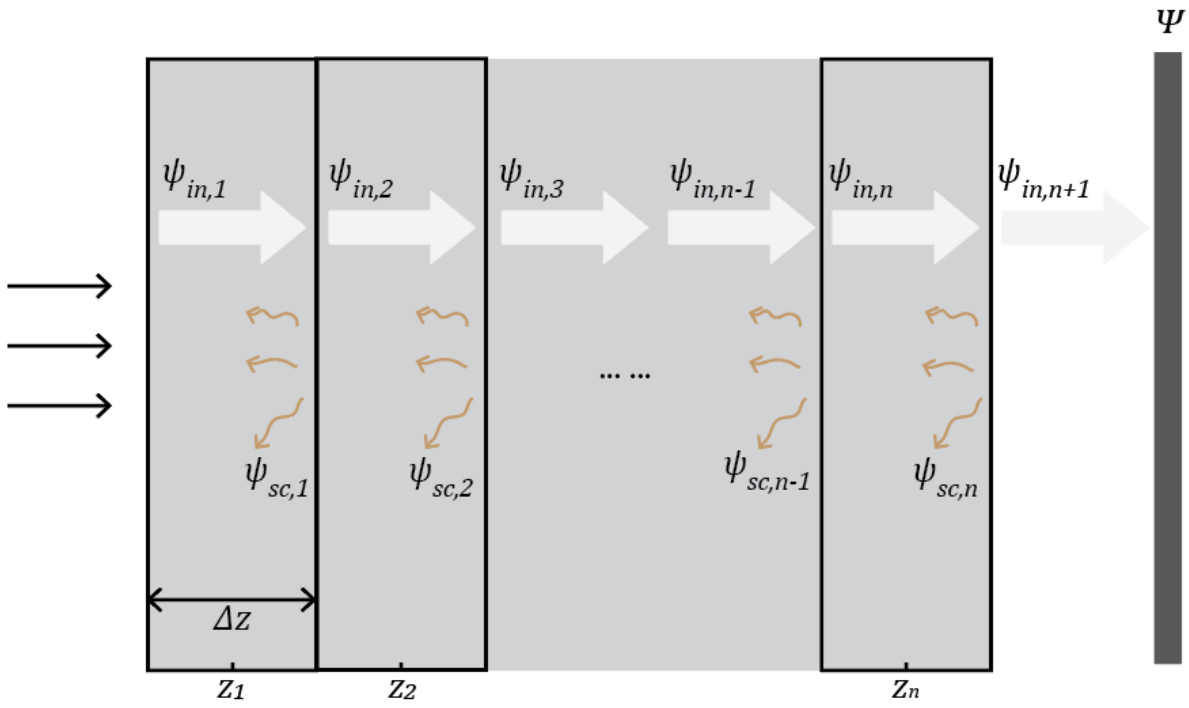

Figure 2.15: Forward scattering model for multi-layer Born. ψ_{in} is the incident field and ψ_{sc} is the 3D scatter field. Each layer has a finite thickness of Δz, the physical position of each layer z occupies $\left(n-\frac{1}{2}\right)\Delta z \; to \; \left(n+\frac{1}{2}\right)\Delta z$.

According to the first Born approximation, the new wave field scattered by a weakly scattered 2D object can be represented as

$$\psi_{new}(r,z) \approx \psi_{in}(r,z) + \iint G(r-r', z-z') \times \psi_{in}(r',z')V(r',z')dr'dz'. \qquad (2.55)$$

Where, r is the (x,y) coordinate, G is the scattering potential derived from Green's function, V is the 3D scattering field for an optically thick object.

Similarly to the conventional multi-slice approach, Multi-Layer Born model can be decomposed into multiple first Born approximation for each layer with a finite thickness of Δz. Assuming the incident wave at the first slice $\psi_{in,1}(r)$ is from the initial probe illumination. The incident wavefront for $(n+1)$th layer can be expressed as the recursive forward formular of MLB model for an object consisted of n slices in Eq. 2.56:

$$\psi_{in,n+1}(r,(n+1)\Delta z) = \psi_{in,n}(r,(n+1)\Delta z) + \psi_{sc,n}(r,(n+1)\Delta z). \quad (2.56)$$

The first term of Eq. 2.56 can be treated as free-space propagation of the incident wave

$$\psi_{in,n+1}(r,(n+1)\Delta z) = D_{AS_{\Delta z}}\{\psi_{in,n}(r,(n+1)\Delta z)\}. \quad (2.57)$$

The second term of Eq. 2.56 models the 3D scattering field:

$$\psi_{sc,n+1}(r,(n+1)\Delta z) = \mathcal{F}^{-1}\left\{\tilde{G}(u,\Delta z)\mathcal{F}\{\psi_{in,n}(r,(n+1)\Delta z)V_n(r)\}\right\}. \quad (2.58)$$

It is assumed that the scattering of the potential field $V_n(u)$ over a small thickness remain unchanged for each slice. $\tilde{G}$ denotes to the Fourier spectrum of Green's function.

Where D_Δ is angular spectrum propagation with the distance from $(n-1)$ to nth slice.

Then the standard Fourier ptychography model is followed, where the spectrum of the wavefield exiting the nth slice at detector plane is

$$\psi_{image}(r) = \mathcal{F}^{-1}\left\{C(u,\Delta z_f)\mathcal{F}\{\psi_{in,n+1}(r,(n+1)\Delta z)\}\right\}. \quad (2.59)$$

C is the refocusing operator, which compensates for the defocus distance by applying a correction function in the frequency domain. This function C adjusts for the defocus effect over the propagation distance Δz_f, which is essentially a free-space propagation step over distance Δz_f.

The detailed backward model and the implementation of the reconstruction algorithm can be referred to the original work [94].

Near-field Multi-slice Ptychography

The next part of the thesis is divided into three result chapters, which present the modification of the 3PIE algorithm and the corresponding experimental results for Near-field Multi-slice Ptychography (NMP) in the cone-beam geometry for visible light and X-rays, and a further NMP microscope implementation with an optical configuration.

Chapter 3 begins with an introduction to the DoF limit in ptychography and the adaptation of the multi-slice model for cone-beam near-field ptychography. The modifications of the 3PIE algorithm to accommodate the alternative equivalent geometry, as discussed in section 2, are then addressed for samples exceeding the DoF limit. This is followed by a detailed introduction to the proof-of-principle lensless optical NMP experiment. Subsequently, the chapter presents the multi-slice ptychographic reconstruction results using the modified 3PIE algorithm, starting with a double-layered laser-cut testing sample to optimise the initial experiment configuration, and progressing to an optically thick bee's leg sample. A comprehensive comparison between 2D reconstruction and the survey on the minimum diffraction pattern number requirement is then presented in the results section.

Following the optical NMP result, Chapter 4 starts with an overview of the coherent branchline I13-1 at the Diamond Light Source, followed by two X-ray NMP experiment sections with two different configurations. In the first experiment section, the experimental setup and data acquisition process are described. The experiment is then performed with a Siemens star testing sample and a series of layered and continuous thick samples. The resolution and DoF achieved is then evaluated and discussed. In the second experiment, the limitation faced in the initial experiment were evaluated and improved. Finally, reconstruction results consisting of an initial reconstruction of a Siemens star and a continuous thick sample are presented.

The final result chapter, Chapter 5, NMP is combined with additional microscope system with objective lens magnification of 20× and NA = 0.5, called Near-field Multi-slice Ptychography Microscopy (NMPM). This chapter starts with a detailed introduction to the experimental configuration and a comprehensive survey on the influence of illumination frequency spectrum and step size on the multi-slice reconstruction effectiveness.

Furthermore, the optimised imaging system is then tested on three sets of biological samples and the minimal requirement of diffraction pattern number is investigated. In the end, a further experimental implementation with higher NA objective lens (40×; NA = 0.75) is presented.

3. Lensless optical cone-beam Near-field Multi-slice Ptychography (NMP)

Ptychography's headline advantage is the ultra-high resolutions it can achieve, reaching deep sub-ängstrom levels in the electron microscope [72] and, in combination with x-ray tomography [14], hitting isotropic 3D image resolution below 20 nm [95]. These remarkable resolutions are, however, limited to small, optically thin samples. Similarly to traditional forms of microscopy, ptychography also requires that the entire sample thickness lies within the DoF of the imaging system. Thicker samples cause ptychographic algorithms either to fail completely or to heavily distort the reconstructed image.

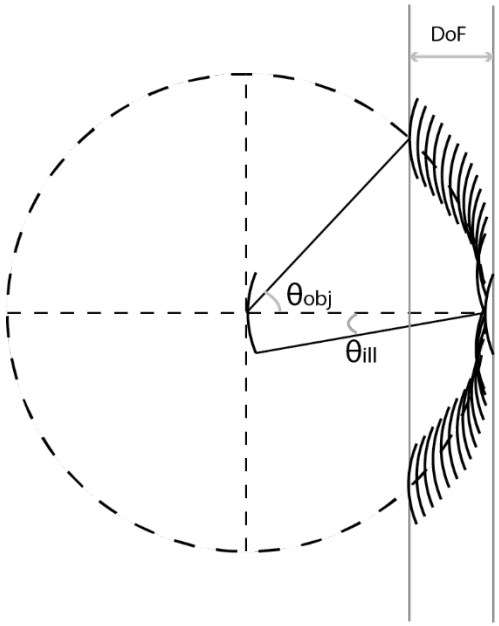

Figure 3.1. Representation of the Ewald sphere for a sufficiently thin object. Θ_{obj} is the half angle of the object scattering angle and Θ_{ill} is the half angle of the illumination angle.

One way to define the DoF or the maximum sample thickness is to consider the Ewald sphere of an image system under Born approximation, as shown in **Figure 3.1** [3] [96]. The sample is required to be sufficiently thin, so that the exit wave can be approximated by the multiplication of the illumination and the transmissive function of the sample. A generalised

numerical representation of DoF in relation to the numerical aperture of both the illumination and the object, was derived by L. Tian as shown in Eq. 3.1 [3].

$$DoF = \frac{\lambda}{2 - \sqrt{1 - NA_{illu}^2} - \sqrt{1 - NA_{obj}^2}}. \quad (3.1)$$

Where NA_{illu} is the numerical aperture of the illumination and NA_{obj} is the numerical aperture of the object.

Several researchers have then later refined this equation in relation to the image resolution, determined by the NA of the image system, to which can be reliably applied for conventional ptychography, both theoretically and experimentally. The general relationship they agree on is given by Eq. 3.2:

$$T_{min} = DoF \leq \frac{c{\delta_r}^2}{\lambda}. \quad (3.2)$$

Here T_{min} is the minimal slice separation distance, δ_r represents the image resolution, λ is the beam wavelength and c is a constant, variously reported to have a value from 1 [97] up to 5.4 [98]. The constant c varies depending on the overall system NA of the imaging system, as well as other factors like the sample being imaged. This constant adjusts the equation to account for variations in these factors. Regardless of this scale factor, the thickness limit of Eq. 3.2 becomes increasingly severe as the target resolution drops. In X-ray ptychography, for example, even at hard X-ray energies DoF falls into the 100's of micron range as the lateral resolution goes beneath 100 nm. This trade-off between thickness and resolution poses a particular problem for ptycho-tomography applications aiming to obtain statistically significant amount of data from meaningful sample volumes, for example mapping connections in brain tissue, where neurons only a few tens of nanometres in diameter can extend over hundreds of microns [99] [100].

One way to overcome sample thickness constraints in ptychography is to incorporate a multi-slice model into the reconstruction algorithm [2] [92]. Multi-slice ptychographic algorithms pass estimates of the illumination wavefront and the contents of each slice through this forward model, revise the resulting estimate of the wavefront incident on the

detector to agree with the measured data, then reverse the multi-slice process as shown in **Figure 3.2(b)** – back-propagating to each slice in turn and updating the wavefronts and slice contents along the way, via update equations identical to those used in conventional ptychography [51] [67]. For samples whose thickness exceeds that dictated by Eq. 3.2, the multi-slice model is considerably more accurate than the standard multiplicative approximation used by 2D ptychography, which can be thought of as the reductive case of a multi-slice model with only a single slice. Incorporating this more accurate model within ptychographic algorithms has extended DoF by an order of magnitude, with visible light, X-rays and in the electron microscope [1] [4] [90] [101].

As discussed earlier in this chapter, the multi-slice method had been applied only in the far-field diffraction regime. As mentioned previously, one of the aims of this thesis is to increase both sample thickness and lateral volume imaging capabilities. To achieve this, implementation of the multi-slice method in the near-field regime becomes a natural choice. Unlike far-field ptychography, where a small, localised patch of illumination is used to 'probe' the sample, near-field ptychography utilises a beam modulator, or diffuser, to generate a speckle-like pattern that flood-illuminates the sample [20]. Whilst operating in this near-field regime does not offer the extremely high resolution of the far-field method, it does provide two benefits. First, a large FoV can be captured from data comprising only twenty or so diffraction patterns, compared to many hundreds or thousands for far-field ptychography. This can be especially advantageous for ptycho-tomography, where data collection in the far-field can take many hours. Secondly, the dynamic range requirement of the detector can be reduced because there is no huge central diffraction peak in the data.

In this chapter, an adaptation of the original multi-slice ptychographic algorithm, 3PIE, outlined in Section 2.9.2, is introduced for the implementation of cone-beam, near-field ptychography. Then the experiment configuration for optical NMP is demonstrated via a designated 2-layered sample and a continuous biological sample - a bee's leg. In the end of the chapter, the minimum requirement for optical NMP is evaluated.

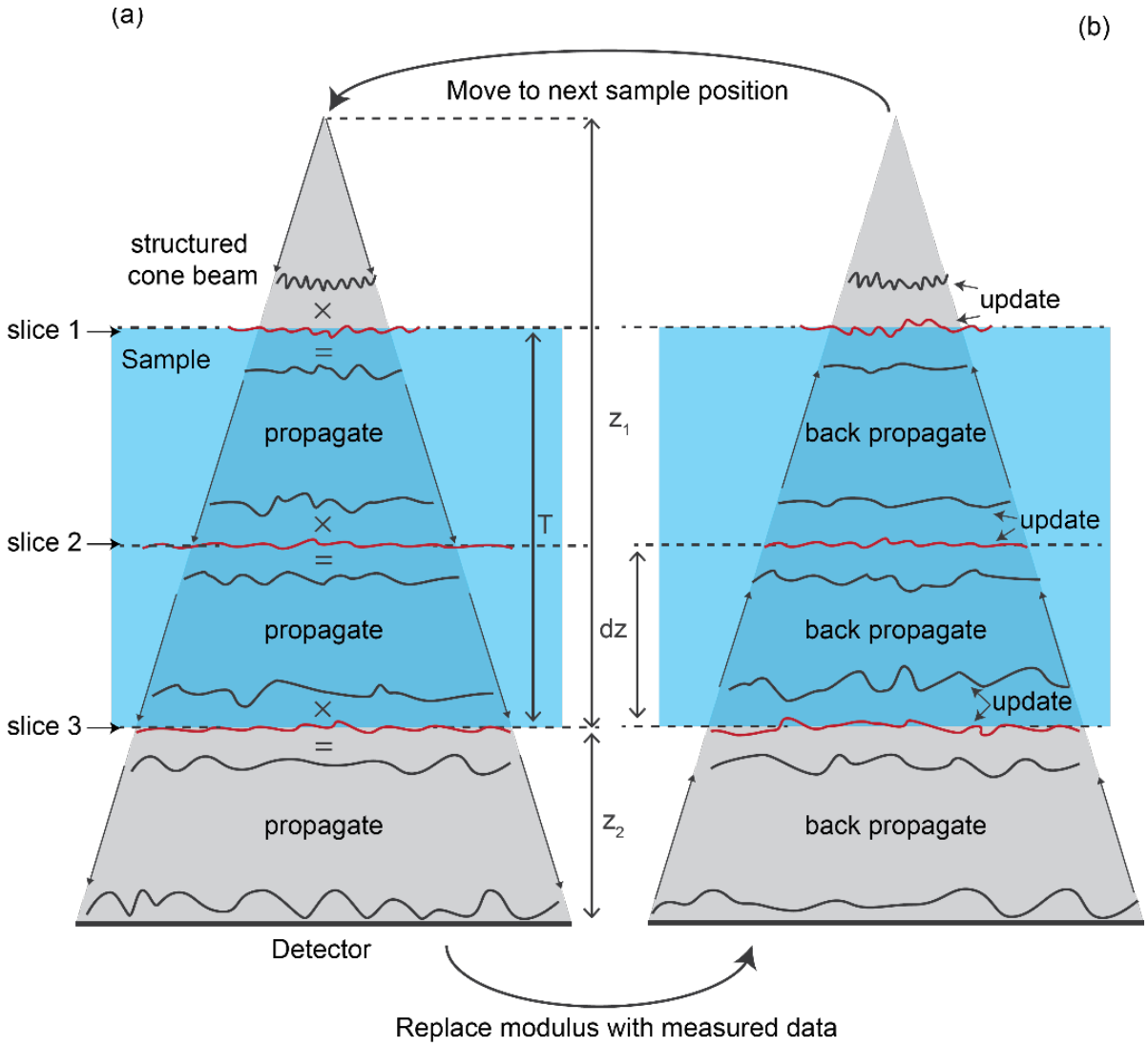

Figure 3.2. A schematic illustration of the multi-slice reconstruction process. A sample of thickness T is modelled by thin slices, each of which represents part of the sample volume – the multi-slice algorithm solves for these slices, as well as the illuminating cone beam wavefront. (a) The algorithm first approximates the wavefront incident upon the detector via a chain of multiply-propagate steps through the slices, using current estimates of the illumination wavefront and the slice contents. (b) This wavefront is modified to match the recorded diffraction data and the result then back-propagated through the slices one by one, updating the slice contents and the illumination wavefront at each step.

3.1. Geometric modification

To adapt multi-slice ptychography for the cone beam geometry the FST (see Section 1.3.2.4) must be used to propagate not only from the sample to the detector, as in the 2D case discussed in Section 2.8.3, but also between the slices in the multi-slice model. This additional deployment of the FST is complicated by the changing geometric magnification within the sample thickness: the magnification is higher for the up-beam face of the sample, closest to the cone beam focus, decreases within the sample volume, and reaches a minimum at the down-beam face, closest to the detector. Application of the FST must therefore use a slightly larger magnification at the first slice than at the second slice, and so forth. It is possible to do this through an extension of **Figure 2.11(b)** to the multi-slice case [85], but this involves re-interpolating the wavefronts at each slice of the object to accommodate the changing magnifications. Instead, a simpler approach extends **Figure 2.11(c)** to implement the multi-magnification FST, through the equivalence of the two geometries shown in **Figure 3.3**.

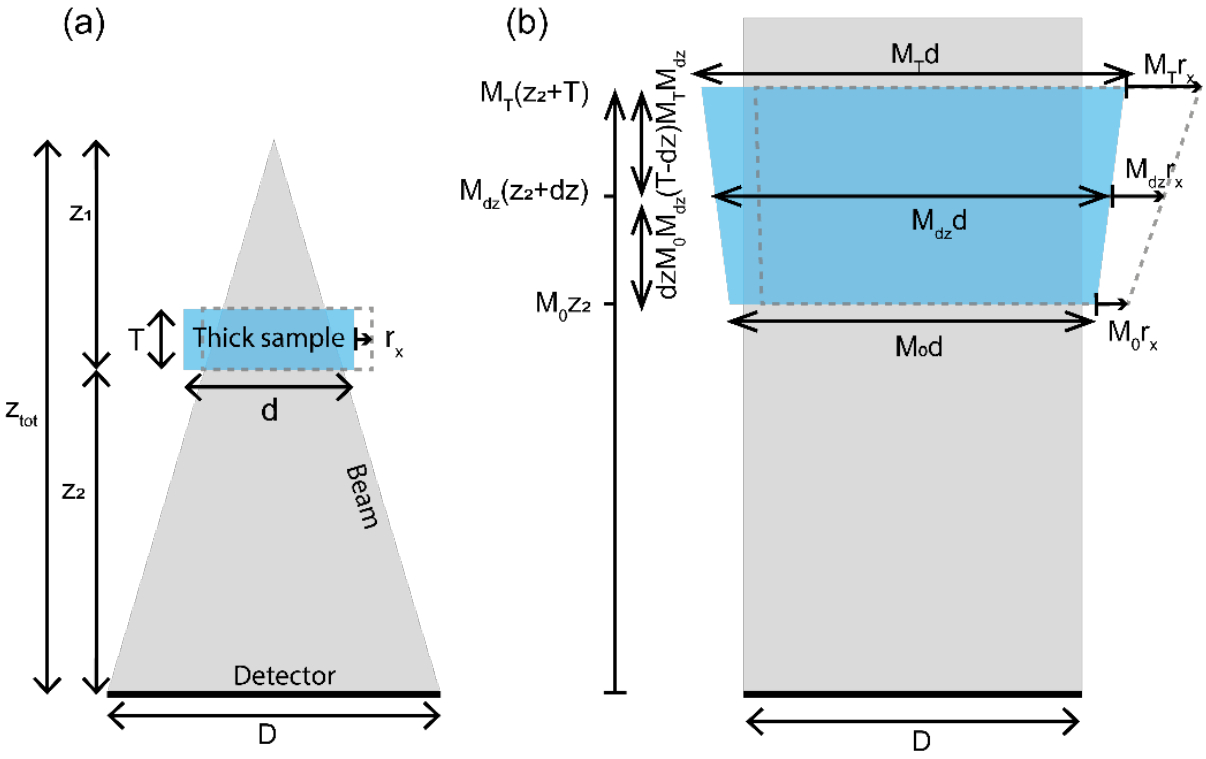

Figure 3.3. An equivalent plane-illumination model for an optically thick sample. (a) Experimental configuration of cone-beam near-field ptychography. (b) Equivalent plane-illumination.

Figure 3.3(a) shows the experimental setup for cone-beam near-field ptychography, the sample thickness is T, the detector is of diameter D, d is a representative distance on the down-beam face of the sample, r_x is an example sample translation between positions in the ptychographic scan, which moves the sample to the location shown by the dotted line. z_1 is the distance from the cone beam focus to the down-beam face of the sample and z_2 is the distance from the down-beam face to the detector. **Figure 3.3(b)** shows an equivalent three-slice model of the actual experimental geometry in **Figure 3.3(a)** incorporating the change in magnification within the sample volume, where the slices are located at the down-beam face of the sample, a distance z_2 from the detector; an arbitrary distance dz up-beam from this; and at the up-beam face of the sample, a distance $z_2 + T$ from the detector and a distance $z_1 - T$ from the cone apex. The distance from the detector to the down-beam sample face is multiplied by the base geometric magnification M_o . The sample itself is imagined to be stretched both laterally and axially as shown, reflecting the magnification changes within the sample volume. The model incorporates parallax by scaling the ptychographic scan translations by the magnification at different planes, as shown by the translation vectors to the right and the dotted outline.

The magnification at the down-beam face is M_0 as it was for the 2D case. The magnification of the slice located dz meters up-beam of this face is given by Eq. 3.3:

$$M_{dz} = \frac{z_1 + z_2}{z_1 - dz} = \frac{z_{tot}}{\frac{z_{tot}}{M_0} - dz}, \tag{3.3}$$

with the magnification at the down-beam slice found by substituting $dz = T$.

Referring to the diagrams shown in **Figure 3.3(a)**, the magnification factor of the most down-beam slice M_0 and the most up-beam slice M_T are:

$$M_T = M_{dz} = \frac{z_1 + z_2}{z_1 - T},\ M_0 = \frac{z_1 + z_2}{z_1}. \tag{3.4}$$

Consequently, the distance between the slices in **Figure 3.3(b)** located at $M_T(z_2 + T)$ and $M_0 z_2$ can be derived:

$$M_T(z_2 + T) - M_0 z_2$$

$$= M_0\left(\frac{z_1(z_2+T)}{z_1-T} - z_2\right)$$
$$= \frac{M_0}{z_1-T}\big(z_1(z_2+T) - z_2(z_1-T)\big)$$
$$= M_0 T\frac{(z_1+z_2)}{z_1-T}$$
$$= M_0 T M_T. \qquad (3.5)$$

Within the sample, the z-axis of the model in **Figure 3.3(b)** is stretched non-linearly, such that the physical distance between two adjacent slices in the multi-slice model increases by the product of the magnifications of each slice. For example, illustrated in the Figure are two slices located $z_2 + dz$ and $z_2 + T$ up-beam of the detector. The physical distance between these slices is $T - dz$ and the magnifications of the slices are calculated from Eq. 3.4 as M_{dz} and M_T: the model therefore implements the FST by stretching the intervening distance to $(T - dz)M_T M_{dz}$. This model is consistent with the usual 2D near-field model shown in **Figure 2.13**, in that any one of the slices in the model can be chosen and the rest of the slices "deactivated" (maintained as free-space or matrices of ones in the algorithm) and the result is the same as for one of the 2D algorithms, albeit with the propagation to the detector broken into several sub-propagations.

Similar adjustments to those used to convert conventional 2D ptychographic algorithms for cone-beam near-field data also apply to the multi-slice case. The adjustment steps for the equivalence 3D case shown in **Figure 3.3**, now are as follows:

1. As with the 2D modifications, use the angular spectrum propagator to propagate from the down-beam face of the sample to the detector,
2. Increase the propagation distance used in that propagator from z_2 to $z_2 M_0$,
3. Multiply the propagation distances between adjacent slices in the multi-slice model by the product of the magnifications at each slice,
4. Set different magnifications for each slice of the multi-slice model by converting the measured sample positions, $r_{x,y}$, to pixel offsets, $r_{k,m,n}$, that are different for each of the $k = 1 \ldots K$ slices. These offsets are calculated according to Eq. 3.6:

$$r_{k,m,n} = \frac{M_k}{dc} r_{x,y}, \qquad (3.6)$$

where M_k is the magnification at the plane of the kth slice, given by substituting the corresponding slice position, dz, into Eq. 3.3. Again, step 1 requires minor modification of the code, but steps 2-4 are preprocessing steps and only require changes to the input parameters to the 3PIE algorithm; once these pre-processing steps are carried out, the algorithm proceeds exactly as outlined in **Figure 3.2** and as detailed in the Section 2.9.2 [2]. Alternative multi-slice ptychographic reconstruction algorithms can also be modified in the same way to accommodate the cone beam geometry [92].

The reconstruction **Code 1** and example **Dataset 1** is avaiblable in **Appendix I**.

3.2. Evaluation of aliasing condition

In Section 1.4.3, the sampling condition for the discrete near-field propagator was evaluated, leading to Eq. 3.7:

$$N < \frac{\lambda z}{dx^2}, \tag{3.7}$$

or

$$dx < \frac{\lambda z}{L}, \tag{3.8}$$

where, N is the size of the sampling matrix in pixels, λ is the wavelength of the radiation source, z is the propagation distance and dx is the real-space sampling pixel size. L is the field of view or camera dimension, which consists of N pixels, $L = N\ dx$. If the above conditions are violated, periodical copies of the spherical phase chirps will occur causing aliasing. Therefore, it is very important to consider this condition while designing experiment configurations for the near-field regime.

The above equations can be further derived from the Nyquist limit on the quadratic phase to model the cone-beam near-field propagator configuration. The maximum magnification that can be achieved without the occurrence of aliasing in the model is given by Eq. 3.9.

$$M_0 < \frac{N dx^2}{\lambda z_{tot}} + 1. \tag{3.9}$$

3.3. Experimental configuration

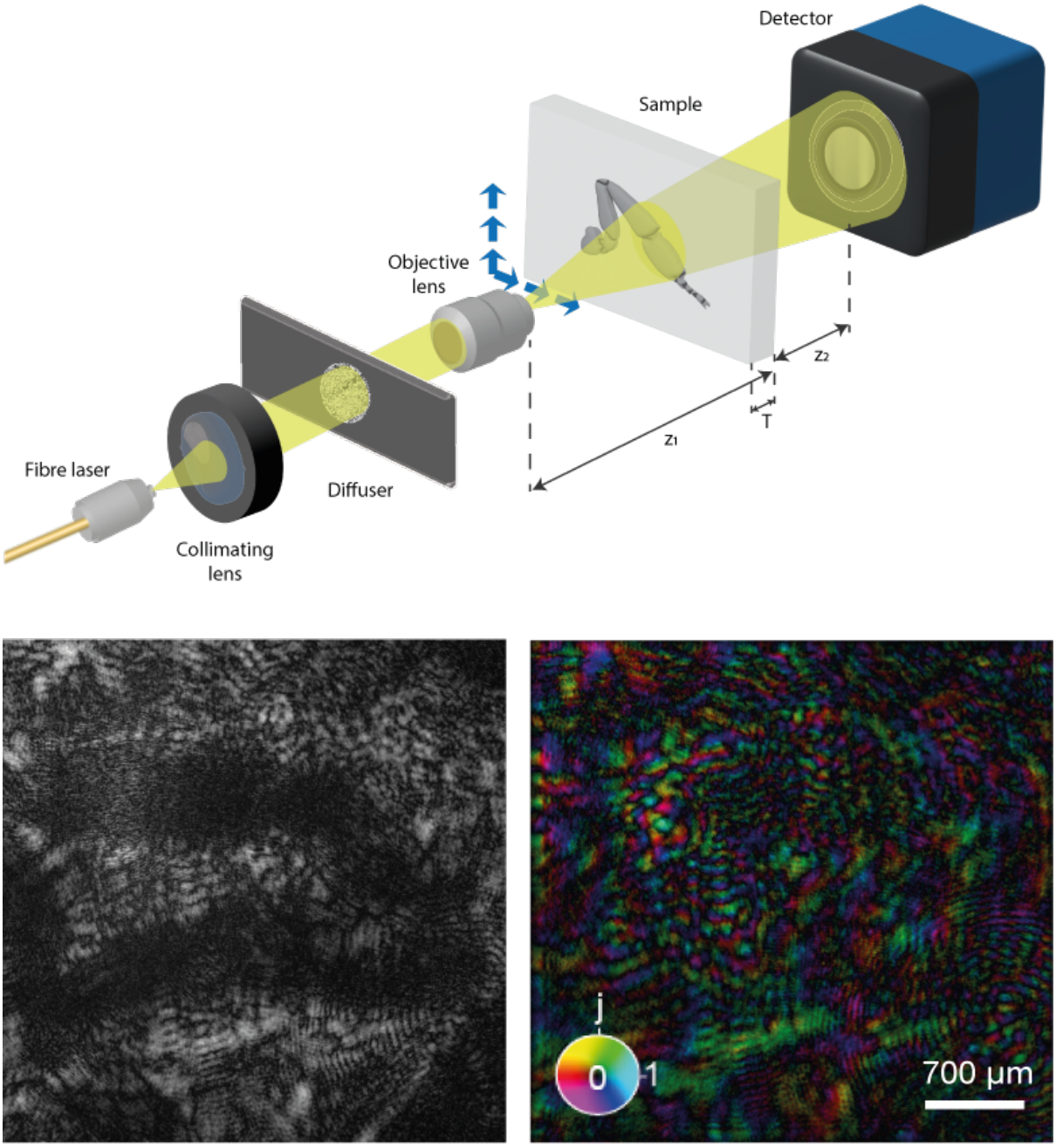

Figure 3.4. Top: Near -field multi-slice ptychography configuration on optical bench, Bottom left: an example diffraction pattern collected in the experiment. Bottom right: reconstructed probe.

Experiments in the visible light regime were conducted on the optical bench setup with the assembly shown in **Figure 3.4**. The system comprised a fibre-coupled laser with wavelength

of 675 nm (THORLABS S1FC675 5mW), a collimating lens and a microscope objective (40×, 0.75NA, Olympus); a scotch tape diffuser; a 3-axis linear translation motorised stage from Newport (M-VP-25XL-XYZR); and an sCMOS camera with dynamic range of 16-bit and 2048×2048 pixels on a 6.5 µm pitch (PCO edge 4.2). The full system was constructed on top of a Newport optical table for damping absorption and dissipation of any excessive environmental vibration. The beam from the fibre laser passes through a collimating lens, then a diffuser before hitting the inverted objective lens. The objective focuses the beam to a point, and from there the structured wavefront expands as it propagates a distance z_1 to arrive at the sample of thickness T, which is mounted on a motorised translation stage. After passing through the sample the wavefront then propagates a distance z_2 to the detector. In **Figure 3.4**, an example of a 2048×2048 pixels diffraction pattern collected from the setup is shown bottom left, and the structured illumination wavefront, recovered during the reconstruction process, is shown bottom right. 4× 0.5s camera exposures were averaged in the recording of each pattern and a dark frame recording was subtracted from the data, with any negative-valued pixels set to zero. The sample was translated through the structured beam in a Fermat Spiral scan pattern [32] with a step size of 130 µm, equating to an overlap between scan positions of 95%. The instrumental control and data acquisition were realised via an interface system on MATLAB. An example of the MATLAB control GUI window for the optical bench experiment is shown in **Figure 3.5.** The GUI is dived into three main parts – Data collection, stage controls and displays. Most of the data collection parameters were explained in Section 2.8.2. The "Stage Controls" initialises the sample position, with x and y representing the lateral position and z representing the beam direction. Those inputs also determine the setting of camera length and the degree of (de-)focus of the sample. The detector view is displayed in the "Live View" window. The "Histogram" shows the average intensity of the detector view, and "Cross Section" shows the intensity of the pixels corresponding to the green dotted line in the "Live View". "Mag. Calculation" is used to calculate the magnification, focus-to-camera distance and camera length automatically via a cross-correlation algorithm. The value of the lateral step X_c is typically set to around 10% of

the detector's dimension, and the value of z-step X_{cz} is set to value equal to "defocus" distance.

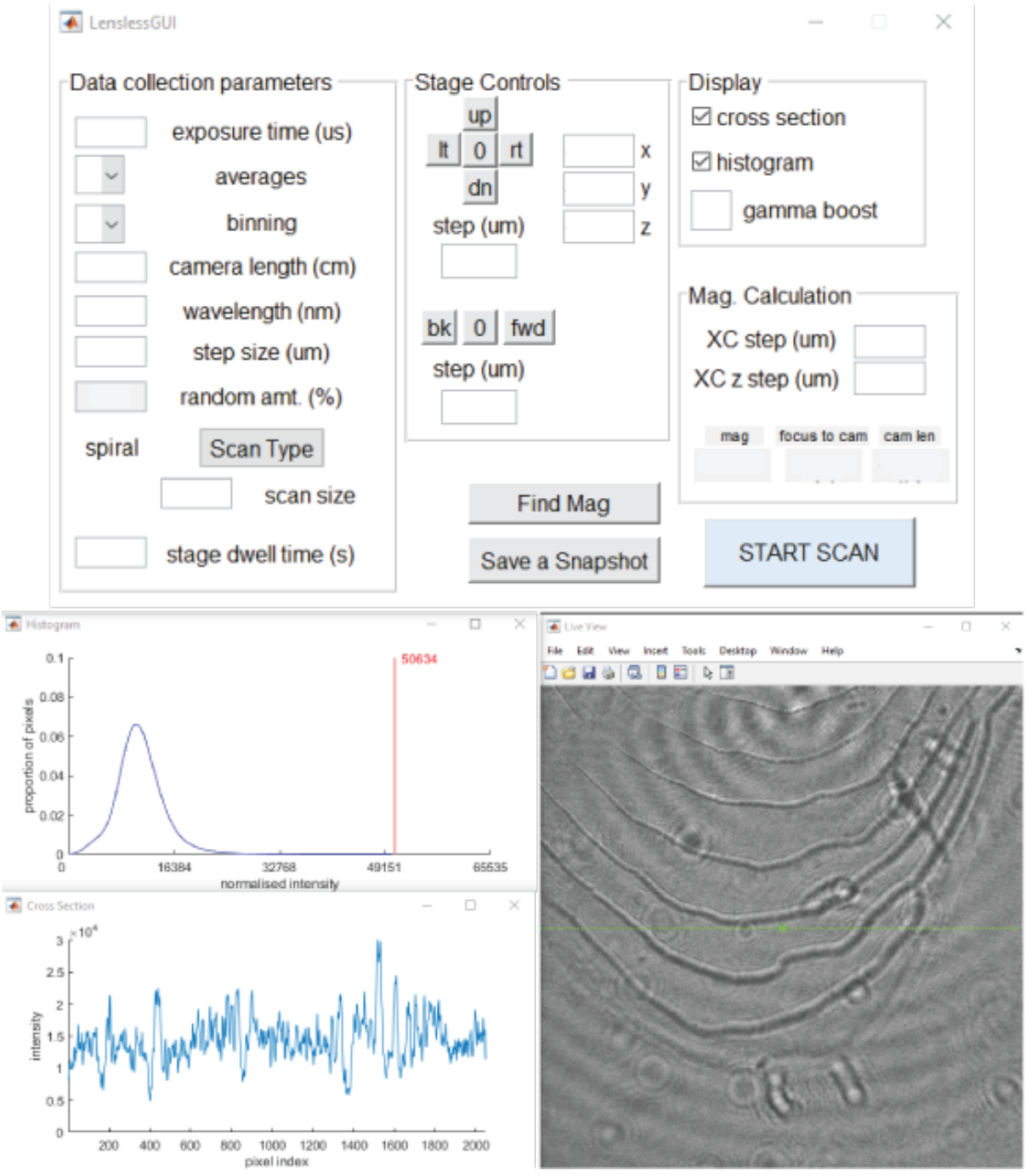

Figure 3.5. Optical bench control GUI via MATLAB platform

The general data collection procedure for the optical NMP experiment follows the steps below:

1. The diffuser was removed from the beam path.
2. The sample was placed onto the motored stage, and the region of interested aligned to the centre of the detector view.
3. The exact magnification and the camera length (distance from sample to detector) were calculated.
4. The diffuser was placed back to the original position.
5. The exposure time and laser intensity were adjusted so that the average intensity was around 40000 – 50000 (the camera saturated at a value of 2^{16}).
6. The scan pattern and total number of diffraction patterns were chosen, and the step size was set to an equivalence approximately 80-90% overlap.
7. Diffraction patterns were then collected via ptychography scan with a dark frame recorded in the beginning.

3.3.1. Experimental results

3.3.1.1. Initial testing - double layered laser cut sample.

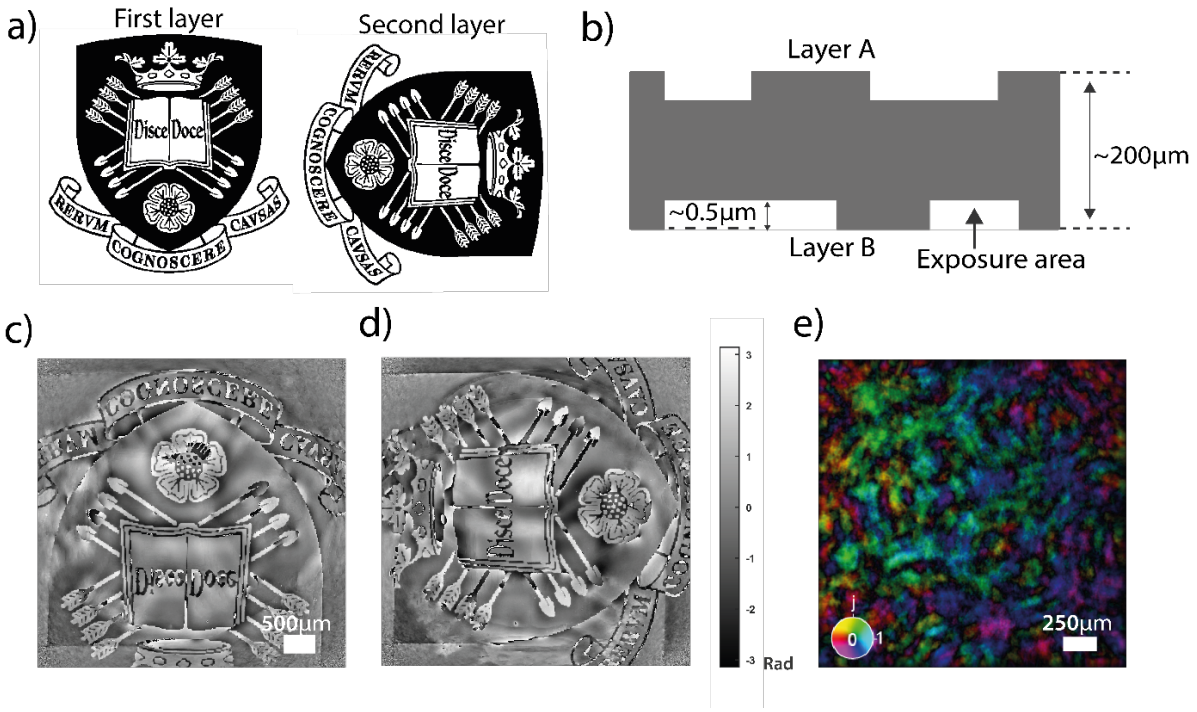

Figure 3.6. (a) shows the layout of the double-layered sample with 90-degree rotational shift between the two layers, (b) shows the arrangement of the design layout of the double-layered sample. (c) and (d) are phase reconstruction of the two layered sample with 200 µm separation distance, (e) is the recovered probe.

To test the initial experimental configuration, a 2-layer laser-cut testing sample (as shown in **Figure 3.6(a-b)**) with 200 µm gap were designed to assess the effect of illumination angle and separation effectiveness across a range of magnification.

For the experiment corresponding to the reconstruction result shown in **Figure 3.6(c-d),** the focal-to-detector distance (z_{tot}) was initially set to approximately 4 cm and the sample to detector distance was set to 3.3 cm, which gave a resultant geometrical magnification of 5.82×. The ptychographic dataset consisted of 400 diffraction patterns with 95% overlap between each scan point. All the diffraction patterns were binned by a factor of 2 to 1024×1024 pixels to avoid aliasing, which gives an effective pixel size of 2.34 µm.

The geometrical magnification can be changed simply by adjusting the ratio of the focal-to-sample distance (z_1) and sample-to-detector distance (z_2). Further tests of 2-layer multi-slice reconstruction results for the layered logo sample shown **Figure 3.7(a-c)** were collected using 40× illumination objective lens, yielding the measured magnifications of 5.9×, 3.7× and 14.86×. The results shown in **Figure 3.7(d)** were obtained with a smaller illumination angle formed with a 20× objective lens with magnification of 5.9×. A list of experimental and reconstruction parameter is summarised in **Table 3**.

Due to the large illumination area in near-field ptychography and the use of small step (95% overlap between scan) the effective field of view (FoV) is essentially determined by the illumination size. Although the central region may receive higher total fluence when a large number of diffraction patterns are acquired, the overall uniformity of the illumination across the FoV is maintained. At a relatively small magnification, as shown in (a), (b) and (d), most of the features were separated, however, the low-frequency crosstalk can still be observed in both slices. And there is no direct indication that the illumination angle constitutes to the effectiveness of separation limit. However, a smaller effective pixel size or larger magnification, can significantly improve the depth resolution. At magnification of 14.86 (c), a much cleaner separation of the two slices is shown with no presence of crosstalk. While MSE are commonly used to quantitatively assess the quality of ptychographic reconstructions, in this particular case they do not provide a meaningful reflection of image fidelity. This is due to the early proof-of-principle nature of the experiment, where overall reconstruction quality remains low and significant crosstalk is visible across both slices. As a result, visual inspection of the reconstructed slices provides a more reliable method for evaluating separation effectiveness.

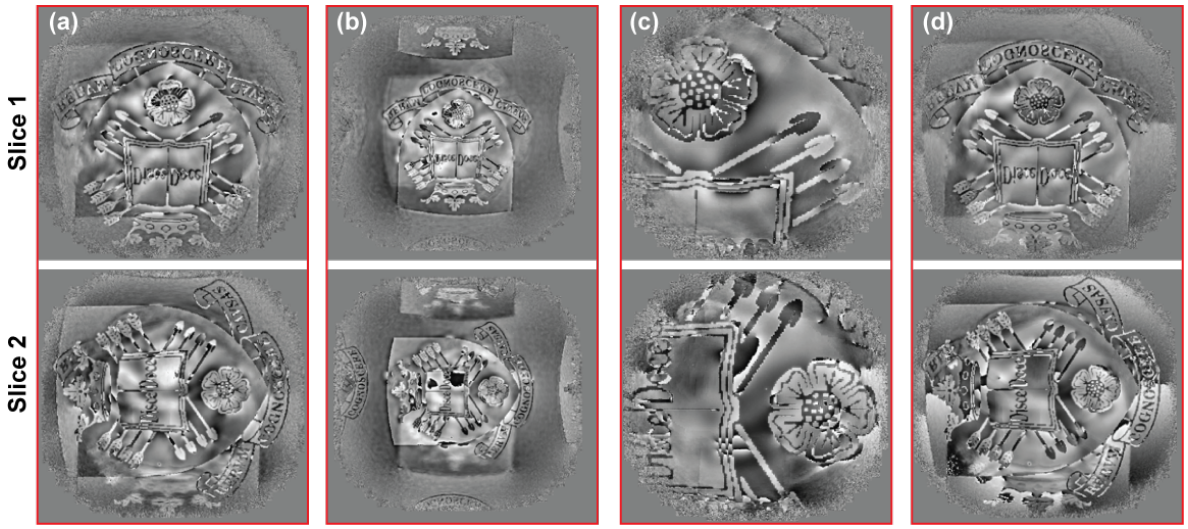

Figure 3.7. Phase reconstruction of the 2-layered sample with various magnification and illumination angle. The illumination objective lens (a)-(c) has a magnification of 40×, the geometrical magnifications are 5.9×, 3.7× and 14.86× respectively. The illumination for (d) is formed with an objective lens 20× and the geometrical magnification is measured as 5.9×.

Table 3: Experimental parameter for lensless optical near-field multi-slice ptychography

	Figure 3.6(cd)	**Figure 3.7(a)**	**Figure 3.7(b)**	**Figure 3.7(c)**	**Figure 3.7(d)**	**Figure 3.8**
Illumination objective lens	40×	40×	40×	40×	20×	40×
Camera distance z_2 (cm)	3.3	4.15	3.65	4.66	4.15	2.98
Geometrical Magnification M_{geo}	5.82	5.9	3.7	14.86	5.9	3.6
Effective pixel size dx_{eff} (μm)	2.34	2.20	3.51	8.75	2.20	1.80
Number of diffraction patterns	400					100
Scan pattern	Fermat spiral scan					
Binning factor	2					N/A
Size of diffraction patterns	1024×1024					2048×2048
Number of reconstruction iteration	300					500
update coefficient	object update coefficient α = 0.5; probe update coefficient β = 1.					α = 1; β = 1.

3.3.1.2. Bee's legs

After an initial test of the multi-slice, near-field method and of the reconstruction algorithm, further experiments were carried out on the optical bench setup shown in **Figure 3.4** with the exact parameters outlined in the experiment configuration section. This structured cone beam illumination wavefront, recovered during the reconstruction process, is shown in the bottom right corner of the **Figure 3.4**. Having passed through the thick sample, the wavefront propagates to the detector, which records diffraction patterns (as shown in bottom left of **Figure 3.4**) at a series of different sample positions. The distance between the camera and the focal point of the objective lens was approximately 4.08 cm. The distance between the camera and the sample (z_2) was 2.98 cm, giving a geometric magnification of $M_0 = 3.6$ and leading to an effective pixel spacing in the reconstruction of 1.80 μm. The test specimen in these optical bench experiments was switched to a set of bee's hind legs, approximately 250 μm thick, mounted on a standard optical microscope slide and covered by a coverslip. 100 diffraction patterns were collected using a spiral scan pattern [32] with a linear overlap between adjacent scan positions of 90%.

Assuming a best-case image resolution of double the pixel spacing in the reconstruction (3.61 μm), the DoF of the image system can be approximated using Eq. 3.2. depending on the constant c [97][98],

$$DoF \leq \frac{c{\delta_r}^2}{\lambda} = \frac{c(3.61\mu\text{m})^2}{675nm} = 20\sim100\ \mu\text{m}.$$

Feeding the bee leg data from the optical bench setup to the 3PIE algorithm, adapted as described in Section 3.1 and using six slices spaced 45 μm apart, produced the reconstruction shown in **Figure 3.8**. **Figure 3.8** shows the reconstructed phase images from the six slices: **Figure 3.8(a)** is the most up-beam slice, furthest from the camera, progressing through to **Figure 3.8(f)**, which is closest to the camera. From these images, and the accompanying zoomed-in inset images, it is clear that different features of the bee's leg are separated axially between the slices, indicating that the sample is thick enough to warrant the use of multi-slice ptychography for the reconstruction.

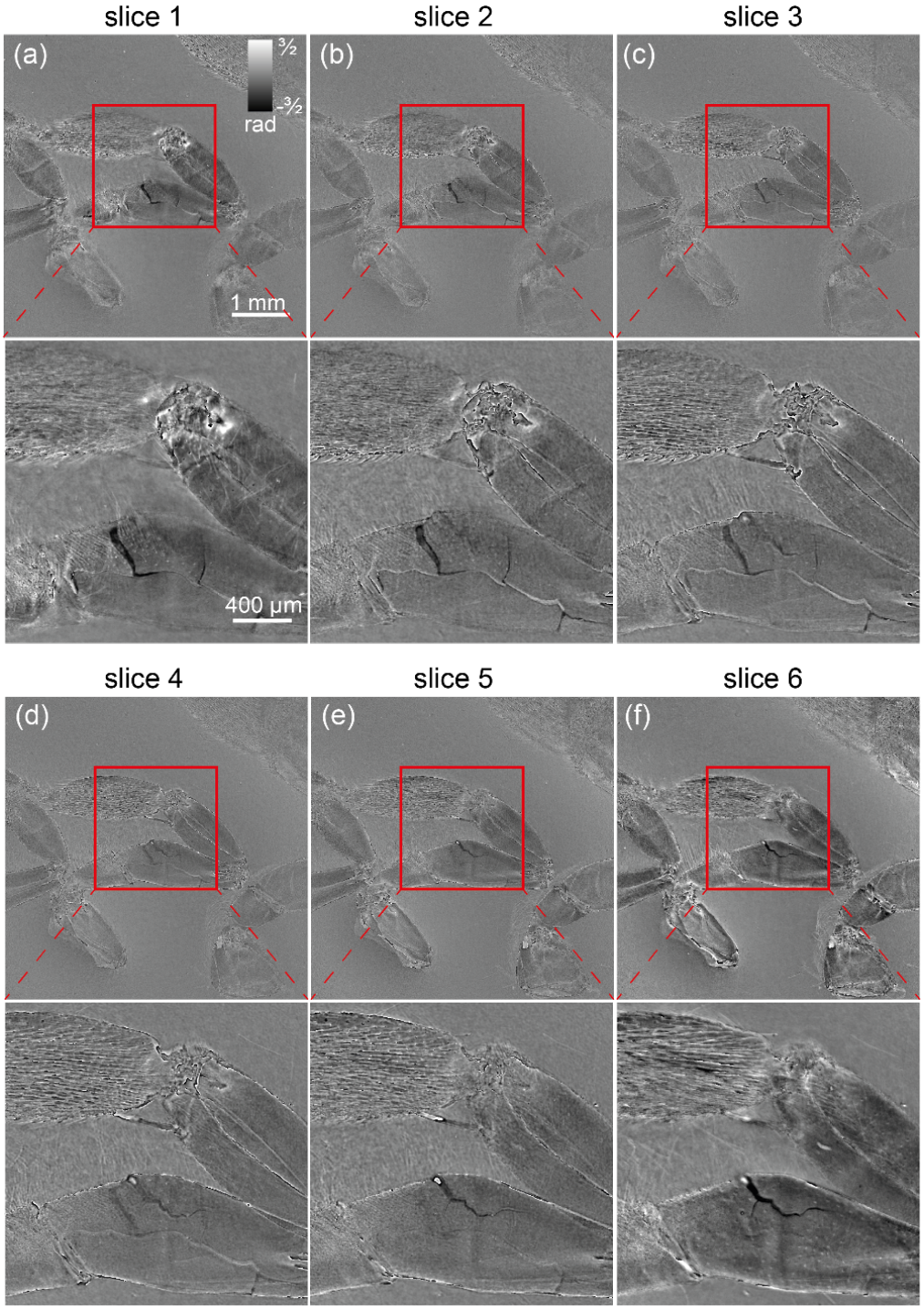

Figure 3.8. An example of a 6-layer phase image multi-slice reconstruction using the 3PIE algorithm, the sample is a bee's leg. (a-f) show the slices moving progressively up-beam, from furthest from the camera in (a) to nearest the camera in (f). The lower images in each panel show blow-ups of the areas in the red boxes. The phase ranges have been clipped in these images to enhance contrast.

To highlight the improvement in DoF of the 3D method compared to conventional near-field ptychography, we combined all six layers of the multi-slice reconstruction together by taking the pixel-wise product of all the slices. (Note: this is effective only if the pixel offsets, $r_{k,m,n}$, for each slice in the reconstruction all share the same mean centre-point, otherwise the slices do not align when the product is taken.) The resulting phase image (the sum of the phases of the six slices) is shown in **Figure 3.9(a)**. This phase image is equivalent to a cone beam projection of the sample, where the diffractive, out-of-focus features that would usually be expected for a sample of this thickness have been removed by the multi-slice reconstruction. To highlight this, the phase image resulting from processing the same data using the same algorithm, but employing only a single slice, is shown in **Figure 3.9(b)**. The single-slice images were reconstructed using 500 iterations of the same algorithm employing three slices each time, but with only the middle slice allowed to update. The front and back slices were kept as free-space (unity matrices). The slice separations were set so that the central slice was directly in the middle of the sample volume. Although image quality from the 2D reconstruction is reasonable here, closer inspection shows that the multi-slice image exhibits much better focus across all features compared to the 2D phase image.

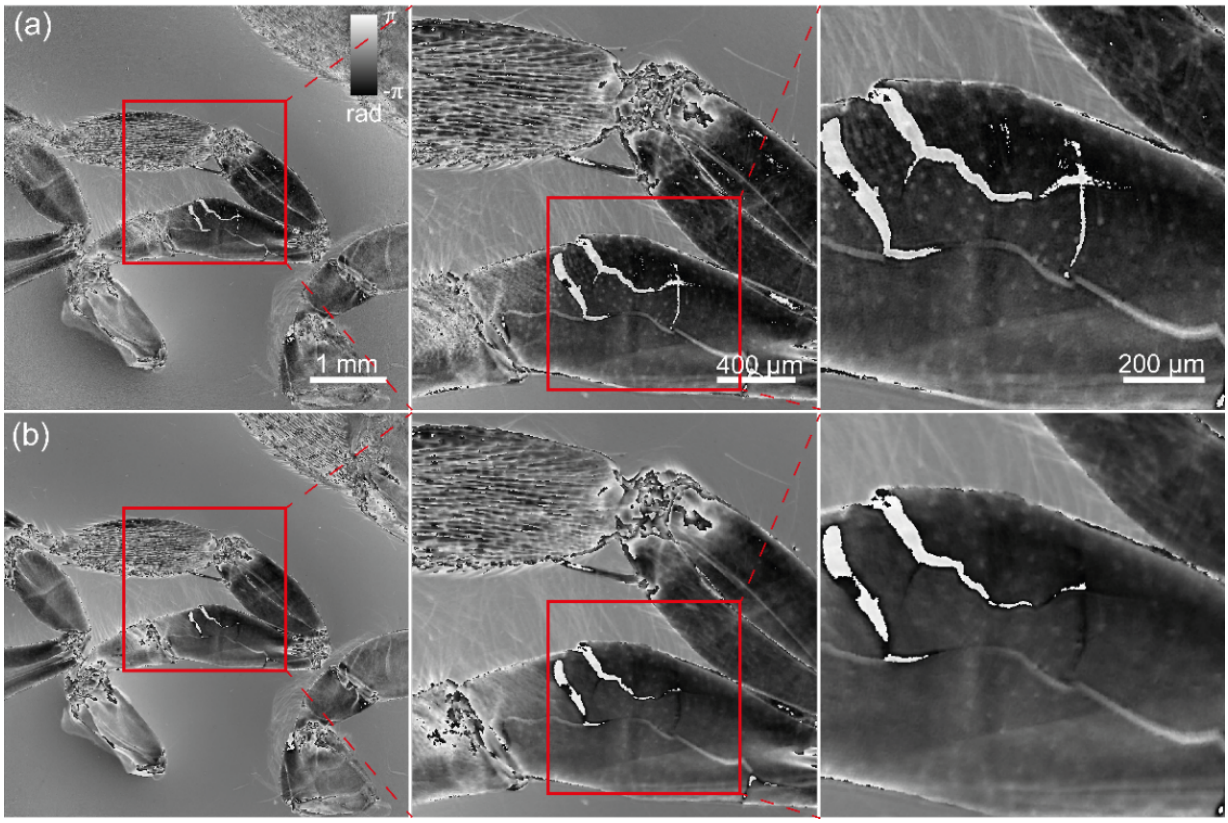

Figure 3.9. A comparison of multi-slice and single-slice reconstructions. (a) summed phase of the three slices from the 3PIE reconstruction. (b) comparative single slice phase image.

Using the same bee leg data and parameters, the minimum number of diffraction patterns required for a successful image reconstruction was then investigated. Since the data were collected using a spiral scan pattern, we reduced the number of patterns by simply discarding the outer loops of the spiral, reducing the number of patterns to 50 (**Figure 3.10(a-d)**), 25 (**Figure 3.10(e-h)**) and 15 **(Figure 3.10(i-l)**). **Figure 3.11** shows the full FoV of the summed phase images – over 25 mm^2. The results show that, for a six-slice reconstruction, effective multi-slice imaging is possible with as few as 15 diffraction patterns. Although considerable noise is introduced at this extreme, it is interesting to note that low spatial frequency content appears to reduce in contrast, as a result of under sampling from lower numbers of diffraction patterns and therefore less redundant information from the overlaps, although the high DoF of the larger scan sizes is retained. In addition, it is overserved that the absolute values of phase shift recovered changes with number of diffraction patterns. The absolute values of the recovered phase can change with the

number of diffraction patterns, especially if the dataset is limited. For quantitative phasing in near-field ptychography, a sufficient number of diffraction patterns is required to ensure accurate phase recovery. Insufficient patterns may result in phase errors, impacting the quantitative measurements.

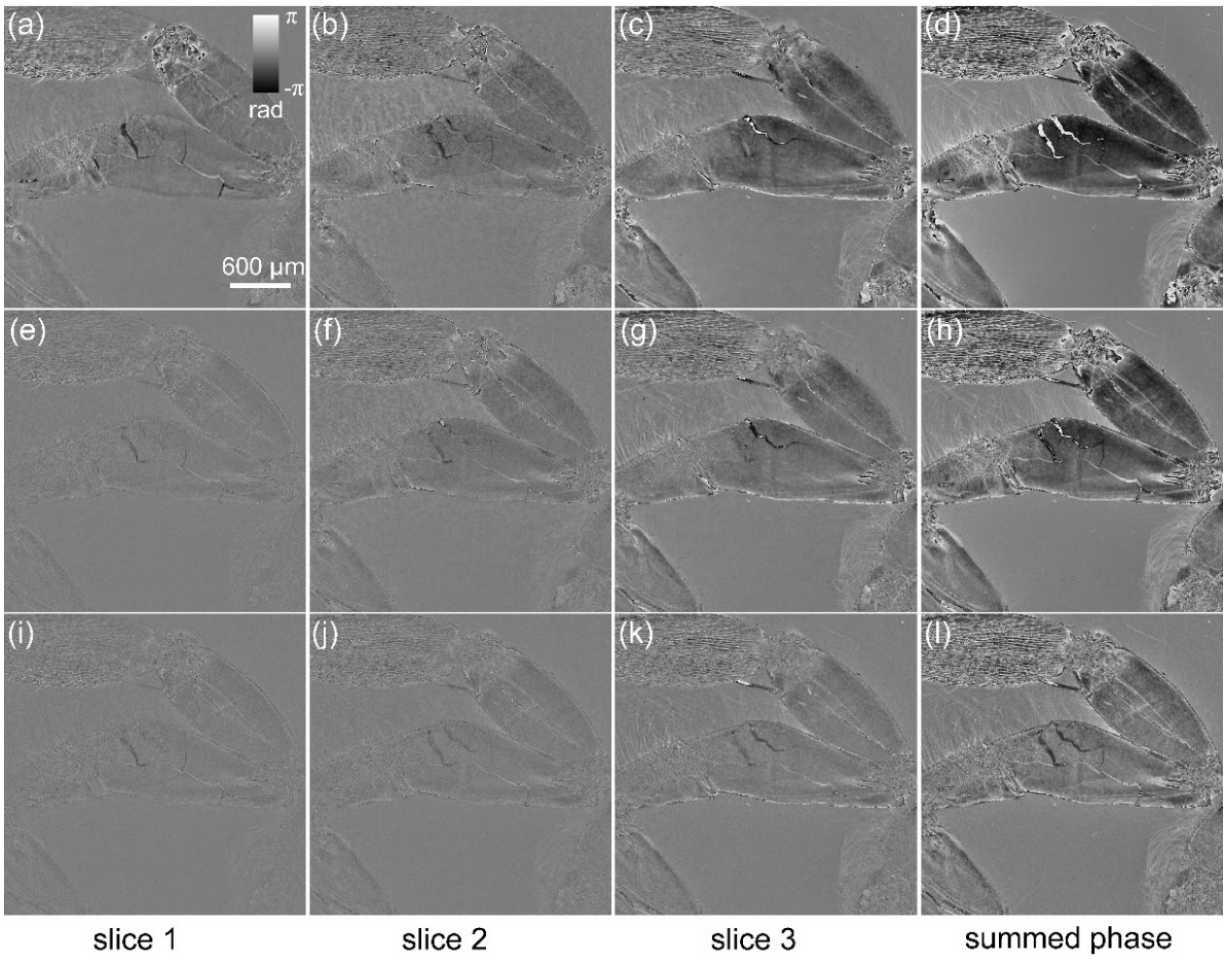

Figure 3.10. Reconstructions of 3 selected layers phase of bee's legs using 3PIE algorithm. The Column one the left shows the most down-beam side bee leg features, and the third column shows the most up-beam features. Each row represents the reconstruction data set using different amount of diffraction patterns which are dedicated as (a)-(d): 50 dps with 360 iterations; (e)-(h): 30 dps with 600 iterations; and (i)-(l): 15 dps with 1200 iterations.

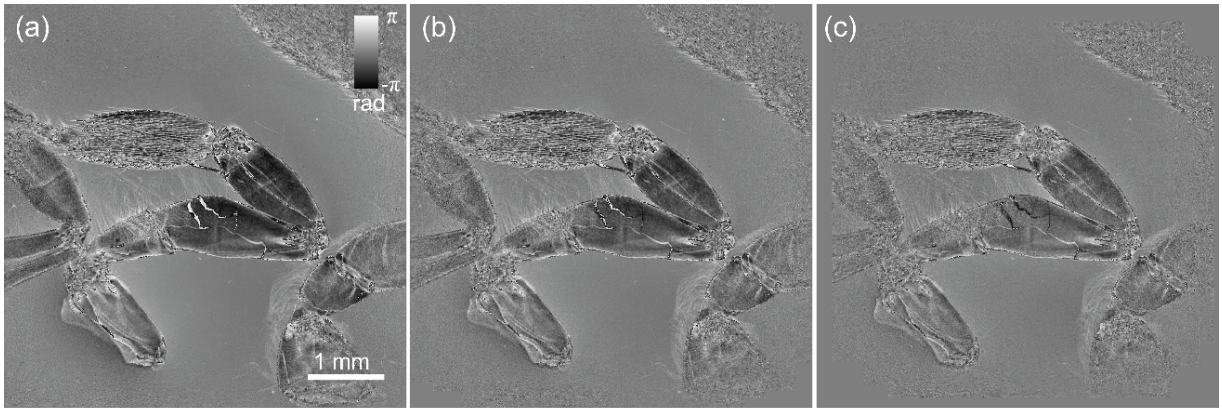

Figure 3.11. The full FoV of summed phase images from 6-layer multi-slice reconstruction of the bee's leg data, using different numbers of diffraction patterns. (a) using 50 diffraction patterns; (b) using 25 diffraction patterns; (c) using 15 diffraction patterns.

This chapter derived the geometric modifications necessary for cone-beam near-field ptychography, including the adaptation of the FST to account for varying magnification across different sample slices. These adjustments ensure accurate wavefront propagation in the near-field regime while maintaining computational efficiency. Additionally, the successful implementation of Lensless Optical Cone-beam NMP was demonstrated, addressing the DoF limitation in traditional ptychography, which restricts imaging to optically thin samples. Experimental validation confirmed that the NMP approach extends the capabilities of near-field ptychography to thicker biological samples while maintaining a large FoV and high resolution. By incorporating a multi-slice forward model into the reconstruction algorithm, this work enables volumetric imaging of samples exceeding the conventional DoF by an order of magnitude.

4. X-ray NMP via cone-beam geometry

In this chapter, two implementations of Near-field Multi-slice Ptychography (NMP) using hard X-rays at a synchrotron facility are presented. These experiments build upon the experimental and reconstruction framework developed in the optical bench experiment, demonstrating the applicability of NMP in an X-ray regime.

The primary objectives of this chapter are threefold. First, it aims to assess the feasibility of NMP in overcoming the DoF limitations inherent in conventional X-ray ptychography imaging. Second, the study evaluates the spatial and depth resolution achievable with cone-beam X-ray NMP. This involves determining the method's capability to resolve fine structural details across different sample depths. Finally, the experimental setup is optimised by refining detector selection, optical arrangements, and illumination diversity, alongside enhancing reconstruction algorithms to improve imaging result for thick samples.

This chapter starts with a brief introduction to the coherence branchline I13-1 at the Diamond Light Source (DLS) where at all the X-ray experiments in this thesis were performed. This is followed by two experiment sections. Both X-ray experiment sections start with the description of the experimental setup and the data acquisition process. In the first X-ray experiment, an indirect detector with a scintillator was implemented, whereas in the second experiment, a direct X-ray detector was implemented. Then the reconstruction results from the experiment are presented.

In the first result section, the performance of the experiment configuration and reconstruction quality is tested using a Siemens star. This initial evaluation in resolution determined the range of DoF of the X-ray NMP system. Thereby a series of test samples – including two double-layered sample and a thick, continuous sample, are designed correspondingly and utilised for the experiment. Furthermore, the near-field ptychographic multi-slice reconstruction results for those sample are presented and discussed. At the end of this section, the minimum requirement for the number of diffraction patterns to successfully carry out ptychographic multi-slice reconstruction is evaluated.

The next experiment section starts with the description of the modification and improvement upon the previous configuration. Then the Siemens star and a continuous thick sample were used to evaluate the lateral resolution and depth resolution of this alternative X-ray NMP configuration.

4.1. Introduction to I13-1 at the DLS – Coherence branchline

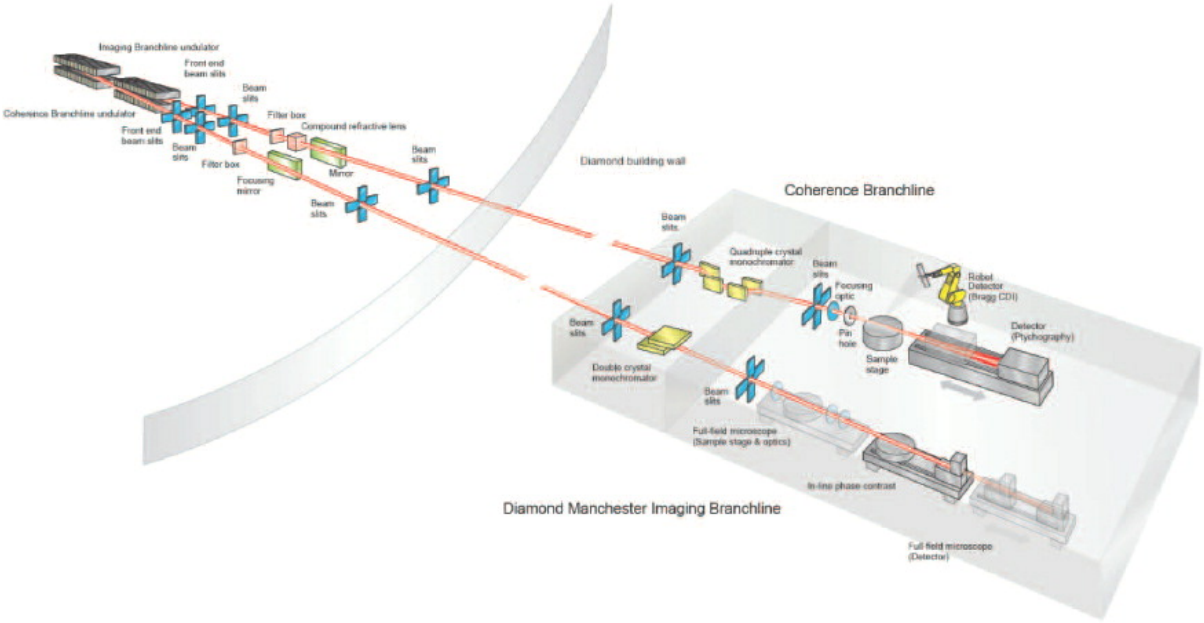

Figure 4.1: Schematic of beamline I13 in DLS. The X-ray experiments were performed in I13-1, coherence branchline. (Image © Diamond Light Source) [102]

Coherence branchline I13-1 at the DLS is one of the longest beamline branches at the third-generation synchrotron Diamond Light Source. The experimental hutch is located over 200m from the source and operates at beam energies range of 6-20 keV. The overall schematic of the branchline configuration is shown in **Figure 4.1.** To maximise the coherent flux for I13-1, a monochromator is implemented before the beam reaches the experimental hutch to minimise the beam vibration. The further coherent fraction can be adjusted by the extra sets of slits before the experiment. The typical lateral coherence length with slits size of approximately 50 µm is reported to be larger than 300 µm [102].

4.2. X-ray Experiment 1

4.2.1. Experimental configuration

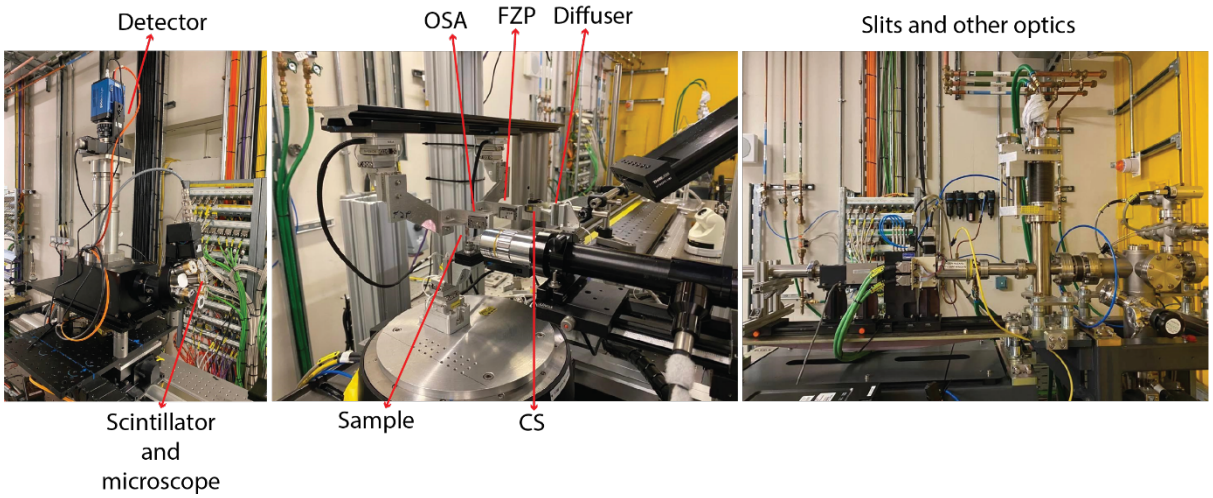

Figure 4.2. Photography of X-ray near-field multi-slice ptychography experimental configuration in I13-1

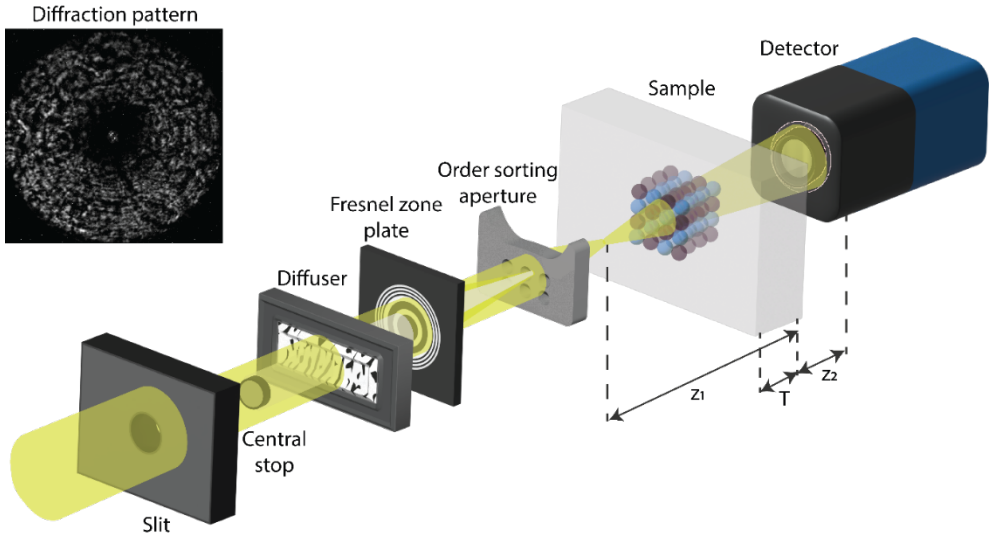

Figure 4.3. Experimental configuration for X-ray near-field multi-slice ptychography

A photograph of the main experimental configuration is shown in **Figure 4.2** and a schematic diagram of the experimental setup is shown in **Figure 4.3**. The beam energy was 9.7keV corresponding to a wavelength of 0.124 nm. The beam was focused using a Fresnel zone plate with a diameter of 180 µm and outer zone width of 50 nm, resulting in a convergence

angle of 2.6 mrad. The intense zero-order beam was eliminated by inserting a gold central stop. A 20 µm order sorting aperture was placed further down-beam of the zone plate. A sheet of paper was placed approximately 1 cm up-beam of the zone plate as a diffuser to introduce a structured speckle into the illumination. The detector (a PCO 4000) had a dynamic range of 5455:1 and a pixel pitch of 9 µm. It imaged a scintillator through a microscope objective with a 20× magnification.

For data collection, the sample was placed approximately 2.5 cm (z_1) from the zone plate focus and the scintillator was a further around 32.5 cm (z_2) down-beam. The resultant geometric magnification, M_0 varied between 13-14 due to slight changes in the sample position and its different thicknesses in the experiments. Its precise value was determined by trial and error during the reconstruction process. Due to the inefficiency of the X-ray optics, the counts acquired in the experiments was particularly low. Therefore, each diffraction pattern required an exposure time of at least 15 seconds and was binned by a factor of 2 to 1024×1024 pixels. A dark frame recording was subtracted from the data and any negative-valued pixels set to zero. Due to the changes in geometrical magnification between the different experiments the pixel pitches in the reconstructions ranged from 64 – 69 nm. All diffraction data were collected using a raster scan with random offsets added to eliminate artefacts that can arise with a periodic grid [32]. The step size was calibrated through the initial Siemens star experiments and achieved best results with a step size of 10 µm (an overlap ratio between scan positions of ~86%), plus random perturbations to the regular grid of ± 2.5 µm. An example diffraction pattern is also shown in the top left of **Figure 4.3**. Patterns that just filled the detector, and did not extend beyond it, gave the best compromise between flux and field of view.

Compared to the optical bench work, the available flux here was lower because of losses in the Fresnel zone plate and the scintillator, and diffraction data suffered from high noise and low counts (reducing from >10000 per pixel to <1000 per pixel).

Table 4 summarises the experimental parameter used for both X-ray experiment and reconstruction.

Table 4: Experimental parameters for the X-ray near-field multi-slice ptychography

	Siemens star (**Figure 4.4**)	1mm 2-layer sample (**Figure 4.5**)	0.5mm 2-layer sample (**Figure 4.6**)	2.5mm continuous sample (**Figure 4.7**)	Siemen star (**Figure 4.10**)	1mm continuous sample (**Figure 4.13**)
Detector pixel pitch size (μm)	9				55	
Microscope objective	20×				N/A	
Geometrical Magnification M_{geo}	14	13.6	13.3	13.6	1300	1100
Effective pixel size dx_{eff} (nm)	64.3	71.4	67.7	66.2	42.3	50.0
Number of diffraction patterns	11×11	10×10	10×10	10×10	50x50	50x50
Scan pattern	Raster grid scan					
Line-overlap	86% ± 20% offset				90%	
Binning factor	2				NA	
Size of diffraction patterns	1024×1024				512×512	
Number of reconstruction iteration	500				500	
Update coefficient	object update coefficient α = 1; probe update coefficient β = 1.				α = 0.5; β = 0.5.	

A Siemens star sample was used initially to calibrate and optimise the setup. The best phase image from these initial 2D experiments is shown in Error! Reference source not found.**(a)**, together with a contrast-boosted zoom-in. The corresponding reconstruction of the structured cone beam is shown in **Figure 4.4**, showing the speckled phase (colour) and amplitude (brightness) introduced by the diffuser and the hollow donut centre resulting from the up-beam central stop. The 2D Fourier transform shown in **Figure 4.4(c)** of the central region of the Siemens star, indicates the cut-off frequency approximately $7.56 \times 10^6/m$, which corresponds to 133 nm resolution. The thickness limit dictated by Eq. 3.2 for this setup, with an X-ray wavelength of 0.124 nm and a resolution of 133 nm, can then be calculated,

$$T_{min} = DoF \leq \frac{c{\delta_r}^2}{\lambda} = \frac{c(133\text{nm})^2}{0.124nm} = 0.142{\sim}1 \text{ mm}.$$

4.2.2. Sample preparation

The two-layer sample was fabricated using a mixture of 2 – 20 µm hollow glass beads gently blown on Kapton discs and mounted on both sides of washers that were 1 mm and 0.5 mm thick. The continuous sample was made from paraffin wax melted on a hot plate in an aluminium foil container mould at 70 degrees. A mixture of the same 2-20 µm diameter hollow glass beads were gently stirred into the liquid paraffin wax until the mixture was evenly distributed, then the mould was removed from the hot plate to cool down until solid. The paraffin block was afterwards manually trimmed and shaped into a cuboid with 2.5 mm thickness.

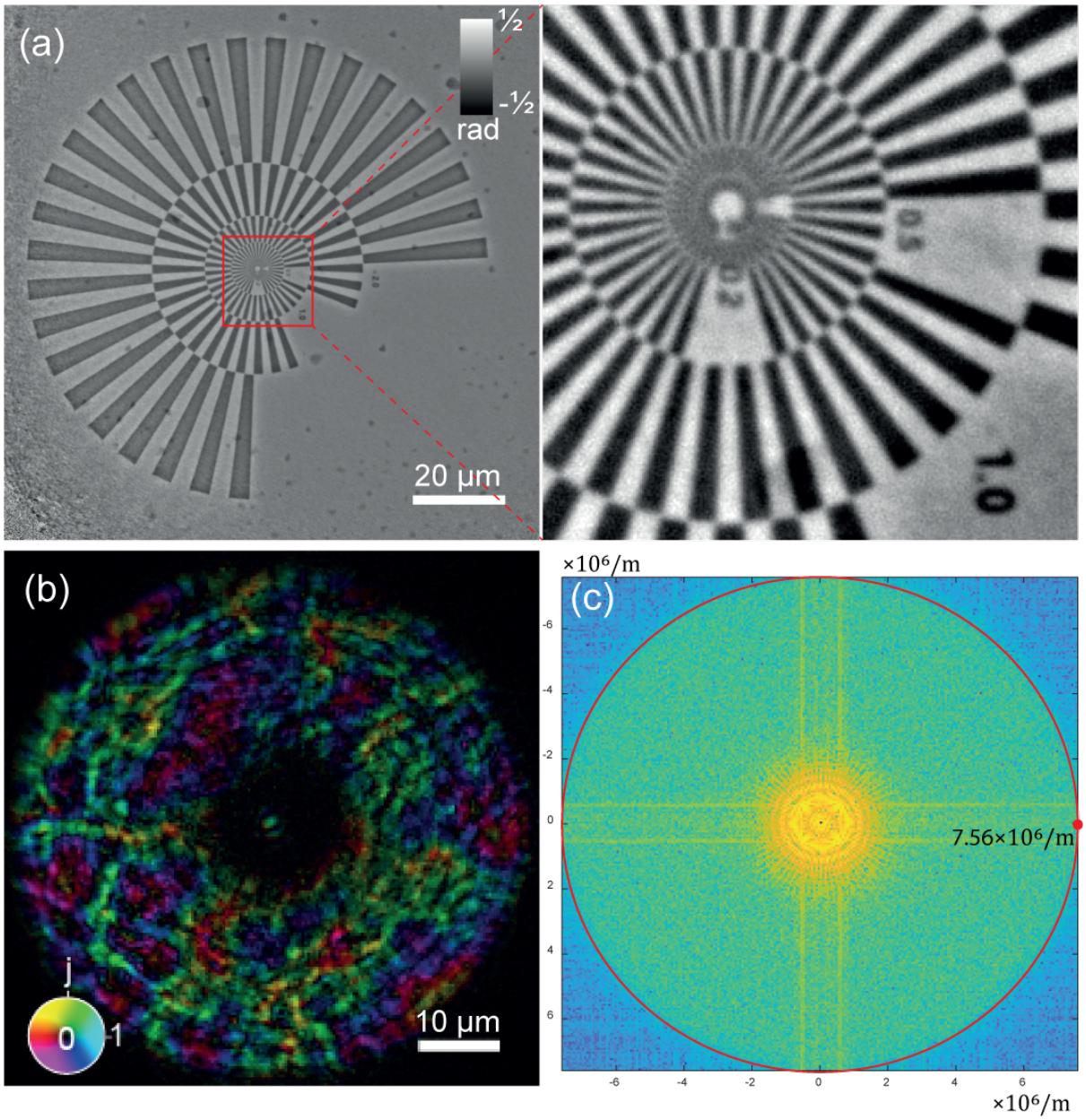

Figure 4.4. Results from a calibration experiment of the X-ray near-field setup, using a Siemens star test sample. (a) the reconstructed phase image of the sample, showing also a phase-boosted zoom of the area in the red box. (b) a colour-wheel representation of the reconstructed illumination wavefront, where colour indicates the phase and brightness indicates the amplitude of the reconstruction. (c) is the 2D Fourier transform of the zoomed-in region shown in (a).

4.2.3. Experiment results

4.2.3.1. Double layered sample

Having determined from the Siemens star tests the geometry, resolution and magnification ($M_0 = 14$) of the setup, we next replaced the star with various thicker samples. Two double-layer samples with 1 mm separation distance were made to test the DoF. Due to the sample's thickness and inaccuracies in its positioning in the beam, the geometric magnification in this experiment was $M_0 = 13.6$, slightly lower than for the Siemens star setup, but data was collected in an identical manner. The 3PIE reconstruction, using two slices spaced 1mm apart to match the measured sample properties, is shown in **Figure 4.5(a-d)**. As shown in **Figure 4.5(a)** and **Figure 4.5(b)**, the reconstruction effectively separated the two layers of balls. In fact, clear separation of the spheres is achieved within only a couple of iterations of the algorithm, with full convergence observed after only 50 iterations.

This indicates that the sample is near the limit of thickness for which 2D ptychography is effective but does not exceed it greatly. The fact that the reconstruction converges quickly (within 50 iterations) suggests that the sample behaves in a way that is mostly compatible with a 2D model. If the sample were significantly thicker than the limit for 2D ptychography, a slower convergence would be expected, as the algorithm struggles to resolve complex multiple scattering effects. Therefore, the clear depth separation of the two layers is therefore unexpected.

The two separate layers are combined by pixel-wise multiplication in **Figure 4.5(c)** and for comparison the same dataset reconstructed using only a single slice is shown in **Figure 4.5(d)**. Although most features are still present in the 2D image, resolution is reduced considerably and the whole image is blurred, implying that the effective reconstruction plane of the 2D image – which is "chosen" by the algorithm in the sense that it is defined by the concurrent reconstruction of the structured illumination profile – falls somewhere between the two Kaptan film layers. It appears to be a trait of ptychography generally that blind recovery of the probe results in some self-adjustment of the reconstruction plane, to a location that gives a best fit to the measured data.

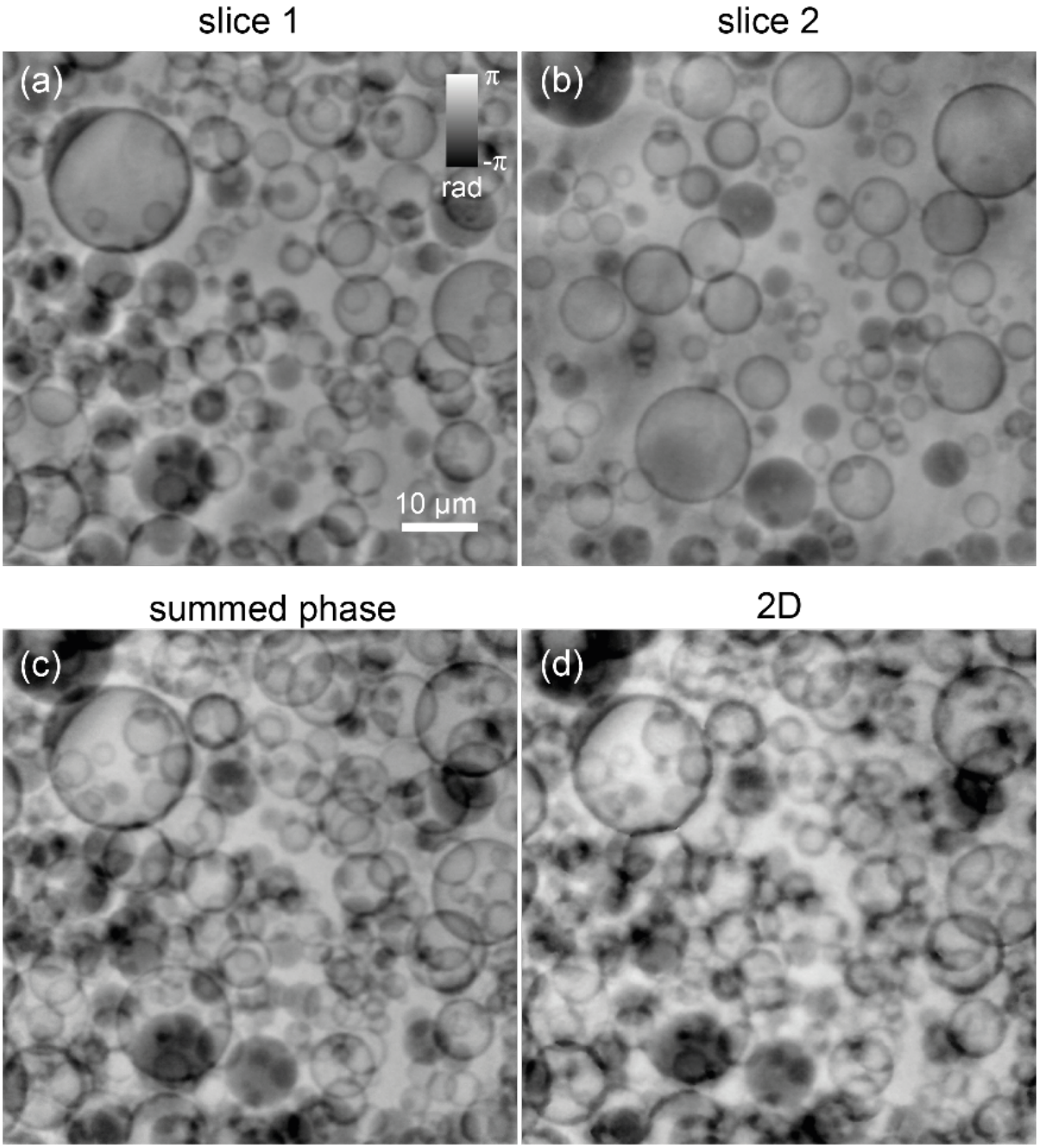

Figure 4.5. A 2-layer 3PIE reconstruction of a sample comprising two Kaptan films populated with microspheres and separated by a 1mm airgap. (a) and (b) phase images of the two slices, where (a) is the up-beam plane and (b) is the down-beam plane. (c) pixel-wise sum of the multi-slice layers. (d) the corresponding single-layer reconstruction.

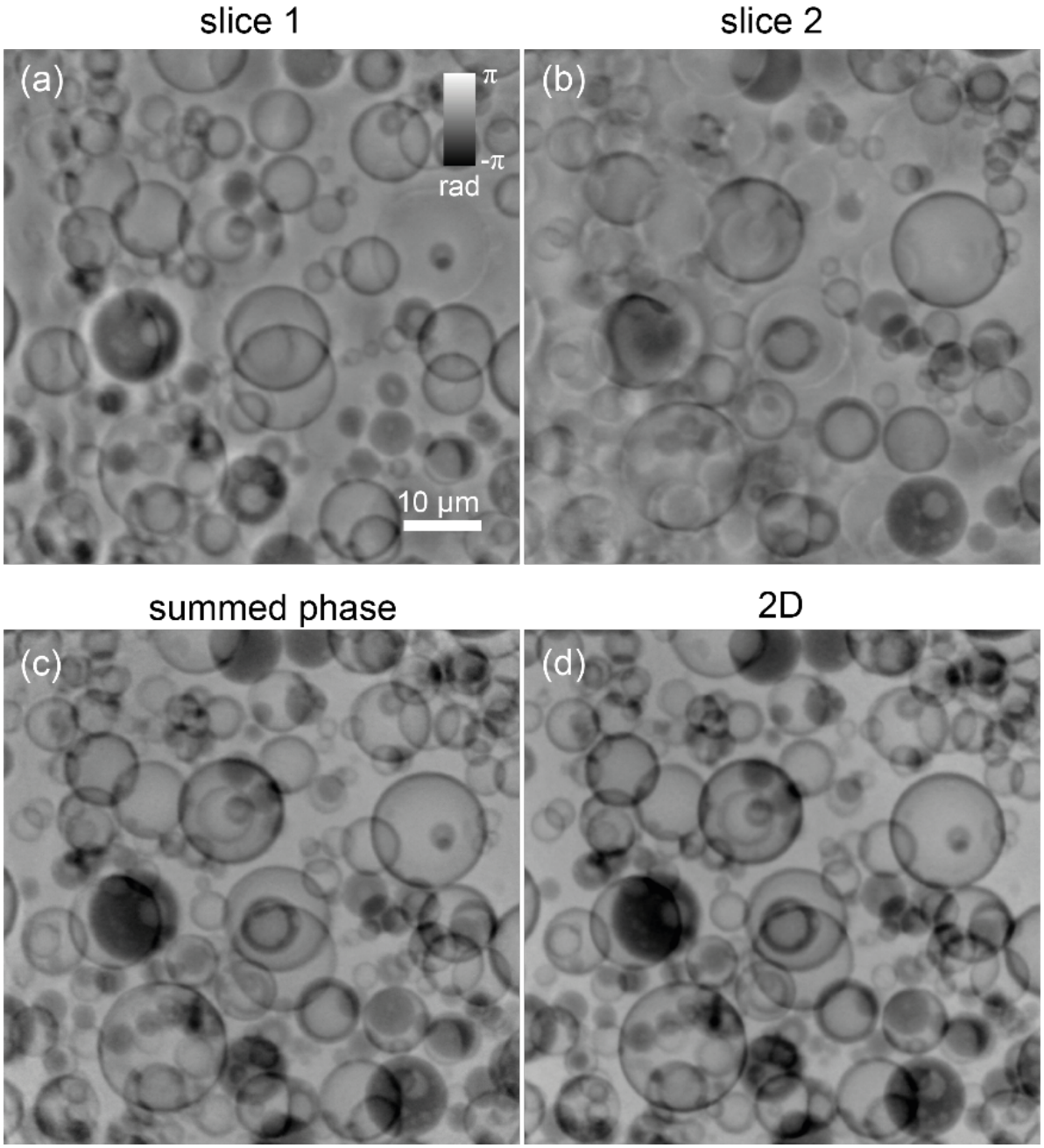

Figure 4.6. A 2-layer 3PIE reconstruction of a sample comprising two Kaptan films populated with microspheres and separated by a 0.5 mm airgap. (a) and (b) phase images of the two slices, where (a) is the up-beam plane and (b) is the down-beam plane. (c) pixel-wise sum of the multi-slice layers. (d) the corresponding single-layer reconstruction.

To further test the separation limit of our setup, a second two-layer sample was imaged with the same configuration, this time with a 0.5 mm separation – at the very lowest end of the DoF according to Eq. 1.2. The diffraction patterns data were captured in the same style, with a magnification measured at $M_0 = 13.3$ in this instance. The reconstruction results are shown in **Figure 4.6**. Reasonable separation of the two layers is still apparent in **Figure 4.6(a)** and **Figure 4.6(b)**, although the slices now exhibit noticeable cross-talk. These effects cancel each other out in the pixel-wise multiplication of the two slices shown in **Figure 4.6(c)**, to give a well-focussed 2D cone beam projection, but there is now little to distinguish this image from the single-slice reconstruction of **Figure 4.6(d)**. Again, the clear depth separation is surprising, given that diffraction of the beam in the space between the two film layers is minimised, such that 2D ptychography provides a well-focussed image shown in **Figure 4.6(c)** – if diffraction within the sample volume can be neglected, the extra depth information recovered is unexpected.

4.2.3.2. Continuous sample

The NMP method was then tested on the 2 continuous paraffin sample with total thickness of 2.5 mm as described above. Again, diffraction data were collected in the same manner, with a magnification of $M_0 = 13.6$ in this instance. A 3-slice model was used to reconstruct this data, where the separation distances were set to 1mm to ensure the whole sample thickness fell within the DoF of one of the slices. The reconstructed phase images of each slice and the corresponding pixel-wise product of the slices are shown in **Figure 4.7**. The phase images of the three layers are shown in **Figure 4.7(a-c)**, where **Figure 4.7(a)** is the up-beam layer, **Figure 4.7(b)** is in the middle and **Figure 4.7(c)** is the down-beam layer. Sectioning of the spheres contained in the paraffin into the different slices of the reconstruction is evident in these figures. The pixel-wise product is shown in **Figure 4.7(d)**, and whilst the single-slice image of **Figure 4.7(e)** at first glance does not appear to differ greatly from the pixel-wise product, on closer inspection several microspheres, especially those from the slice shown in **Figure 4.7(a)**, have all but disappeared from the 2D image (as highlighted in the red boxes shown in **Figure 4.7(e)**).

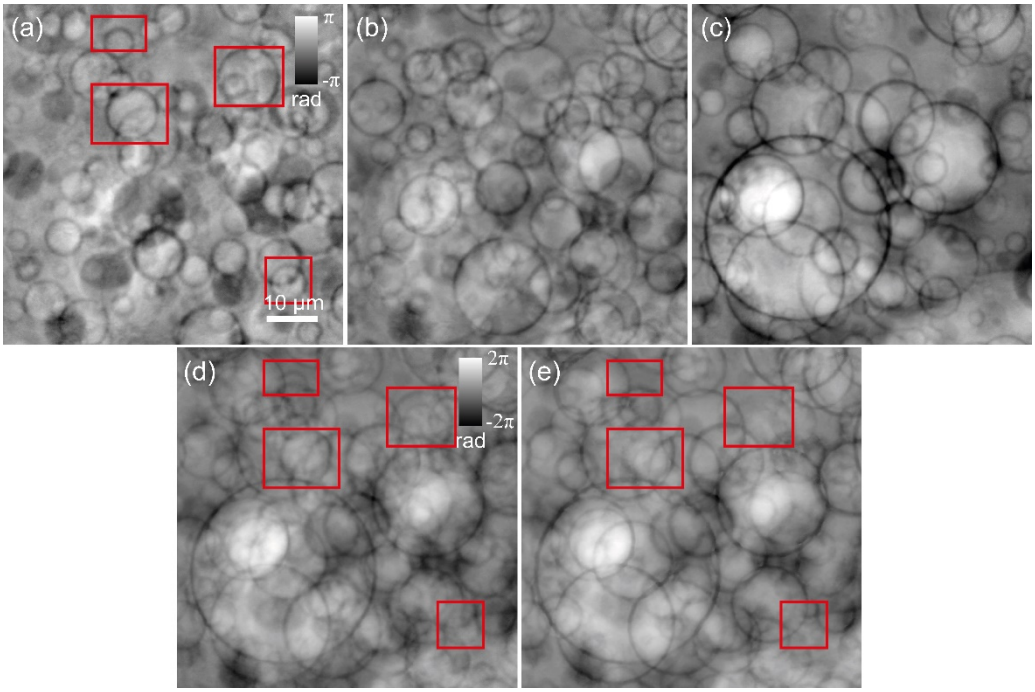

Figure 4.7. Reconstruction of microspheres embedded in paraffin, using a three-slice multi-slice model with 1mm separation between the slices. (a), (b) and (c): Phase images of each slice, where (a) is the upper stream plane (b) is the middle plane and (c) is the down-beam plane. (d) summed-phase projection of the three slices, with phase unwrapped. (e) single-slice reconstruction, with phase unwrapped. The red boxes indicate areas where microspheres have disappeared in the single-slice image.

4.2.3.3. Investigation of minimum diffraction pattern number

In this section, the lower limit of diffraction pattern number on the X-ray data is investigated. **Figure 4.8(a-d)** shows that when the diffraction pattern number is decreased from 121 to 49 (a sub-set of the original data created by extracting the central 7×7 scan positions), a relatively high-quality reconstruction is still achieved. However, there is no significant resolution loss compared to the larger scan as less redundant information was obtained from the diffraction pattern data set. A further reduction in the diffraction pattern number to 36 still achieves some degree of separation in the slices, albeit with a significant increase in noise. When the number of total diffraction patterns is reduced to 25, the reconstruction starts to fail, especially for the two up-beam slices. Accordingly, the final summed-phase image also shows poor quality. That this lower limit for the X-ray data is higher than it was

for the optical bench results described in Section 3.3.1.2 is not unexpected, given the relative increase in noise and lowering of flux.

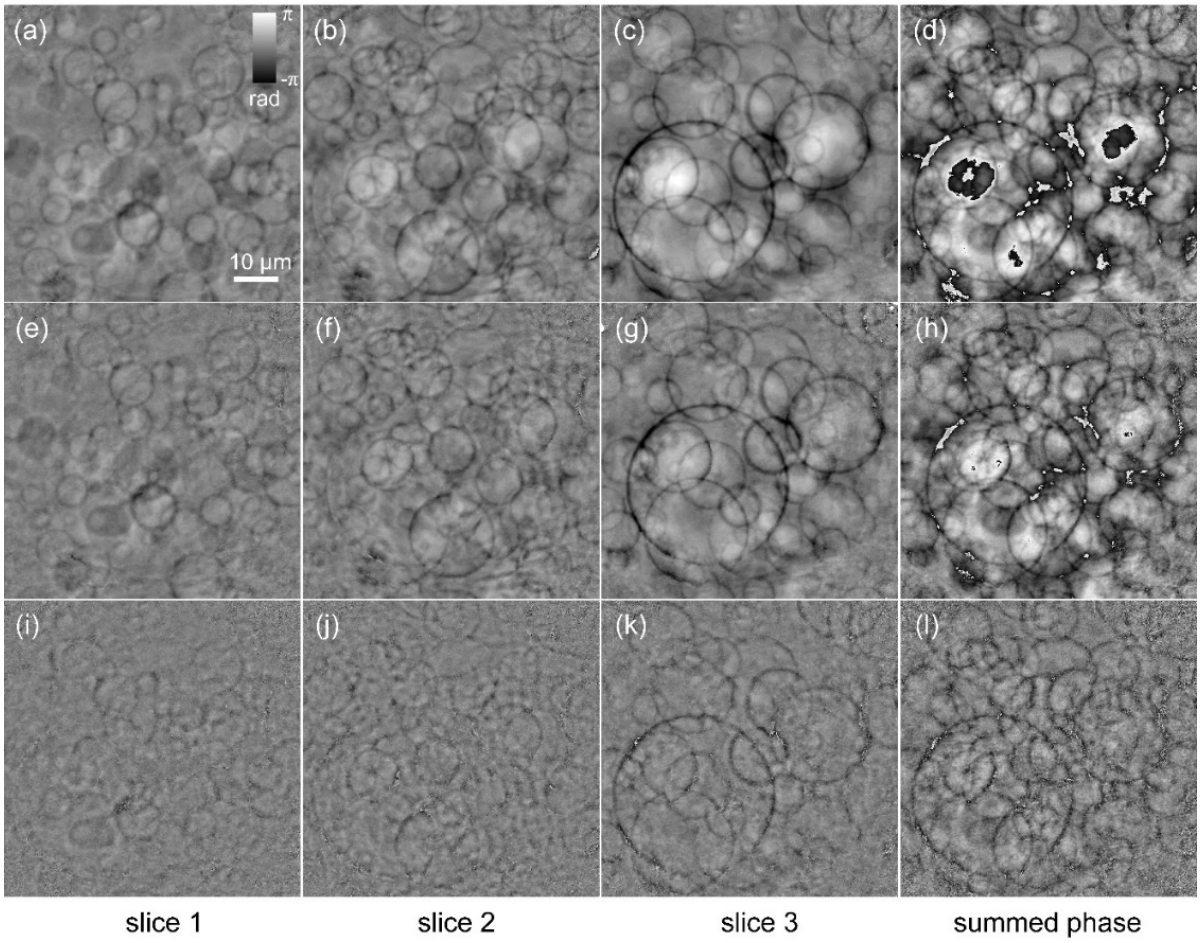

Figure 4.8. Phase images of a three slice 3PIE reconstruction with a reduced number of diffraction patterns. (a)-(c) phase images of each slice when using 49 diffraction patterns in a 7×7 grid; (d) summed phase of the three slices; (e)-(g) phase images of each slice when using 36 diffraction patterns in a 6×6 grid; (h) the summed phase; (i)-(k) phase images of each slice when using 25 diffraction patterns in a 5×5 grid; (l) summed phase.

4.3. X-ray experiment 2

4.3.1. Experimental configuration

The initial experiments described in the previous section suffered several issues. Firstly, the resolution achieved in the first experiment was limited to 200 nm, which consequently restricted the depth resolution to approximately 1 mm. Secondly, the total counts in the diffraction patterns collected from the experiment were very low due to the inefficient X-ray optics. Specifically, the high angle Fresnel zone plate had less than 50% efficiency, and the requirement of a scintillator for the indirect detector further reduced the available counts. Due to the low available flux, a sheet of paper was initially used as the diffuser, which did not provide sufficient high-frequency components as the illumination modulator. The lack of illumination diversity also limited the overall reconstruction effectiveness.

To address those mentioned issue, several adjustments were made to improve optics efficiency and illumination diversity:

The main configuration for the X-ray experiments can be referenced in **Figure 4.3**. The beam energy was slightly adjusted from the initial experiment and set to exactly 10 keV, corresponding to a wavelength of 0.124 nm. The beam was focused using the same optic setup as configuration 1 shown in **Figure 4.3**. To increase the diversity of the illumination, a sheet of 2000p sandpaper was used instead of a piece of paper and placed approximately 1 cm up-beam of the zone plate to act as a diffuser, introducing much stronger and finer speckles. To achieve the highest possible count, instead of using the scintillator and microscope with a small-pixel detector, a direct X-ray photon detector (Merlin Quad) with large pixel size was used in the experiment, which had a pixel pitch of 55 μm and full detector dimension of 512×512 pixels.

The sample was placed approximately 0.6 cm (z_1) down-beam from the Fresnel zone plate focus point and the detector was positioned a further 7.74 m (z_2) down-beam. The actual resulting geometric magnification, M_0, ranged between 1100-1350 due to slight changes in the sample position and the different thicknesses in subsequent experiments. Similarly to the previous X-ray experiment, the precise value of the magnification needed to be determined through trial and error during the reconstruction process. The higher optics

efficiency leads to a reduction in exposure time to around 2 seconds per diffraction pattern. The full detector size with 512×512 pixels was utilised for data collection. No dark frame was recorded. The final pixel pitches in the reconstructions ranged from 57 – 62 nm due to the variation in the geometric magnification. All diffraction data sets were collected using the same strategy as described in X-ray experiment 1. The scan step size was however reduced to 2 µm due to the small illumination size of 20 µm, which corresponds to an overlap ratio between scan positions of approximately 90%. Addition random offset of ± 20% of the step size was required to eliminate the artefact induced by a regular scan pattern.

Figure 4.9 shows the two example diffraction patterns, one collected from the initial experiment (**Figure 4.9(a))** and the other one from the improved experimental configuration (**Figure 4.9(b)**). The average intensity of the diffraction pattern shows about a threefold improvement. However, due to the sampling condition, the diameter of the illumination only occupies about 2/3 of the full detector size (512×512 pixels). Furthermore, the detection panel on Merlin Quad detector is dived into 4 sub-regions, so when the full detector is utilised, a "cross" artefact can be observed in the collected diffraction patterns (as shown in **Figure 4.9(b)**). Consequently, an extra pre-processing step need to be undertaken, where a Gaussian smooth mask is applied to the cross region.

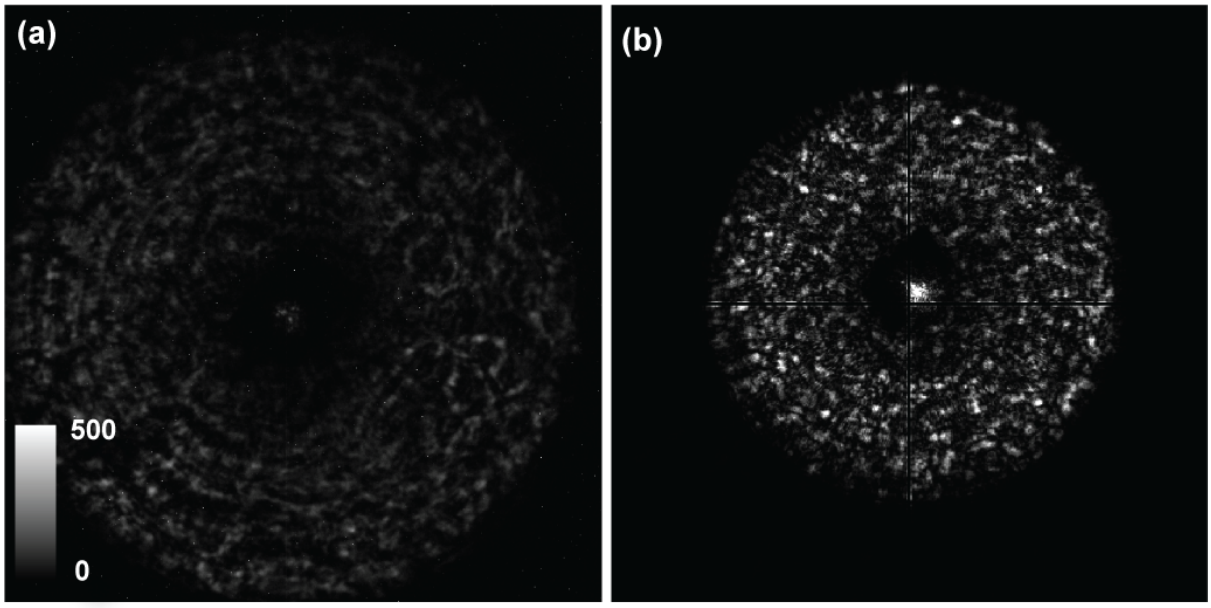

Figure 4.9. Example diffraction patterns, (a) the diffraction pattern collected from X-ray experiment 1 with dimension of 1024x1024 pixels with pixel pitch of 18 µm, (b) the diffraction pattern collected from X-ray experiment 2 with dimension of 512×512 pixels with pixel pitch of 55 µm.

4.3.2. Experiment results

4.3.2.1. Siemen star

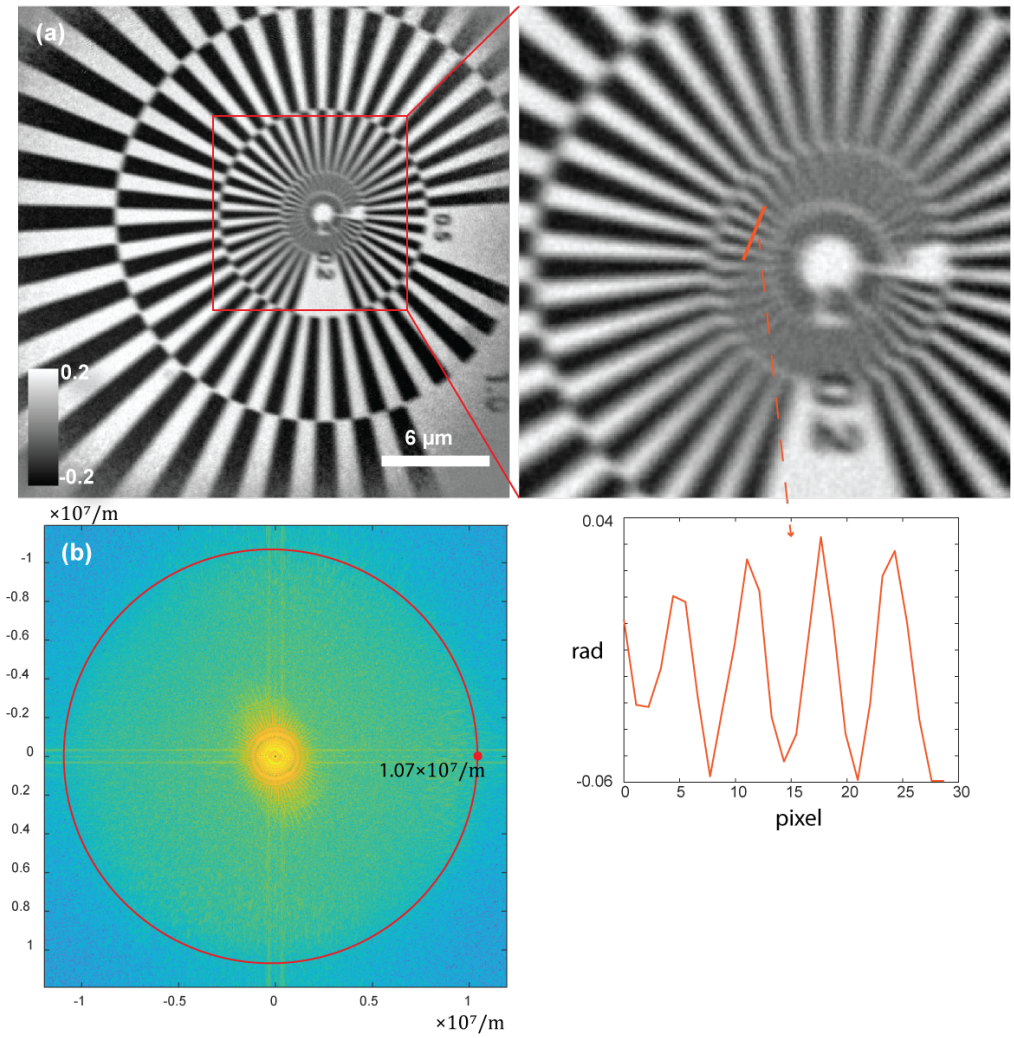

Figure 4.10. Results from a calibration experiment of the new x-ray near-field setup, using a Siemens star test sample. (a) the reconstructed phase image of the sample, with a zoomed-in area indicated by the red box. The orange-coloured bar shows the line profile, indicates the resolution around 100 nm. The blur in x-direction is likely to be caused by the mechanical instabilities in the sample stage or beam drift that was introduced by systematic shifts that degrade resolution along the drift direction. (b) is the corresponding 2D Fourier transform of the zoomed-in area shown.

Again, a Siemens star was used to calibrate the initial experimental configuration. The best reconstructed phase image is shown in **Figure 4.10**. The zoomed-in feature indicates the

lateral resolution around 100 nm, estimated from Siemens star reconstruction. The 2D Fourier transform also shows a cut-off frequency of 1.08×10^7/m (equivalent to resolution just below 100 nm). Both values demonstrate twofold improvement upon the previous configuration. The recovered probe illumination shown in the **Figure 4.11(a)** , with the bottom half, **Figure 4.11(b)** showing the recovered probe illumination of the Siemens star sample from first X-ray experiment. The corresponding frequency domains of both probes are shown on the right, respectively. Compared to the illumination in the previous experiment, the recovered probe in the top figure shows much finer and randomised speckle employed in the new experiment, with speckle feature sizes spread out between 100 – 400 nm on average which is a good match with the NA of the design imaging system. Consequently, the much more even distribution across the entire frequency spectrum is shown in **Figure 4.11(a)** also indicates the high diversity of the modulated illumination. Whereas as shown in **Figure 4.11(b)** the probe recovered from the previous experiment consisted of average speckle size around 5 – 10 µm, which is way below the system NA. The strong central low frequency distribution around 1.5×10^6/m shown in **Figure 4.10(b)** indicates this relative low diversity of the illumination. The diffuser speckle in the new experiment is 50–100 times smaller in average, reflecting a more diverse and better-modulated illumination, which leads to more diverse and evenly distributed frequency spectrum, enabling the recovery of higher resolution details.

However, due to the misalignment of the OSA, the new experiment unfortunately suffered from diffraction from the unwanted direct beam, which mean degrees of inhomogeneity from the other diffraction order contributed to the blur and soft edges effects, and overall reduced phase contrast observed in the final reconstruction result.

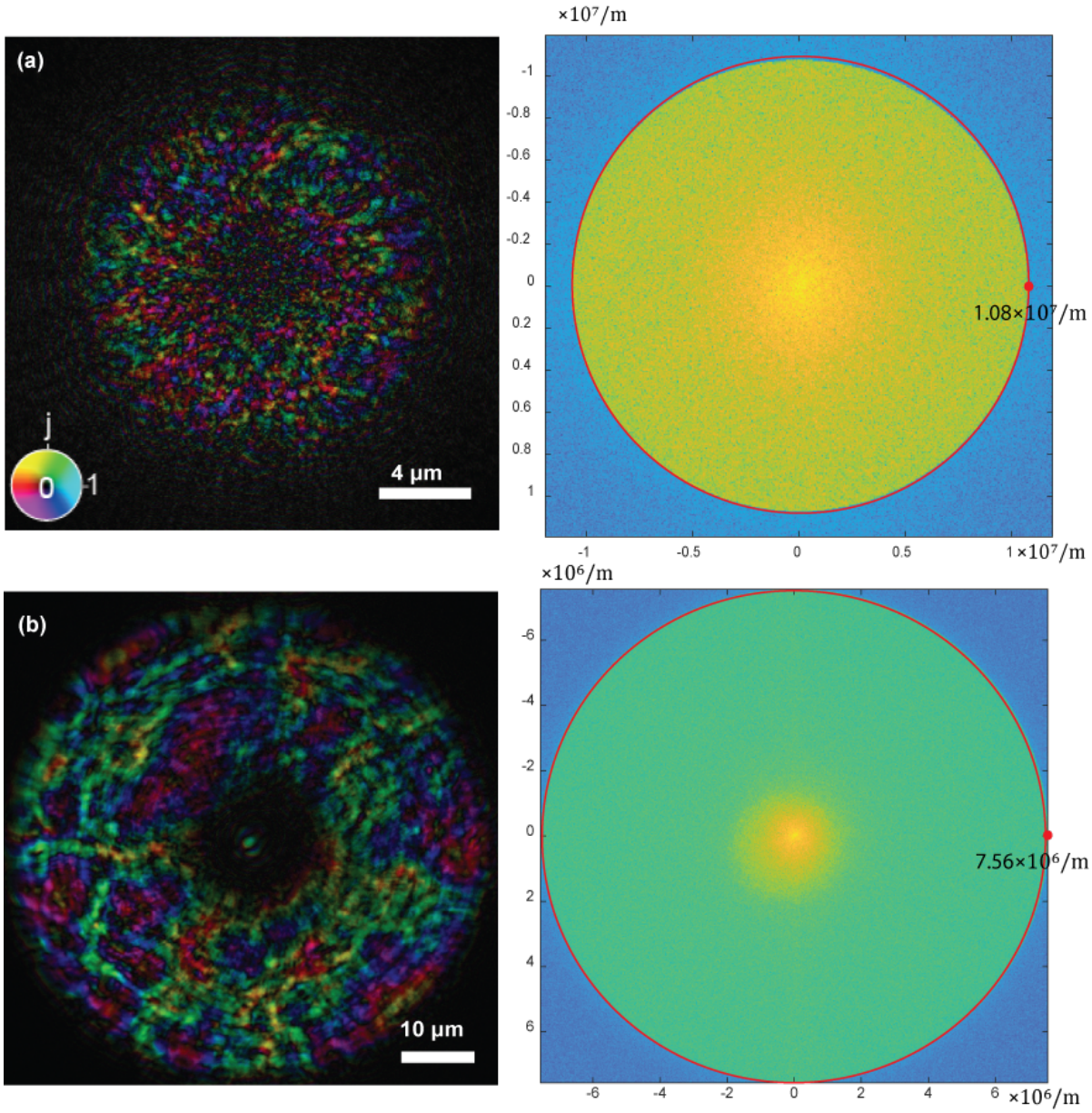

Figure 4.11. Colour-wheel representation of the reconstructed illumination wavefront with the corresponding 2D Fourier transform on the right, where colour indicates the phase and brightness indicates the amplitude of the reconstruction. (a) probe reconstruction of the new experimental configuration. (b) probe reconstruction from the previous experiment.

4.3.2.2. Paraffin beads

The depth resolution of the new X-ray NMP system then was approximated using Eq. 3.2, where the DOF is directly proportional to the squared value of the resolution:

$$T_{min} = DoF \leq \frac{c{\delta_r}^2}{\lambda} = \frac{c(100\ nm)\text{^}2}{0.124\ nm} = 160 - 400\ \mu\text{m},$$

which gives the theoretically DoF of the new experiment configuration somewhere between 160 μm to 400 μm. This compares well with configuration 1 where the DoF was from 0.142 -1 mm. After the initial evaluation with the Siemens star, the same experimental system was used to image a continuous 1 mm paraffin block populated with randomly scattered glass beads as in configuration 1.

For the reconstruction process, the magnification variation between each layer due to the cone-beam configuration was calculated and scaled using the equivalent geometry described in **Figure 3.3(b)**. The magnification of the most down-beam slice was set to 1100, which corresponding to an effective pixel size of 65 nm.

Due to the small but highly diverse illumination (approximately 20 μm^2) and small step size, 2500 diffraction patterns (via 50 × 50 pixels raster grid scan) were collected in the experiment to achieve field of view of just over 100 μm^2. The probe was split into three modes (as shown in **Figure 4.12**), which significantly accelerated the probe convergence speed. The main, secondary and third illumination mode contribute 43.0%, 31.6% and 25.3% to the total power spectrum respectively, indicating a large degree of incoherence, which is unexpected. Several factors could potentially contribute to the incoherence. Most commonly, the scattering from the X-ray optics installed in the beamline experiment [70]. Secondly, the diffraction pattern data were not corrected from the darkfield data. Without the help from extra probe modes, all those incoherent scattering factors can pose challenges on the reconstruction process.

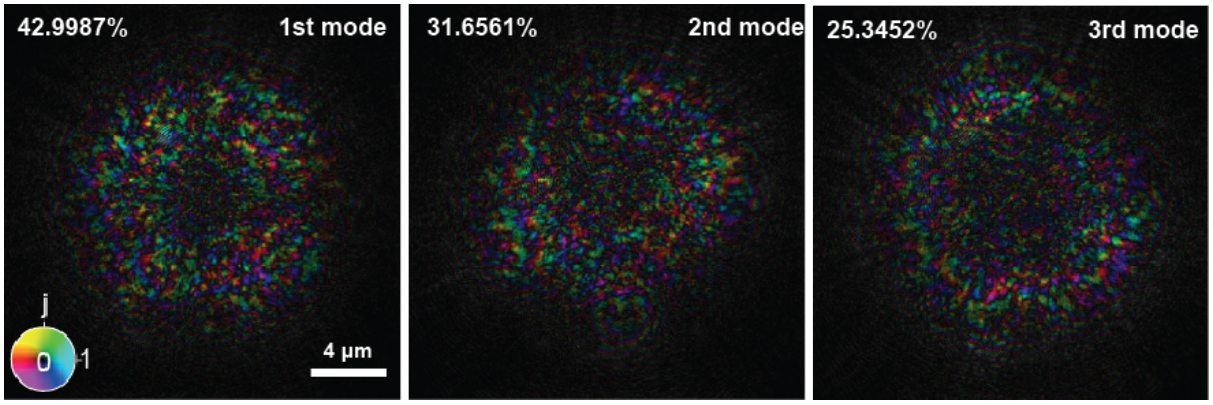

Figure 4.12. Three probe mode used for the ptychography reconstruction. From left to right the main probe mode, 2nd probe mode and 3rd probe mode are displayed.

To evaluate the DoF limit, the data set was fed into 3PIE algorithms with the reconstruction parameter (**Table 4**) and method indicated in previous sections. Given the sample thickness of approximately 1 mm, three sets of reconstructions (as shown in **Figure 4.13**) were conducted with evenly spread-out separation distance of **Figure 4.13(a)** 2×500 µm (3 slices), **Figure 4.13(b)** 3×333 µm (4 slices) and **Figure 4.13(c)** 4×250 µm (5 slices) separation. All reconstruction were completed with 500 iterations, however full convergence was reached usually after around 100 iterations. As shown in **Figure 4.13(a-b)**, a good degree of separation is evident between the reconstructed slices. Due to the random positions of the glass beads in the paraffin block, there are some features shared by the DoF between two adjacent slices in **Figure 4.13(b)**. With careful observation, some features still fell within the region set by the separation distance in the reconstruction, consequently appearing in only a single slice. In contrast, almost no features in **Figure 4.13(c)** show the presence in only a single slice. This observation indicates the T_{min} of around 350-500 µm.

Degrees of inconsistency in the separation ability is shown in this experiment, while some features separate successfully within the DoF range, some appear in multiple reconstructed slices. However, it is possible to set the separation distance much lower than the actual DoF, as shown in **Figure 4.13(c)**. As a result, each slice only shows the feature falls within the DoF range at the current slice position.

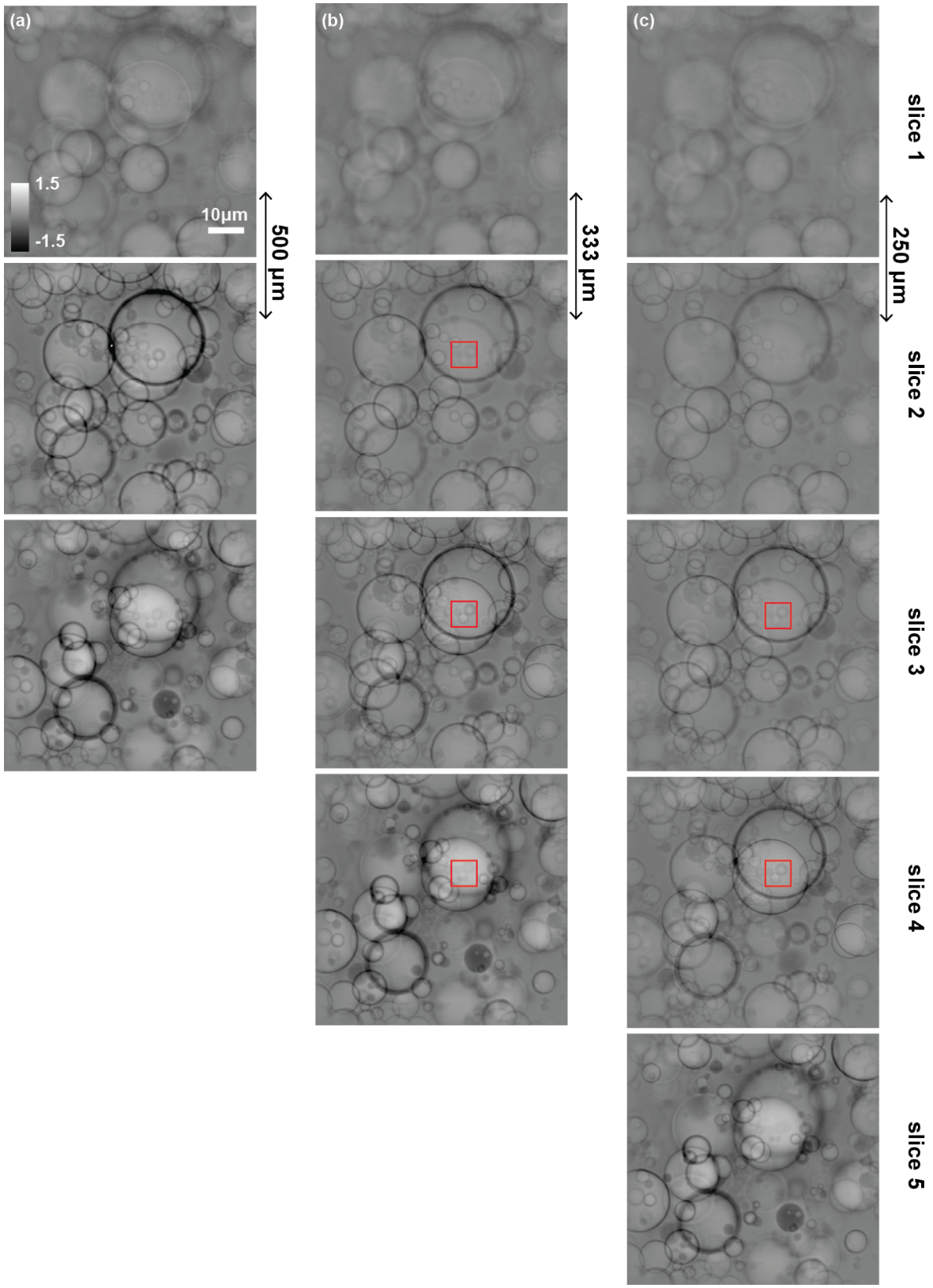

Figure 4.13. Reconstructed multi-slice phase images of 1mm thick paraffin mounted glass beads. (a) 3 slices were reconstructed with separation distance set to 500 µm, (b) 4 slices were reconstructed with separation distance set to 333 µm, (c) 5 slices were reconstructed with separation distance set to 250 µm.1

On initial inspection, the depth separation achieved in both results appear to contradict Eq. 3.2 and disagree with the literature on multi-slice ptychography in the conventional, far-field geometry. Indeed, for the results presented in the chapter the inter-slice separation can be set to zero, and the two slices still separate out the microspheres effectively. The cause of this apparent discrepancy is the geometric parallax of the cone beam: it is the way features in different axial locations move relative to one another as the sample scans that dictates the minimum distance between slices for which a degree of depth separation can be obtained. This minimum, T_{min}, is dependent on the change in geometric magnification between slices, as shown in **Figure 4.14**. In the Figure, due to parallax effect, the star feature, projected onto the plane of the square feature, moves a larger distance as the sample is scanned through the beam. In the extreme case where the star is scanned from one side of the beam to the other, its projection must move at least a resolution element further than the star in order that some depth information be encoded in the recorded data.

The minimum separation T_{min}, for which the recorded diffraction data contains a degree of depth information can be estimated from a geometric consideration of parallax. When the sample is translated by a distance D/M_{Tmin}, the star feature moves from one side of the beam to the other. Its projection onto slice 2 initially lines up with the square feature, but after the translation, the square has moved by the translation distance D/M_{Tmin} but the projected star has moved further, a distance D/M_0. The difference between these two distances is DT_{min}/z_0 and this must exceed the lateral resolution δr if the star and square are to be differentiated in depth. This leads to Eq. 4.1, where the star slice must be separated from the square slice by a distance:

$$T_{min} = \frac{z_{tot}\delta r}{D} \qquad (4.1)$$

Where D is the diameter of the detector (or of the cone disc if its entirety falls within the detector area), δ_r is the resolution, and z_{tot} is the distance from the cone beam apex to the detector. Note that this limit is governed by the convergence angle of the cone beam, which under the paraxial approximation is D/z_{tot}, and that it is independent of the wavelength. For the optical bench experiments Eq. 4.1 gives T_{min}=11 µm, and for both X-ray experiment configurations it gives T_{min} ≈ 100 µm and 50 µm, respectively. These figures are the smallest

possible slice separations for which some degree of depth information is encoded in the diffraction data. Eq. 3.2 is applicable only for the highest resolution features in the sample volume and is contingent on the sample being scanned across the entire beam diameter.

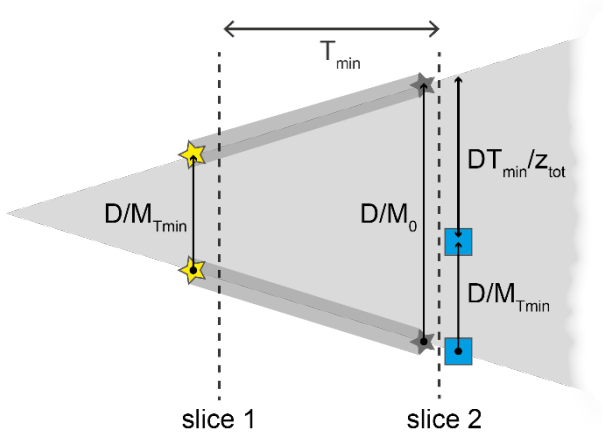

Figure 4.14. Demonstration of minimum separation set by geometric parallax effect of cone-beam NMP configuration.

In practice, depth separation appears to be some small multiple of the extreme limit in Eq. 3.2 and is likely sample- and setup-dependent due to the system NA, which is determined by the NA of the image system and the object NA from the sample, as demonstrated in Figure 3.1. For instance, the minimum slice separation is limited to ~0.5 mm at an image resolution of ~200 nm the near-field X-ray setup, around a factor of 5 above the limit set by Eq. 4.1. From the results, if the slice separation is lower than this threshold the multi-slice reconstruction does not provide significant benefit over single-slice, 2D imaging, whilst for samples thicker than this, resolution and DoF are improved by using the multi-slice method.

This chapter successfully demonstrated the implementation of X-ray NMP in synchrotron facility. First, it significantly extended the DoF, with multi-slice reconstructions resolving features in samples up to 2.5 mm thick—far exceeding the theoretical DoF limit of for just under 150 nm resolution.

Second, resolution trade-offs were explored across different experimental configurations. Depth separation was validated through experiments with both layered and continuous samples. In Experiment 1, which utilized an indirect detector, a resolution of 133 nm and depth resolution around 1 mm was achieved; however, the setup suffered from low flux and

limited illumination diversity. In contrast, Experiment 2, which employed a direct detector, improved the resolution to below 100 nm and depth resolution to approximately 100–400 μm by leveraging higher flux, beam geometry and optimised speckle illumination.

As well as demonstrating a good degree of depth sensitivity and extension of DoF, these experiments successfully demonstrated MNP over large fields of view using as few as 20 diffraction patterns – a considerable data saving over equivalent far-field ptychographic scans. Building on the recent demonstration of multi-slice ptycho-tomography at optical wavelengths [33], the work presented in this chapter shows the potential to realise the implementation of near-field multi-slice ptycho-tomography, aiming to increase accessible sample volume and reduce the huge data sets that are currently required.

5. Optical slicing via near-field multi-slice ptychography microscopy

As a tool for optical microscopy, ptychography has been implemented in myriad forms, including microscope add-ons, stand-alone systems and as a system-on- chip [12] [103] [104]. Unlike X-ray and electron ptychography, the key advantages of the method at optical wavelengths comes not from its lens-free operation but from the contrast enhancement offered by phase imaging and the ability, especially of Fourier ptychography, to extend an optical system's space-bandwidth product. In the work presented in this chapter, these benefits were combined with one of ptychography's other facets: accommodating multiple scatter and diffraction when imaging optically thick samples, via the multi-slice method [2]. The multi-slice method described in previous Chapters has been implemented as a microscope add-on, either in Fourier or conventional sample-scanning geometries, and has enabled computational optical sectioning, where the axial or z resolution of the slicing reduces to the micron scale [90] [91]. The approach proposed in this chapter continues this theme, enhancing a standard microscope through a combination of multi-slice and near-field ptychography (where interference patterns are recorded at Fresnel numbers $\gg 1$) [20] [74] [73] [105] to realise extended FoV for computational optical sectioning, free from the effects of multiple scattering and diffraction.

The aim of this work is to implement and optimise Near-field Multi-slice Ptychography Microscopy (NMPM) to enhance phase imaging in optical microscopy, enabling high-resolution, label-free computational optical sectioning with an extended depth of field (DoF). To achieve this, an optical NMPM system is developed and implemented by integrating NMP within an optical microscope to enhance phase imaging for thick samples. The experimental configuration is also optimised by systematically evaluating the effect of illumination modulation and further experimental parameters on reconstruction quality.

This chapter started with the motivation to further implement near-field multi-slice ptychography within an optical microscope. The experiment configuration for NMPM and

modification of 3PIE algorithm are then demonstrated, followed by three studies using this optical NMPM configuration.

The first study focuses on the optimisation of the illumination spatial frequency, where four diffraction pattern data sets were collected using illumination modulated by a range of speckle sizes. The reconstruction results are then compared and analysed systematically.

The second study investigates the step size influence on multi-slice reconstruction and the importance of the introduction of a second probe mode for the algorithm convergence.

In the final part, three sets of result are presented to demonstrate the NMPM method's capability to recover the phase image at a diffraction-limited resolution of around 1 µm and extend the DoF for samples ranging in thickness from 40 to 130 µm. In addition, the minimum number of diffraction patterns for multi-slice reconstruction was investigated aiding the reduction of computation requirement.

5.1. Experimental configuration

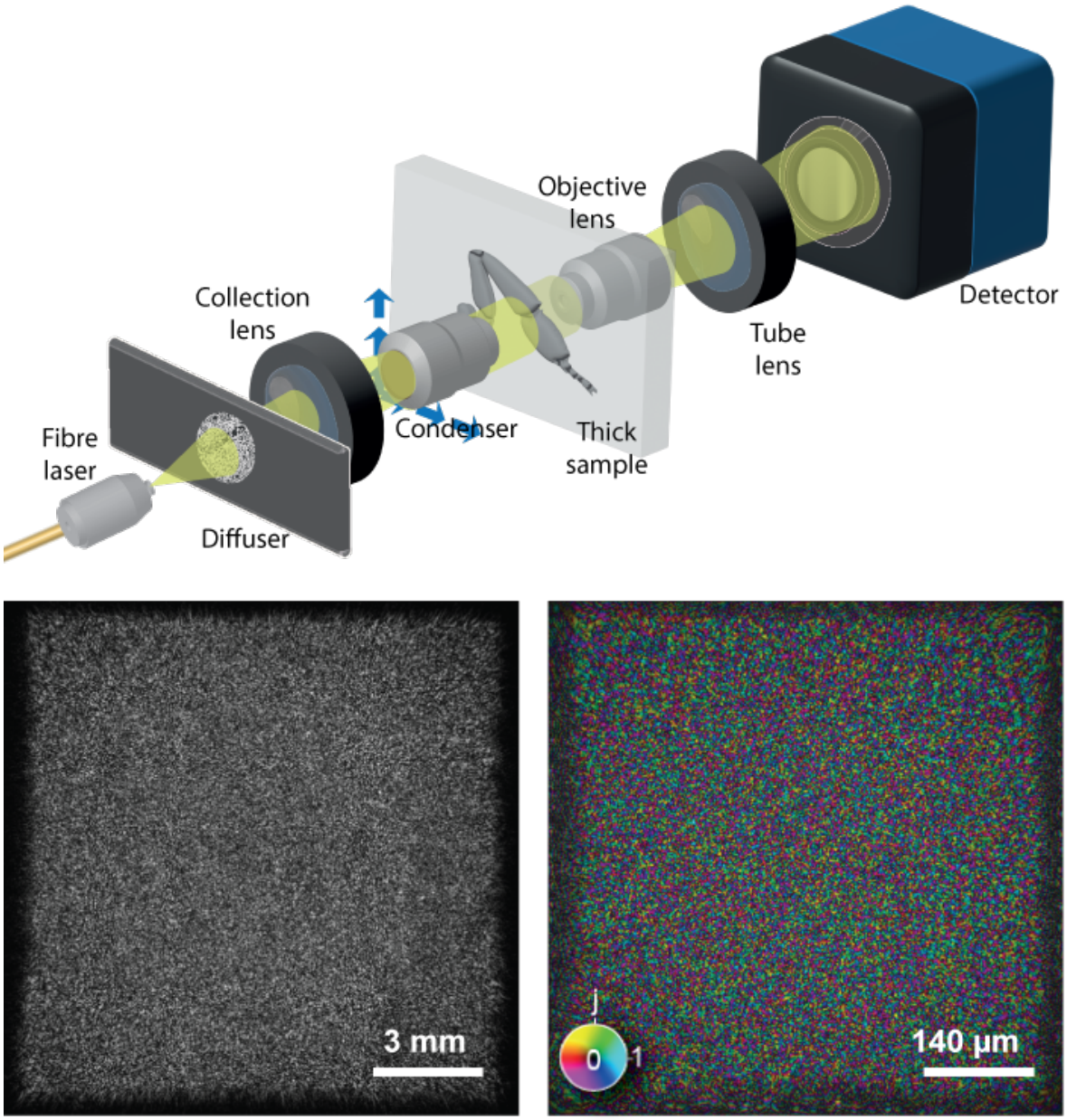

Figure 5.1: Top: optical experimental configuration for near-field multi-slice ptychography microscopy. Bottom left: example of a diffraction pattern collected in the experiment, with size of 1024×1024 pixels. Bottom right: example of recovered probe illumination.

The optical arrangement of the multi-slice microscope is shown at the top of **Figure 5.1**. A fibre-coupled diode laser of wavelength 675 nm first passes through a ground glass diffuser and a square aperture that limits the extent of the beam. The resulting structured

wavefront (an example of recovered probe illumination is shown in bottom right of **Figure 5.1**) was projected onto the sample through a condenser lens (NA = 0.4). The fibre tip and back focal plane of the condenser were conjugated, so that the wavefront between the condenser and objective lenses was formed into a collimated pencil beam. The most down-beam plane of the sample was initially positioned at the image plane of a standard compound microscope comprising a 20×, NA = 0.5 objective and f = 180 mm tube lens with the measured magnification of 20.27×. For the data collection process, the sample was then axially offset in the up-beam direction by 25 μm from the image plane. This results in near-field diffraction patterns imaged onto the CCD detector, a PCO edge 4.2 with a pixel pitch of 6.5 μm. Ignoring lens aberrations, the combination of the microscope and the detector can be seen as a virtual detector positioned 25 μm from the sample, with a demagnified pixel pitch of 0.325 μm. The diffuser can be moved along the optic axis to change the speckle size of the measured interference patterns; **Figure 5.1** bottom left shows a typical diffraction pattern with a speckle size in this range. Each diffraction pattern comprises an average of 16 frames, each exposed for 200 μs and corrected by subtraction of a darkfield reference. The diffraction pattern data were binned by a factor of 2, to 1024×1024 pixels, resulting in an effective pixel size for the reconstructed images of 0.64 μm. A full ptychographic data set was collected from the microscope by recording a series of between 100 - 400 of these diffraction patterns as the sample was laterally translated through a Fermat spiral pattern of scan positions, with a 25 μm step between each position [80].

The lateral resolution set by the system is approximately $1.1\ \mu\mathrm{m}$, suggesting a DoF for the system in of $1.8 - 9.3\ \mu\mathrm{m}$ defined by Eq. 3.2 Conventional (non multi-slice) ptychography results in image reconstructions showing considerable out-of-focus diffraction artefacts for samples beyond the upper end of this thickness, and for samples well beyond this limit multiple scattering causes convergence failure of the reconstruction algorithms.

5.2. Improvement of the reconstruction algorithm

The recorded diffraction data are reconstructed via the 3PIE algorithm [2], adapted for near-field operation as described in Section 2.9.2, by replacing the final far-field (FFT) propagation from sample to detector with an angular spectrum propagator. Different from the work

presented in Chapter 2 and 3, as the illumination beam was collimated in the experiment, no extra geometrical adjustment was required. However, In the work, several further modifications are also introduced for the most optimal reconstruction result:

1. Tikhonov regularisation was implemented for the slice update. The original 3PIE algorithm suffered from the limitation caused by the weakly constrained low spatial frequency as iteration progresses [91] [1], where the low spatial frequency artefacts appear if the slice separation is set to a small value – typically smaller than the DoF defined by Eq. 3.2.

2. Because the beam must be back-propagated sequentially through the slices of the multi-slice object, the down-beam slices, which are addressed first, are preferentially updated, and features located at up-beam slices can take a considerable amount of iteration to emerge. Consequently, the update rate is tapered when the number of slices is large – typically more than 10 slices.

3. Due to the complexity of the highly speckled illumination probe, two coherent probe modes were implemented to model the illumination wavefront [70], which significantly boosted the convergence speed. However, the coherence was not an issue for the fibre coupled laser illumination source. An example of the two coherent modes is shown in **Figure 5.2**. An example shown the evolution of the probe recovery over 2000 iteration in **Figure 5.3**. It takes more than 2000 iterations for the probe just start to converge using only one probe mode with MSE of 0.0713, whereas the employment of two probe modes results in an accurate and fully converged probe estimation and reach MSE of 0.0313 in less than 250 iterations. This shows the method with two probe modes achieves a significantly better convergence rate and improved accuracy, as evidenced by the lower MSE. The MSE obtained using two probe modes is approximately 56% lower than that from the single-mode reconstruction, and this result is achieved with only one-tenth of the iteration count, clearly demonstrating a substantial advantage in both convergence speed and reconstruction accuracy.

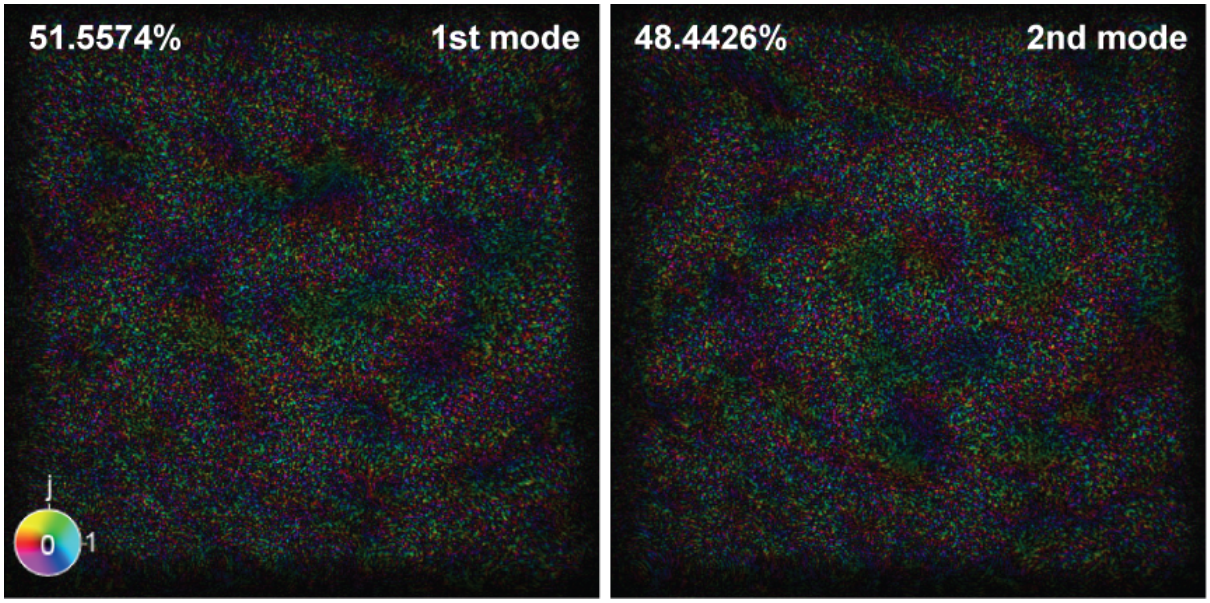

Figure 5.2. Example of two coherent probe modes. Left: the main probe mode; right: secondary probe mode.

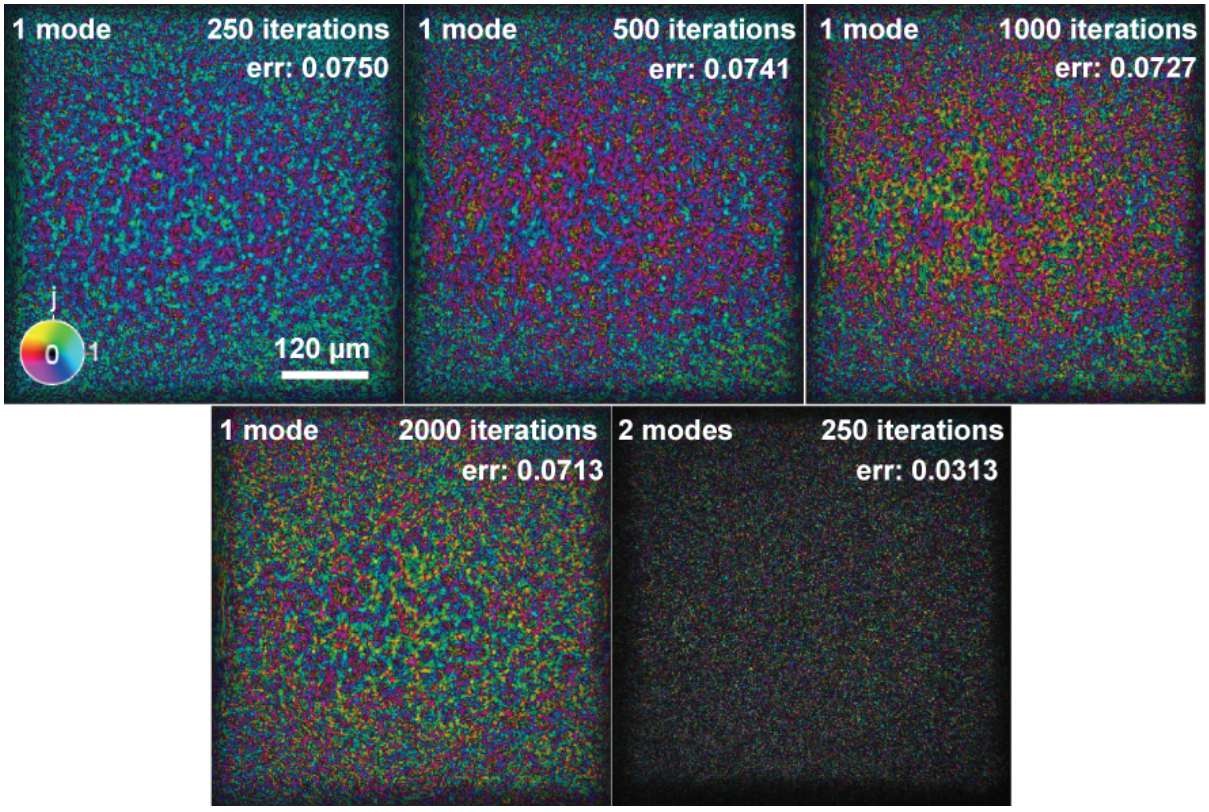

Figure 5.3: The probe estimation over 2000 iteration using a single probe mode and the full probe convergency with two probe modes with 250 iterations.

Alongside the modifications mentioned above, all the multi-slice results shown in this chapter were conducted using a two-step reconstruction strategy when the number of reconstruction slice was set to more than 10. First an accurate model of the illumination wavefront was recovered using 250 iterations of the modified 3PIE, with 5 slices evenly spaced through the sample volume. Then the number of slices was increased to any desired amount before running a further 250 iterations.

The modified version of 3PIE algorithm and example dataset are shown in **Code 2** and **Dataset 2**.

5.3. Optimisation of illumination frequency spectrum

In near-field ptychography, the resolution is primarily determined by the NA of the imaging system. However, resolution can be improved by employing a highly spatial-frequency-diverse illumination [106][107]. From the definition of the projection approximation, the formation of the diffraction patterns, or the intensity measurement in ptychography data are determined by the scattering power of the object itself and the frequency spectrum of the illumination. Since the scatter power of the sample is usually fixed, the illumination becomes a more viable strategy to enhance the diversity of the intensity measurement.

In conventional ptychography, the far-field measurements are naturally highly diverse due to the pinhole illumination, which offers a wide range of spatial frequency information [108] [49]. However, this is not the case for near-field ptychography. As explained in Section 2.8 [20] [74] [97], the diversity in the diffraction pattern data relies heavily on the illumination spectrum, which is determined by the combination of the illumination NA and the spatial frequency spectrum of the speckle modulation introduced by the diffuser.

Traditionally, scotch tape was commonly used as a choice of diffuser for near-field ptychography in an optical setup [61] [75]. However, high-resolution information is often missing from the reconstructed phase images, because of the limited frequency spectrum of the scotch tape diffuser. Ideally, the projection of the diffuser speckle size needs to be small enough to fully occupy illumination frequency NA, while the speckles also need to be large enough to be resolved by the NA of the virtual detector.

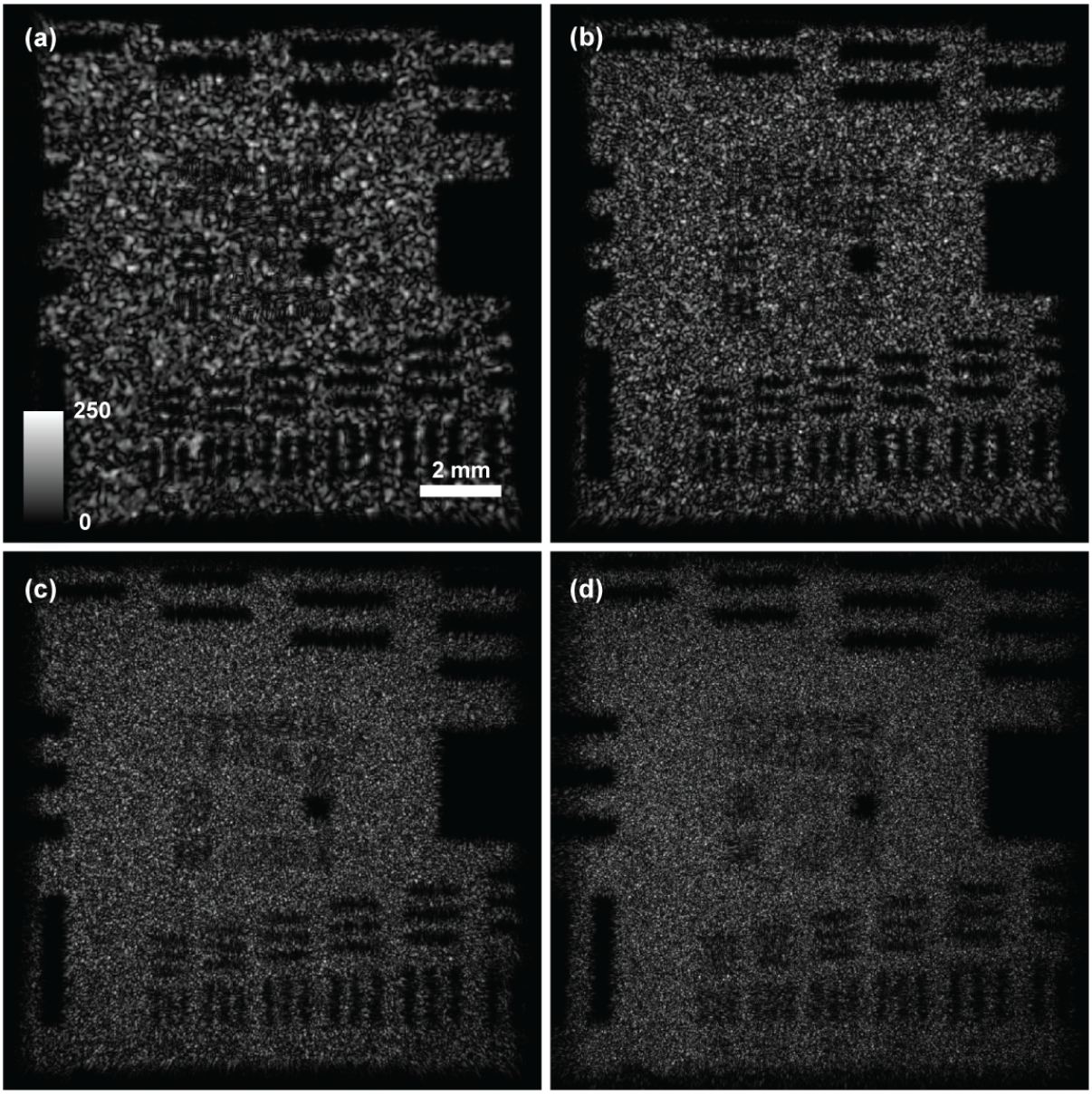

Figure 5.4. Diffraction patterns collected with a range of speckle sizes from (a) largest to (d) smallest. The colour bar indicates the root-squared value of the recorded intensity.

To demonstrate the role of the illumination spatial frequency content in the NMPM system, four sets of 400 diffraction patterns of a 1951 USAF resolution target (as shown in **Figure 5.4**) were collected, with gradually decreased speckle sizes, to assess their impact on the reconstruction effectiveness. The step size for the data collection was fixed at 25 µm (equivalent to approximately 90% line-overlap). **Figure 5.4** presents examples of the collected diffraction patterns: in order from (a) to (d) the average speckle sizes are approximately 20-30 pixels, 10-20 pixels, 5-10 pixels and 2-5 pixels. All the 2D reconstruction

were performed using 250 iterations of the 3PIE algorithm, but with only one slice enabled. The reconstruction results are shown in **Figure 5.5**, where (a-d) corresponds to the diffraction patterns shown in **Figure 5.4**. The top row shows the reconstructed amplitude images of the resolution target, with the zoomed-in views of group 8 and 9 in the second row. The third row shows the recovered probe illumination, whereas the frequency spectrums corresponding to the central region of those probes (cropped to 800 × 800, so that not affected by the distorted edge) are shown in the bottom row. The spatial frequencies indicated in the bottom row from left to right are approximately 3.9×10^5/m 5.9×10^5/m, 7.0×10^5/m and 7.8×10^5/m.

As expected, a much more evenly distributed frequency spectrums and spread across the entire illumination NA are shown in **Figure 5.5(c)** and **(d).** Whereas the cut-off frequency corresponds to the illumination shown in (a) and (b) almost halved and most distributed across the centre, which is approximately a third of the illumination NA frequency spectrum.

All the reconstructed images indicate that the smallest set of bars in group 8 of the pattern can be clearly resolved, corresponding to a lateral resolution of $\delta_{lateral} = 1.1\ \mu\mathrm{m}$.

Despite the results shown in **Figure 5.5(c)** and **(d)** seems to have the most optimal frequency spectrum, the reconstruction result from the smallest speckle unexpectedly shows slight blur and reduced contrast. There are several factors that potentially contribute to this discrepancy: Firstly, the slit was not aligned perfectly to the back image plane formed by the collection lens and condenser, which led unwanted scattering and aberration. Secondly, the environmental instability caused the vibration of the system. The employment of small speckles which requires high system stability. In addition, the choice of step size has significant influence on the resolution, which is investigated in the following section. However, further work is required to evaluate the cause of the blurring.

Overall, the speckle size shown in **Figure 5.5(c)**, around 3-10 pixels holds a good compromise between some degree of relaxation of the experiment condition and the speckles employ here being highly random and containing high spatial frequencies to fully utilise the illumination NA. This ensures rapid evolution of the illumination field along the propagation direction, which allows the recovery of clean sample slices at minimal axial separation.

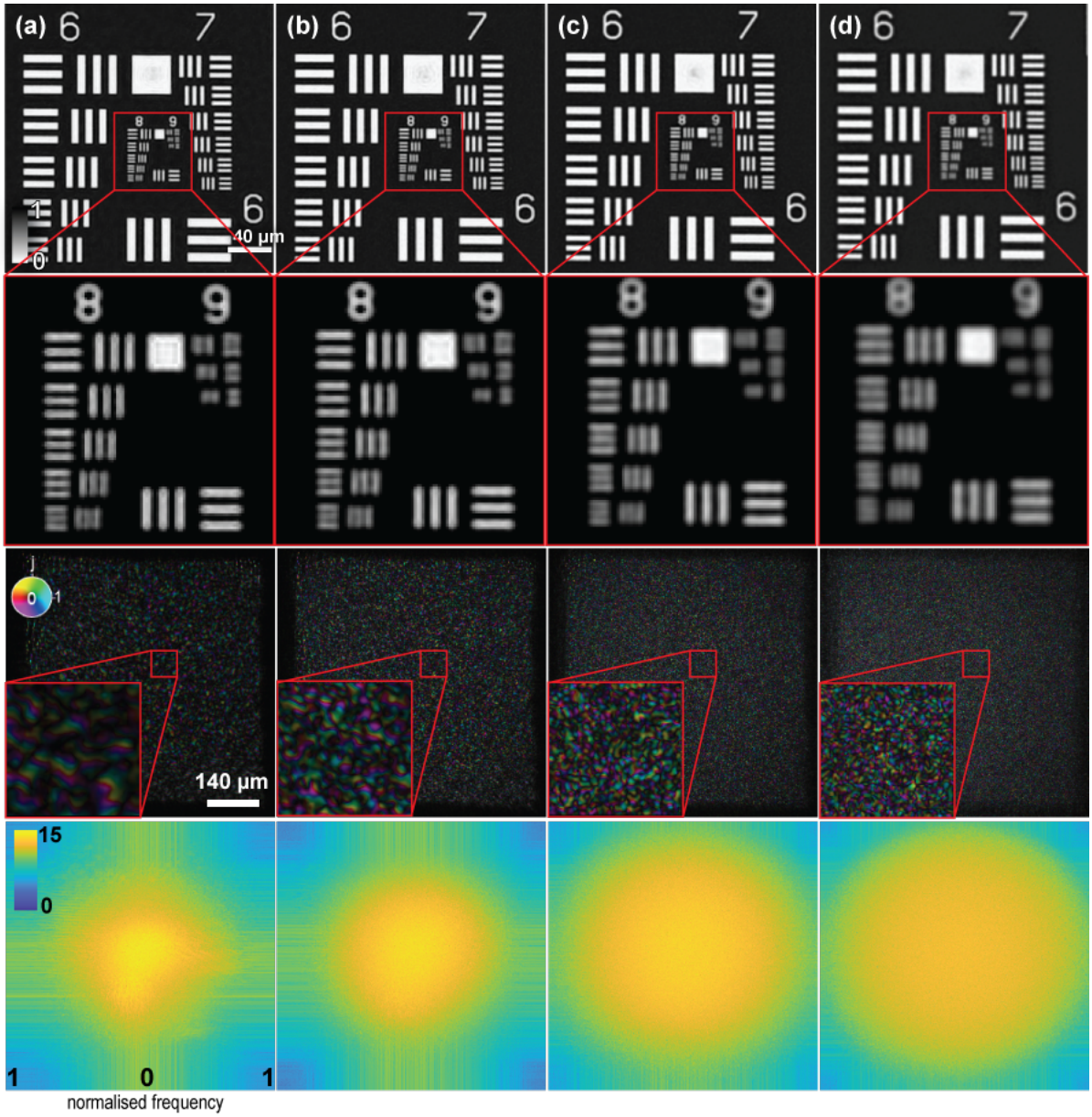

Figure 5.5. 2D reconstruction result for a resolution target with different speckle grain size from (a) largest to (d) smallest. First Row: recovered modulus of the resolution target. Second row: zoom-in view of group 8 and 9. Third row: recovered illumination probe. Bottom row: the corresponding frequency spectrum of the illumination probe. The maximum spatial frequency in the bottom row is 7.8×10^5/m.

5.4. Step size influence on NMPM

From the experiences of conventional ptychography experiments and most of the simulation work, a step size equivalent to 70-80% overlap is typically considered as the most optimal scanning step [83]. This balance ensures sufficient redundant information while maintaining the high diversity of the diffraction pattern data. However, this is not the case for near-field ptychography, especially with the extra diffuser modulation. R. Clare has previously suggested that the step size for near-field ptychography experiment should be chosen depending on the characteristic of the diffuser, with the most optimal value ranged between 4 – 20 times of the speckle size [74]. Based on the solution from Clare's work, the step size influence is then investigated for multi-slice reconstruction using the most optimal illumination from the last experiment, which has an average speckle size of is approximated 3- 10 µm, shown in **Figure 5.5(c)**.

A comprehensive survey was conducted by collecting four sets of 100 diffraction patterns with step sizes of 66 (90% overlap), 25, 8 and 4 (99% overlap) µm using a whole aphid sample with a thickness of around 130 µm. In total, 26 slices with separation distance of 5.2 µm were reconstructed using the reconstruction strategy described previously. The reconstruction results of three selected slices are shown in **Figure 5.6** (Slice 1 is the most up-beam slice and slice 26 is the most down-beam slice; the step size decreases from top row to bottom row). The corresponding zoomed-in views are shown in **Figure 5.7**. From the initial inspection on **Figure 5.6**, all four sets of data achieved high resolution reconstruction results, apart from slightly decreasing FoV at a small step size.

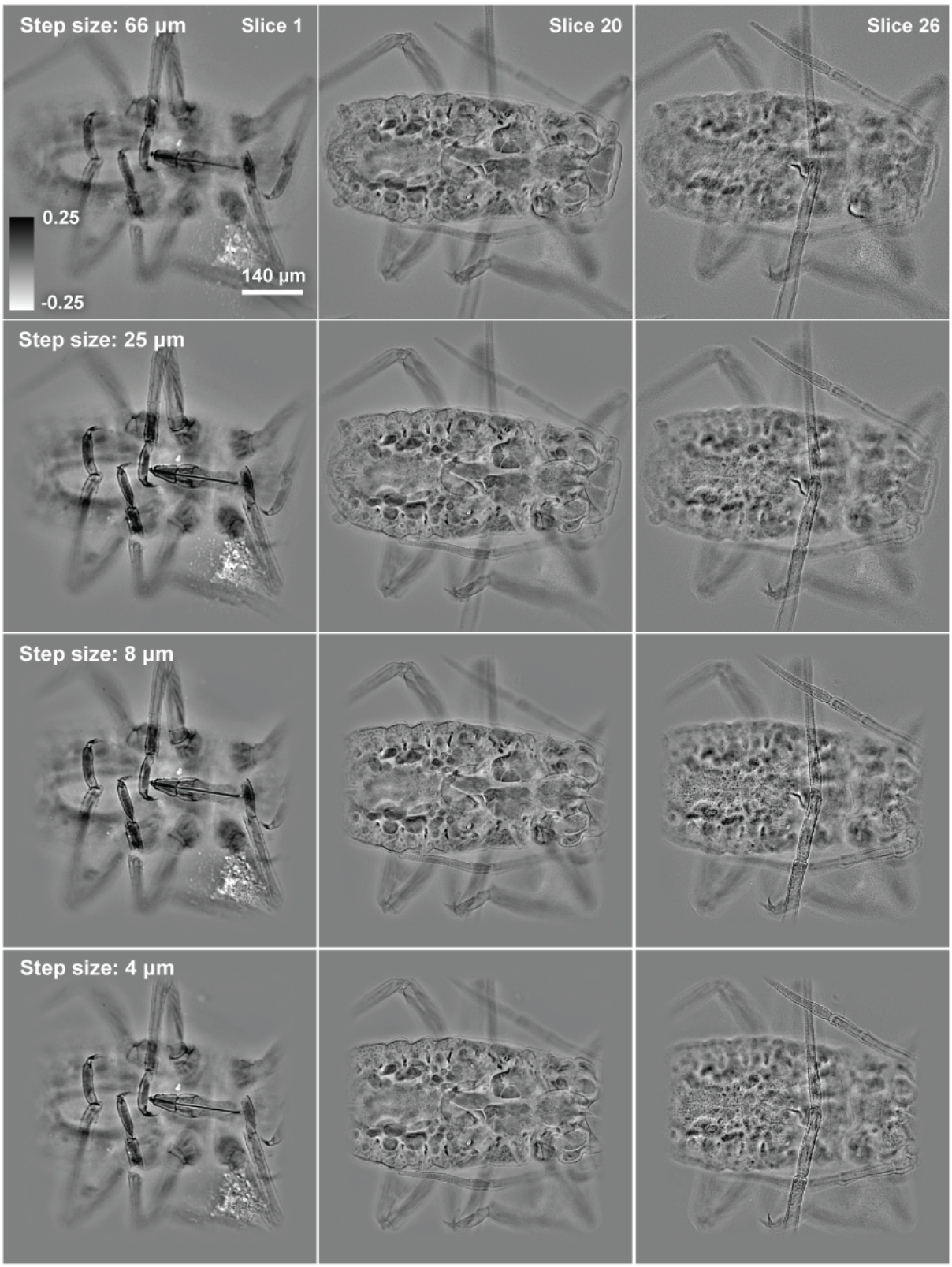

Figure 5.6. Reconstructed phase images using multi-slice method with step size of 66 µm (top row), 25 µm (2nd row), 8 µm (3rd row) and 4 µm (bottom row).

However, the corresponding zoom-in view in **Figure 5.7** reveals that as the step size decreases from 66 µm to 8 µm, both image resolution and phase contrast improves. When the step size is relatively large in comparison to the average speckle size, 66 µm in the case, the high frequency features cannot be recovered or are blurred. This effect is particularly severe and can be easily observed in slice 26s, as the “dot” features were missing from the reconstruction. When the step size is reduced to 25 µm, these features begin to emerge, and the phase standard deviation increases to 0.062 over the central region, indicating greater contrast. A further reduction to 8 µm improves SNR, reducing the standard deviation to 0.059 and recovering finer structures. At 4 µm, however, a slight decline in contrast occurs, with the standard deviation decreasing to 0.048, likely due to increased redundancy and averaging effects. In this case, the subtle drop in SD combined with better feature recovery suggests that noise was reduced without loss of meaningful contrast, which is ideal.

Additionally, the MSE after 100 iterations for step sizes of 4 µm, 8 µm, and 25 µm are 0.0233, 0.0236, and 0.0279, respectively, showing a ~16.5% improvement in reconstruction error when decreasing from 25 µm to 8 µm, and a further minor gain at 4 µm. While smaller steps yield better feature recovery, the diminishing returns and slight loss of contrast at 4 µm suggest an optimal trade-off around 8 µm. This is further supported by more uniform illumination sampling and improved frequency coverage in the reconstruction. In this case, a relatively small step size close to the speckle size shows great improvement on the recovery of high frequency features and increases the signal-to-noise ratio, thereby the resolution for each slice reconstruction is improved. However, further investigation is required to optimise and evaluate the relationship between the ptychographic step sampling condition and illumination frequency spectrum. In addition, there is no direct indication showing that the separation ability and depth resolution were affected by changing the step size.

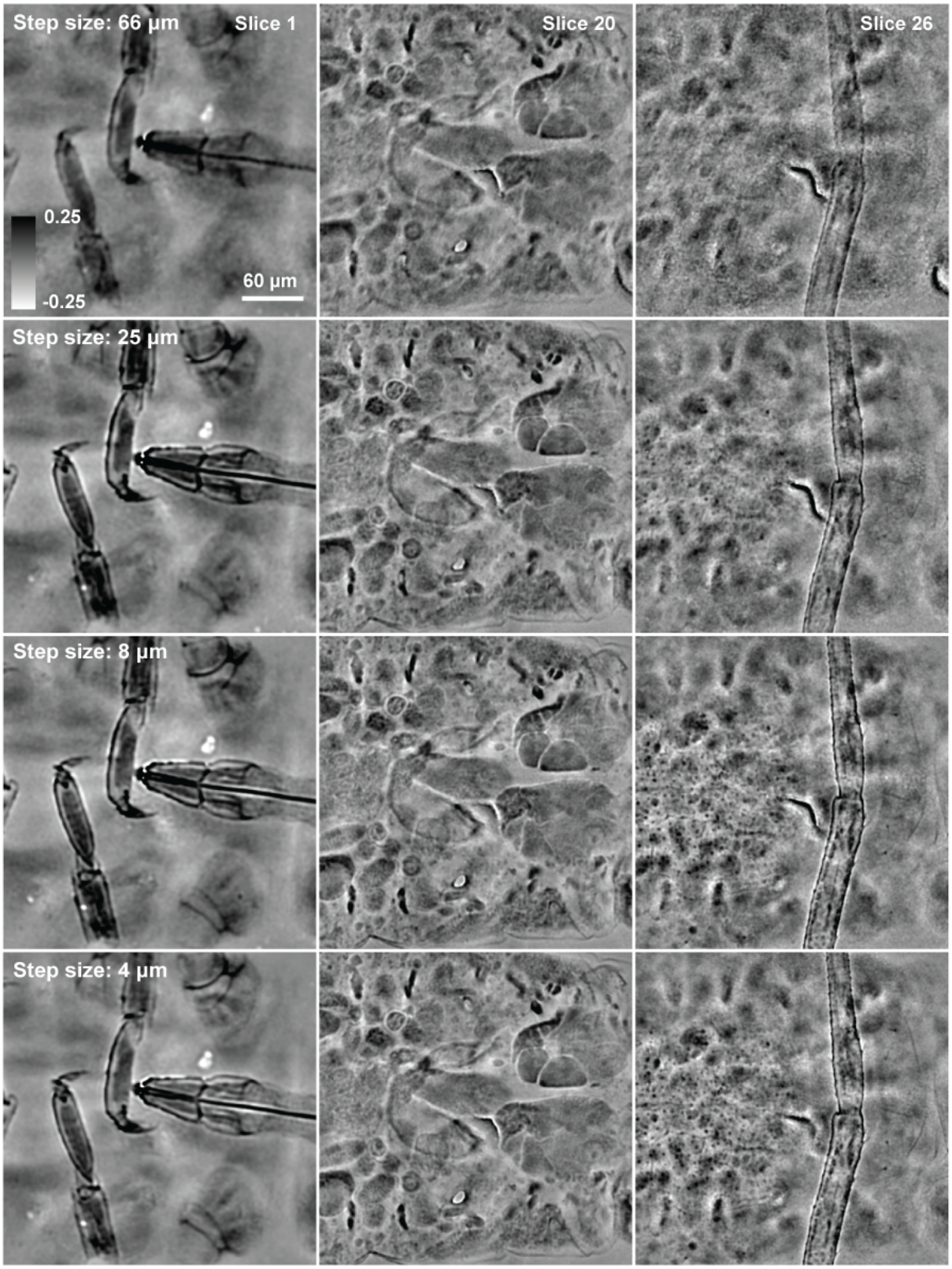

Figure 5.7. The zoomed-in view corresponding to the reconstructed phase images in Figure 5.6.

5.5. Further testing on various samples

With the optimised configuration and experiment set up, the versatility of NMPM method is now demonstrated using three different biological samples which show a range of phase variation and structure complexity: Lilium pollen grains, an algae colony and a whole aphid. All the data comprised 400 diffraction patterns and were collected using the illumination shown in **Figure 5.6(c)** with the step size of 25 µm, which gives a good comprise between high resolution and large FoV.

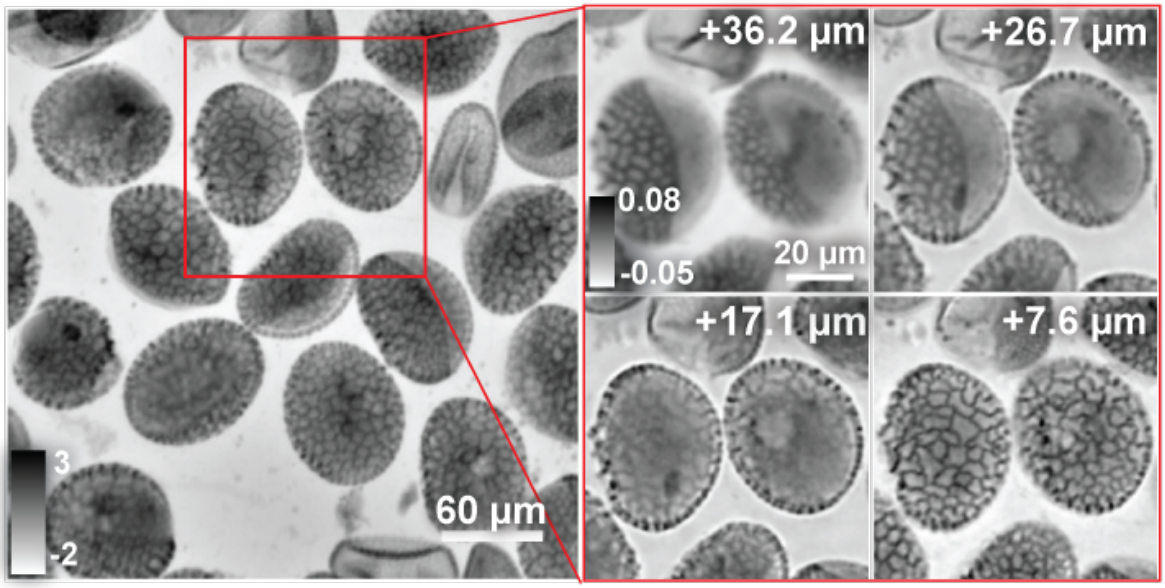

Figure 5.8. Reconstructed phase images of lilium pollen grains, computationally sectioned using multi-slice ptychography. Left: pixel-wise product of all 43 reconstructed slice phases. Right: examples of individual slices at the indicated depths through the sample volume.

The lilium pollen grains were approximately 40 µm thick – exceeding the optical system's DoF by a factor of at least 4. The grains were pre-stained and mounted on a standard microscope slide beneath a 200 µm coverslip. Following the data collection and reconstruction procedure as described in Section 5.2, 43 slices spaced 0.95 µm apart were reconstructed. **Figure 5.8** shows the recovered projected phase of the full sample volume on the left: this is obtained by summing the phases of the individual slices. Examples of four reconstructed slices are shown on the right, corresponding to positions within the sample volume at 7.6 µm, 17.1 µm, 26.7 µm, and 36.2 µm (the most down-beam plane of the

sample is positioned at 0 µm). A movie of all 43 slices is shown in **Media 1**, and the sample volume is rendered in 3D in **Media 2**. The multi-slice reconstruction boosted the possibility to identify structural detail within individual slices that is not apparent in the 2D projection, including the cell wall, tube nucleus, pollen wall, and aperture.

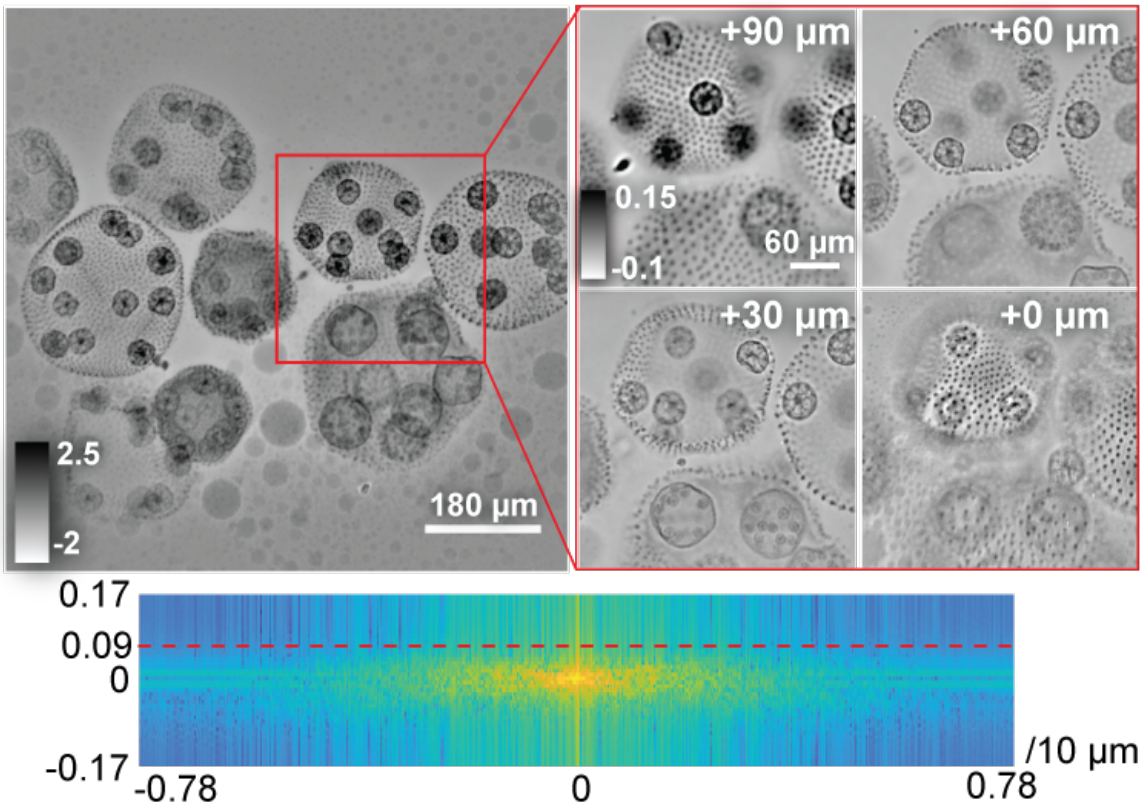

Figure 5.9. Reconstructed phase images of a volvox, computationally sectioned using multi-slice ptychography. Top left: pixel-wise product of all 41 reconstructed slices. Top right: examples of individual slices at the indicated depths through the sample volume. Bottom: 3D-FFT of the full reconstructed image stack, the red dotted line indicates the cut-off frequency of approximately $0.09 \times 10^6 /m$, corresponding to the axial resolution of 11.1 µm.

A second sample, a volvox colony approximately 90 µm thick and mounted in the same way to the previous sample, produced the reconstruction shown in **Figure 5.9**. The reconstruction was performed using the same two-step strategy, finishing with 41 slices, spaced 2.25 µm apart. To the top left, the phases of all 41 slices are added to produce a single projection through the sample. Examples of individual slices through the volvox are

shown to the top right of the main figure at the indicated range of depths through the sample volume. A movie showing the reconstruction of all slices can be viewed in **Media 3**.

The DoF achieved in the reconstruction is at least 10 times the DoF of the microscope objective and the projection remains free from diffraction and multiple-scattering artefacts, leaving only blurring due to the missing wedge of low spatial frequencies as shown in **Figure 5.9**. The plot represents the project of 3D-FFT spectrum from z-direction, where the horizontal axis and the vertical axis corresponds to the lateral spatial frequency and the z-frequency of the full reconstructed sample volume.

In a final test the whole aphid sample, which had an approximate thickness of 130 µm, at least 13 times the DoF set by the imaging system, was imaged again. The exoskeleton structure and the soft tissue of this sample exhibit very different optical densities, which can be particularly challenging for conventional light microscopy: standard brightfield microscope images, collected from the same optical setup (The same objective lens and the matching condenser NA was used to take the light microscopy images and the DoF for is estimated at approximately 5 µm) at a range of defocii, are shown in the top row of **Figure 5.10**, and clearly demonstrate the difficulty posed by background light and diffraction when attempting to clearly resolve features at different depths through this thick sample. Multi-slice reconstruction of 44 individual slices separated by approximately 3 µm produced the zoomed-in phase images shown in the middle row of **Figure 5.10** at the same depth locations (120.9 µm, 74.4 µm and 27.9 µm), showing the evolution of the aphid reproductive system over the change in depth, with the bottom row showing the full reconstruction FoV. High-resolution visualisation of both the internal and external structures of the aphid are made clear across a significant depth range here, well beyond the limits of the conventional microscope. Furthermore, the phase information obtained at different depths provides much better contrast and richer structural detail. The complete reconstruction of all 44 slices is shown in **Media 4.**

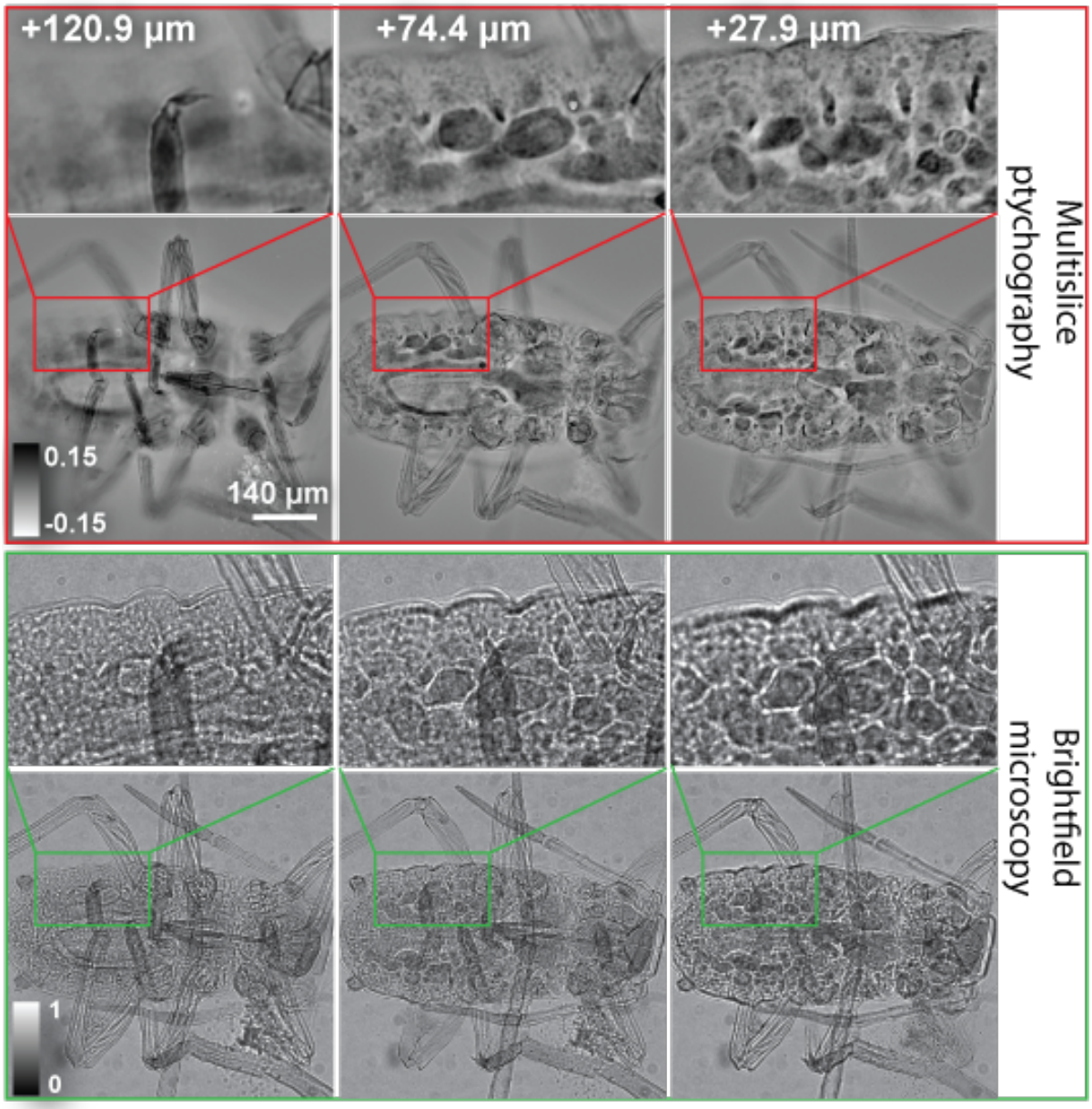

Figure 5.10. Reconstructed slices of a whole aphid through the full sample volume. The highlighted boxes show a zoomed-in view of the reproductive organs. A series of images taken using a compound light microscope at the same depth and cropped to the same region for comparison.

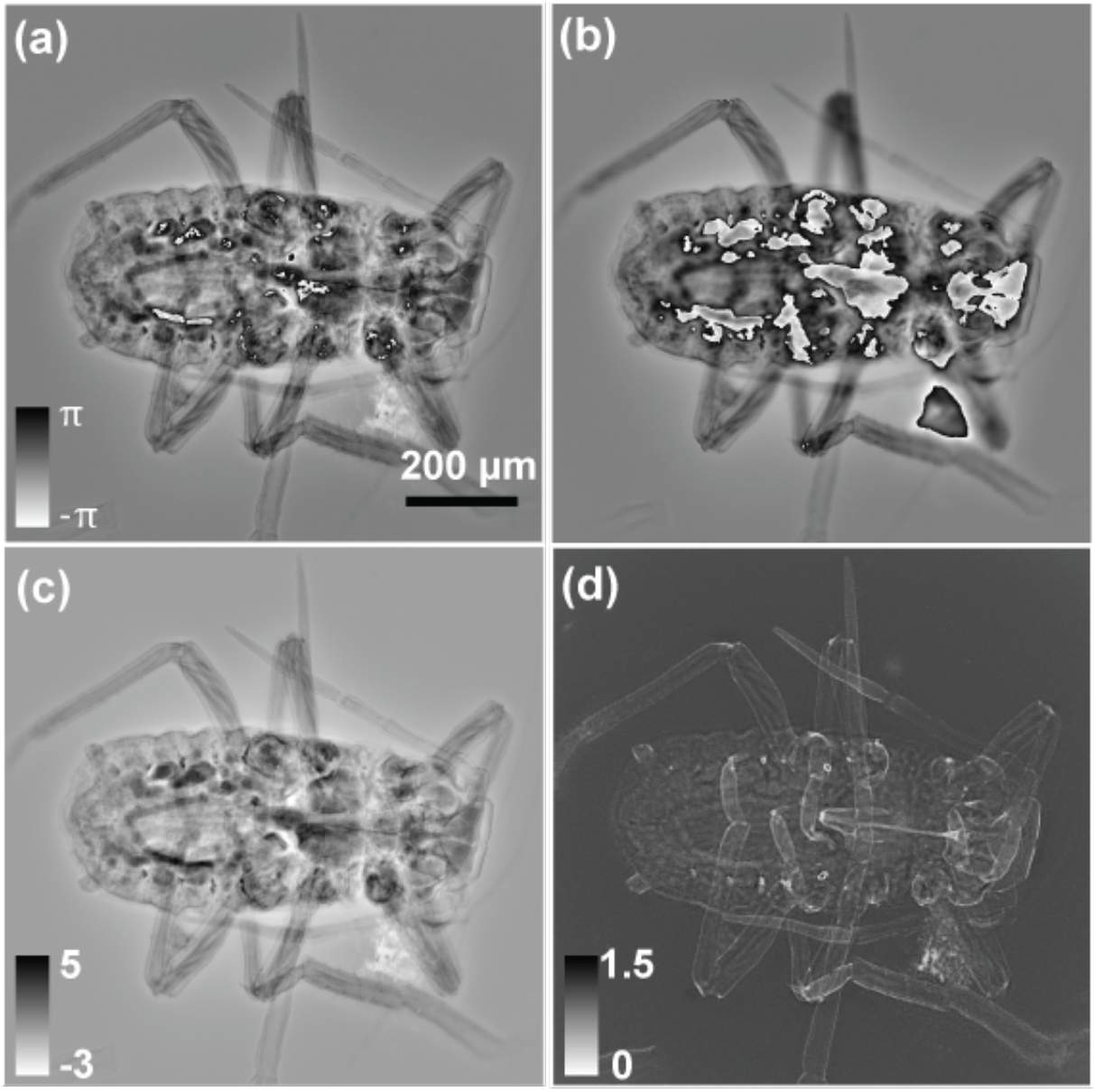

Figure 5.11. Comparison between multi-slice reconstruction and 2D reconstruction. (a): pixel-wise sum of the phase image from multi-slice reconstruction. (b): 2D reconstruction. (c) unwrapped image of multi-slice reconstruction shown in (a). (d): modulus of the pixel-wise added multi-slice reconstruction.

The result from multi-slice reconstruction were then compared to a 2D ptychographic reconstruction using the same dataset, further highlighting the capacity of the multi-slice approach to extend DoF. **Figure 5.11(a)** presents the pixel-wise sum of all 44 reconstructed slices, covering a full FoV of approximately 1.5 mm^2. By performing multi-slice reconstruction, all the fine features are revealed with high resolution across the full sample

volume. In contrast, the 2D reconstruction (**Figure 5.11(b)**) exhibits significant out-of-focus blur artefact limiting the observable features and details within the sample. Both images in (a) and (b) are presented with wrapped phase to facilitate a more direct visual comparison. Furthermore, **Figure 5.11(c)** shows the unwrapped phase of the multi-slice result, while (d) shows the corresponding recovered modulus. However, the 2D reconstruction result shown in (b) cannot be unwrapped due to the presence of phase vortex artefacts, which arise from the violation of 2D projection approximation condition.

5.6. Reducing the data requirements

Data collection and reconstruction times are a potential drawback for multi-slice ptychography and are in general the most significant weakness in the ptychographic method. The results where 400 diffraction patterns were collected, took, in total, around 600 seconds for data collection and 8283 seconds to run through the reconstruction process. To reduce these times, the effect of collecting fewer diffraction patterns on the multi-slice reconstruction is now investigated. **Figure 5.12**. displays the 33rd slice out of 44 slices, showing the aphid embryo and reproductive organ, reconstructed using (a): 100, (b): 50, (c): 25, and (d): 16 diffraction patterns. The smaller data sets were created simply by discarding the outer parts of the spiral scan pattern whilst maintaining the same step size. Both data collection and reconstruction times fall linearly with the number of diffraction patterns, so that the data set containing 100 patterns took 150 seconds to collect and 993 seconds to reconstruct.

Notably, with 50-100 diffraction patterns (**Figure 5.12(a,b)**), the aphid embryo's reproductive organ remains clearly visible, and lateral and axial resolution are comparable to the reconstruction using 400 patterns. A further reduction to 25 diffraction patterns (**Figure 5.12(c)**) results in significantly lower signal-to-noise ratio, thereby obscuring fine details, but most features remain recognisable. When the number of total diffraction patterns is reduced to 16 (**Figure 5.12(d)**), the reconstruction fails. **Media 5** provides a comparison of reconstructions with reduced diffraction pattern number, further illustrating the decrease in phase contrast, especially in upstream slices, as the number of patterns is reduced.

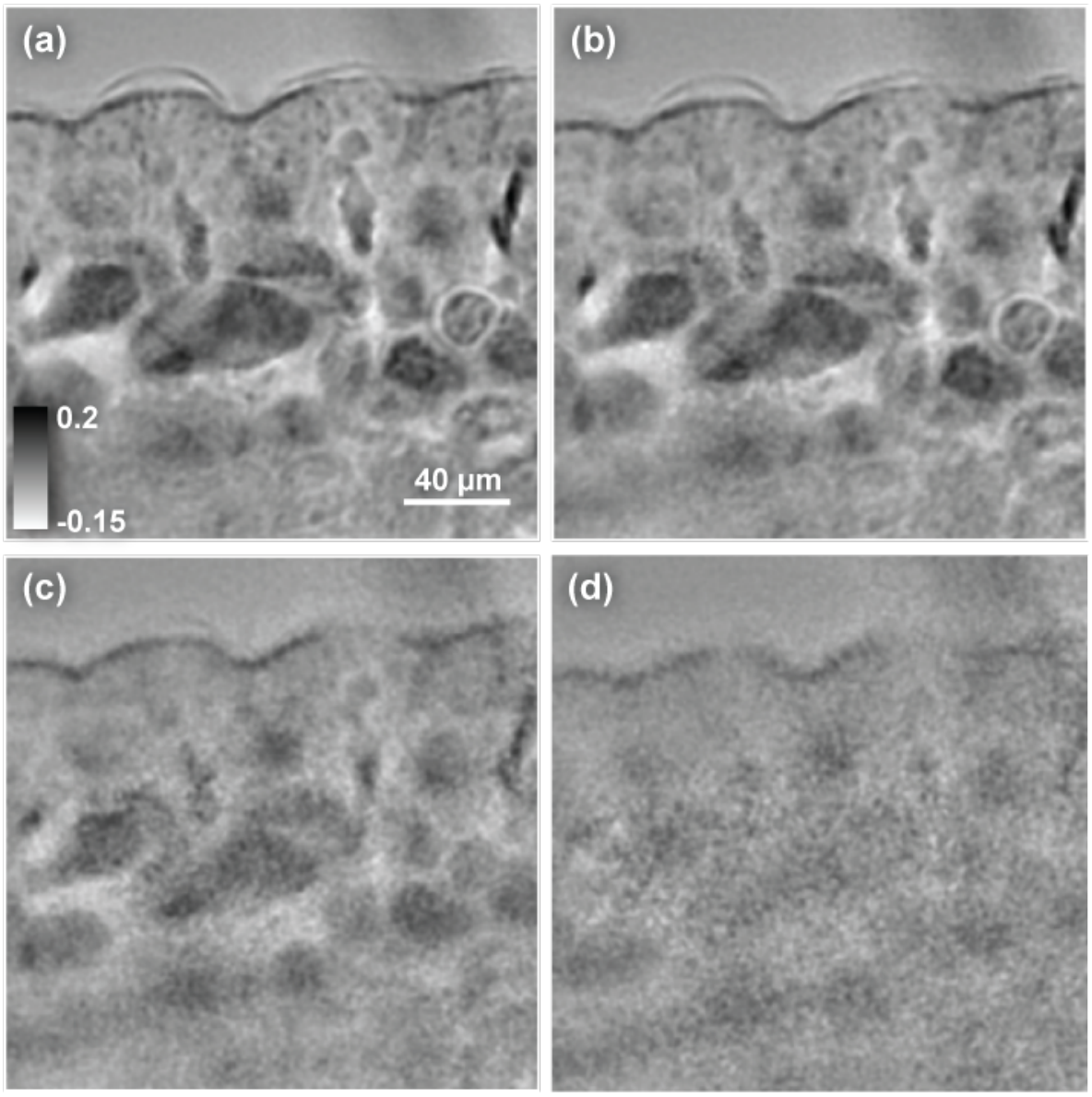

Figure 5.12. A selected slice from multi-slice reconstructions of the aphid sample, using fewer diffraction patterns. (a) 100 diffraction patterns; (b) 50 diffraction patterns; (c) 25 diffraction patterns; (d) 16 diffraction patterns.

5.7. Implementation with large NA objective

Further advantage of the NMPM method including the use of a straightforward and easily calibrated optical setup with a fixed optical path during data acquisition, which can be adapted easily to meet various resolution requirements, for both lateral and depth-wise, through the adjustment of the numerical aperture of the condenser and objective lenses.

A further experiment implemented with high NA objectives is demonstrated using the Lilium pollen grains sample. The experiment configuration remains mostly the same as shown in **Figure 5.1**, with the exception that both the condenser and objective lenses from the previous setup were replaced by 40x, 0.75 NA objectives, which resulted in an effective pixel size of 0.325 µm. The theoretical DoF for this configuration ranged between approximately 1 - 4.3 µm, determined by Eq. 3.2. In addition, the camera length was reduced to the 10 µm. The data collection process followed the same procedure as described in the previous experiments, where 400 diffraction patterns were collected using a Fermat spiral scan with step size of 10 µm.

The reconstruction strategy outlined in Section 5.2 was then applied, where 71 slices with axial step of 0.5 µm were recovered. **Figure 5.13** shows a series of selected reconstructed phase image of Lilum pollen grains, with the complete reconstruction stack available in **Media 6.** Several key aspects of the reconstruction are shown in **Figure 5.14**: The top left image presents the frequency spectrum of the centre slice, revealing a cut-off frequency of approximately $1.3 \times 10^6/\mathrm{m}$, which corresponds to a lateral resolution of around 750 µm. The top right image shows the recovered probe illumination, which has an average speckle size of 1-2 µm; And the bottom image provides an orthogonal view (from z direction) of 3D-FFT for the full image stack. The “donut” shaped 3D-FFT indicates a cut-off frequency of $0.3 \times 10^6/\mathrm{m}$ at z-direction, corresponding to the DoF of approximately 3.3 µm. Whereas, the depth resolution using 20x objective configuration was measure at approximately 10 -15 µm, as determined from the 3D-FFT plot shown in **Figure 5.9**.

The reconstruction results clearly show that both lateral and depth resolution are significantly improved with the implementation of high NA objectives (40×). However, despite these enhancement in resolution, the reconstruction result still suffers from the heavy shadowing and blurring artefact in the adjacent reconstruction planes. Again, those artefacts are attributed to the missing wedge of the low-frequency information in the 3D-FFT spectrum shown in **Figure 5.14**. The recovery and separation of those low frequency information require further investigation.

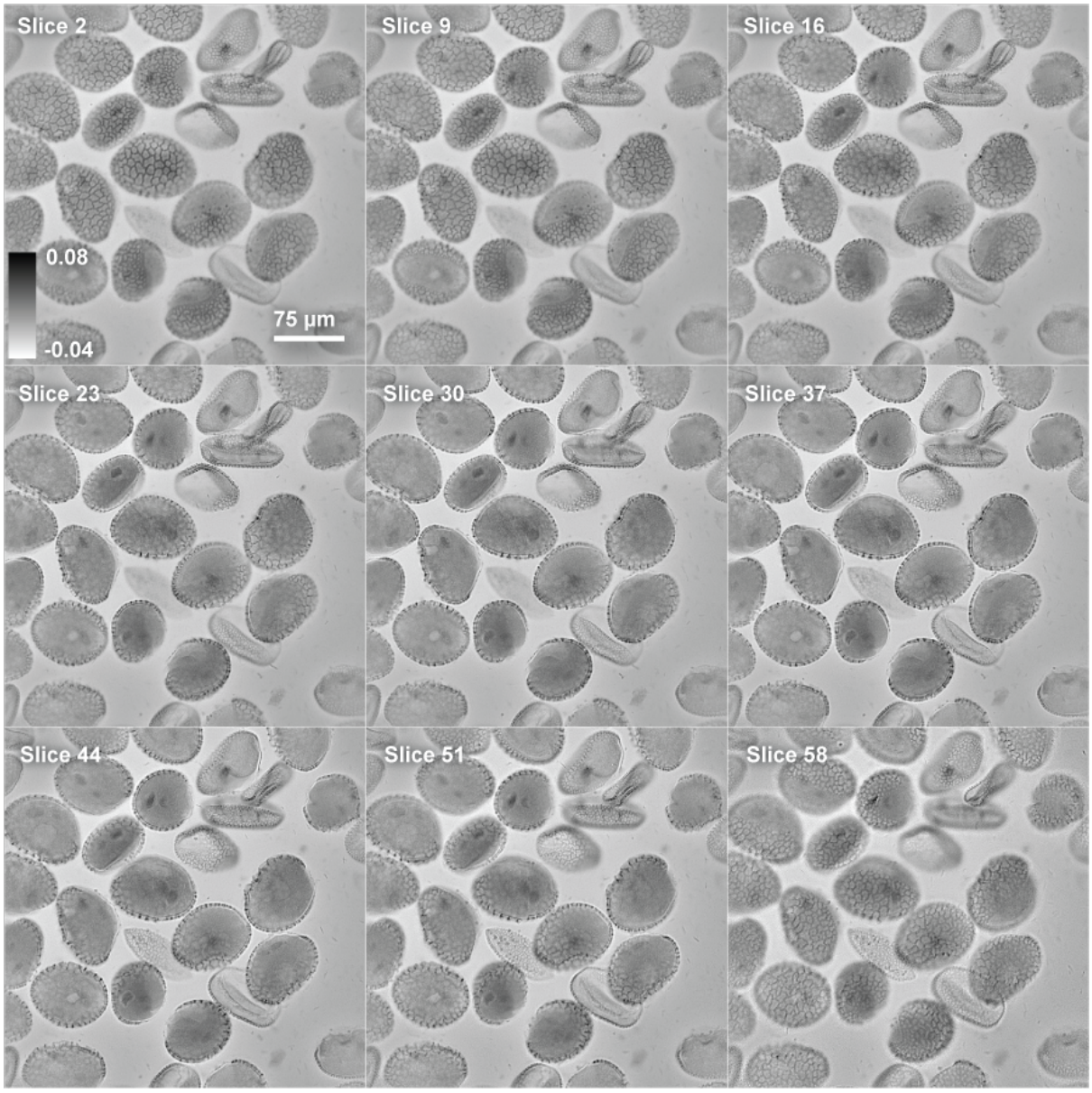

Figure 5.13. Multi-slice reconstruction results of Lilium pollen grains with 40x, 0.75 NA objectives.

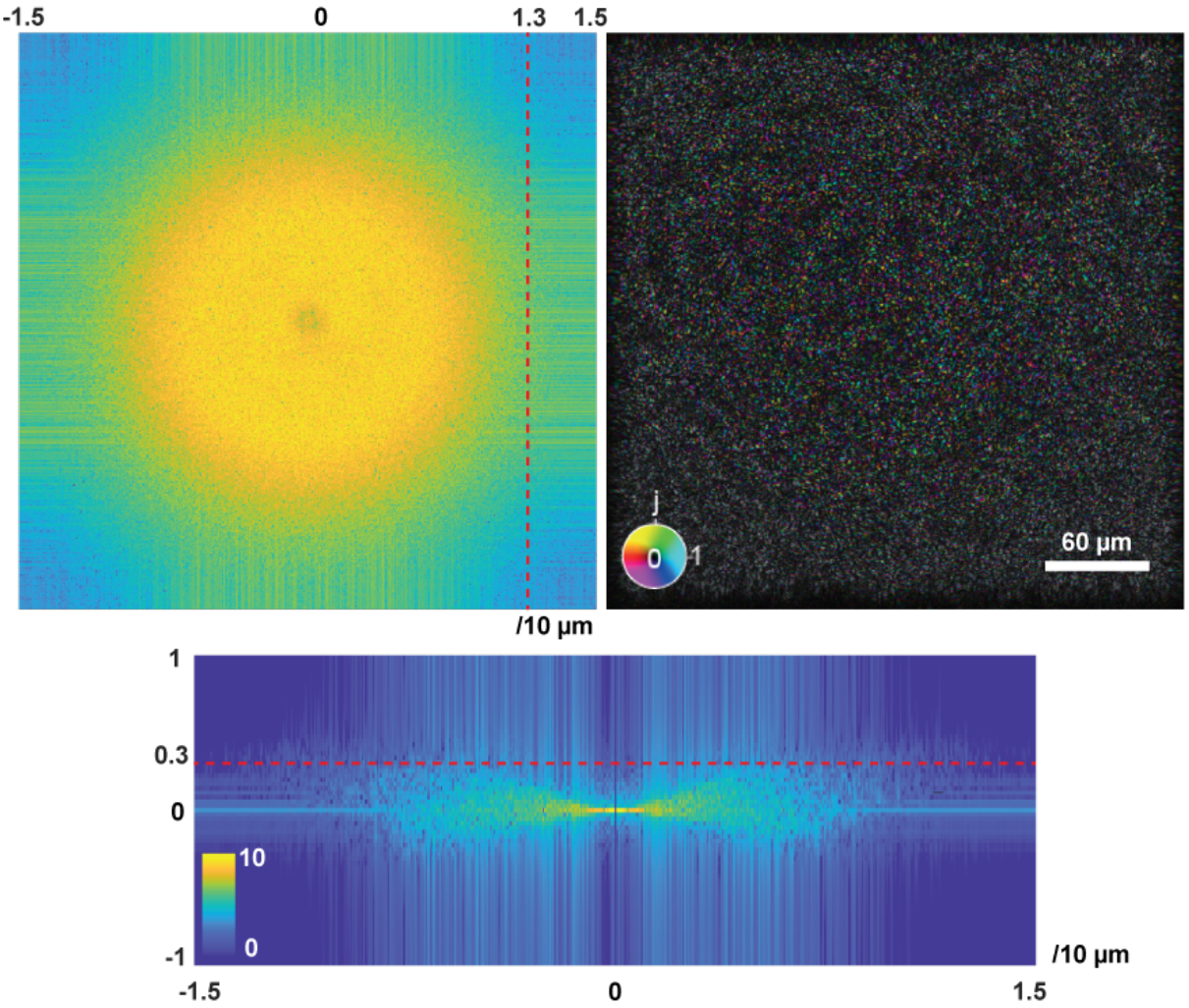

Figure 5.14. Top left: the frequency spectrum of the most centre slice of the reconstruction; Top right: the recovered probe illumination; Bottom: the orthogonal view of 3D-FFT for the full image stack.

In this work, the reconstruction results for computational sectioning of thick biological samples via multi-slice near-field ptychography were demonstrated, incorporating speckle-modulated illumination on a standard microscope platform. The reconstruction results achieved axial resolution below 10 µm over 40 computationally recovered slices at a lateral resolution of 1 µm with 20× microscope, while the 71 slices were recovered at lateral resolution of 750 nm and depth resolution of 3.3 µm using 40× microscope. The microscope implementation of NMP allows detailed visualisation of complex structures of biological samples across a significant depth. Notably, the near-field implementation of multi-slice ptychography requires significantly less data to cover a large FoV than the far-field and

Fourier ptychography configuration [90] [91] – typically fewer than 100 diffraction patterns are required to complete high quality NMP reconstruction. In far-field multi-slice ptychography, the illumination is typically constrained by a small pinhole to ensure spatial coherence and controlled diffraction. A small illumination area limits the sample region probed in each scan position, meaning that a large number of diffraction patterns are essential to cover a reasonable FoV. Increasing the illumination size via optics (e.g., a larger pinhole or lens-based expansion) in conventional ptychography could improve coverage per scan position, but it will lead to reduction of resulting spatial resolution due to the trade-off between spot size and numerical aperture. On the other hand, the ability of the NMPM to clearly address the depth of the sample with large FoV and maintain high resolution in this work strongly suggests the potential of the imaging method for revealing the 3D morphology of large-volume biological specimens. Unlike conventional 2D ptychography methods, which are constrained by their limited DoF and susceptibility to artifacts, multi-slice model can overcome these limitations, offering a more comprehensive and accurate representation of those optically-thick samples.

Conclusion and future work

In this thesis, the implementations and optimisation for near-field multi-slice ptychography using X-ray and visible radiation source were presented. This proof-of-principle work revealed the unique capability of extending sample volume in both lateral and z-direction by implement multi-slice ptychography in a near-field regime. These initial results pave the way for further applications in biological sciences aiming at imaging large volume samples. Additionally, several important experiment parameters were revisited and further optimised specifically for NMP, such as illumination spatial frequency spectrum, step size and minimum requirement for the number of diffraction patterns. Finally, serval modifications of 3PIE algorithm were introduced for enhance the overall performance and quality of the reconstruction, especially the implementation of additional probe modes, even where the illumination can be considered coherent, was shown to significantly accelerate the initial convergence and thereby reduced computational time.

In the first result chapter an alternative equivalent geometrical model for cone-beam illumination NMP was demonstrated, followed by the implementation and modification of the 3PIE algorithm. A lensless optical configuration for NMP was then designed to simulate the experimental geometry for the cone-beam X-ray setup and to evaluate the performance of the modified 3PIE algorithm. The successful multi-slice reconstruction was demonstrated through two sets of results - a two-layered testing sample and six 35 µm thick slices from a bee's leg sample with total thickness of around 200 µm.

The second result chapter presented two experimental works for NMP using hard X-ray (10 keV) radiation source. The first proof-of-principle experiment achieved a lateral resolution of 150 nm and extended the DoF for a continuous sample up to 2.5 mm thick with the separation limit of 0.5 mm to 1 mm. However, due to the inefficient X-ray optics and indirection detector, the limited resolution achieved resulted in poor depth resolution. In the second X-ray NMP experiment, alongside the higher geometrical magnification, a direct detector was implemented, and the illumination was modulated by a sandpaper diffuser which had a much broader spatial frequency spectrum. As a result, the available count for

the diffraction pattern data was improved by a factor of 5-10 and the lateral resolution was improved to sub 100 nm while the depth resolution was improved to 300 µm.

The final chapter reported the implementation of NMP with an external optical microscope system. The chapter emphasised the importance of a diverse illumination frequency spectrum and matching of the step size with the frequency spectrum range to improve the resolution in both 2D and 3D near-field ptychography. Furthermore, the robustness and versatility of NMPM was shown using a wide range of transmissive biological sample, extending the DoF by over 10-15 times at NA resolution (for both spatial and depth resolution) with as few as 50 diffraction patterns.

The future work is mainly aimed at three prospects: 1. The resolution improvement, both laterally and in depth. 2. The combining NMP with tomography – near-field diffractive multi-slice ptycho-tomography. 3. Investigating sample preparation and the implementation with different wavelength for X-ray NMP.

Starting with the resolution improvement with the NMPM, the most direct forward method is to implement a higher NA microscope system with a matching illumination spatial frequency spectrum as mentioned in Chapter 5. Another possibility is to realise super-resolution for near-field multi-slice ptychography microscopy by joint modulated illumination and detection, so that the illumination has an enriched frequency spectrum, and the NA limitation set by the objective lens can be surpassed. Additionally, when compared with far-field and Fourier multi-slice ptychography, the separation of the low spatial frequency components in the NMP reconstruction is relatively poor, which need to be further investigated.

One of the main limitations of conventional ptycho-tomography is the restriction of DoF for each projection angle [14]. Similarly to other imaging techniques, the higher the resolution is, the thinner sample needs to be. However, by incorporating the multi-slice model, combining near-field multi-slice ptychography with tomography [97] [109], the DoF for reconstruction from each projection can be extended, leveraging the naturally large FoV of near-field ptychography. This approach could theoretically increase the sample size by at least factors of ten without the requirement for extra data.

As mentioned previously the major limitation of the hard X-ray NMP is that, the depth resolution achieved is disappointing, even with the lateral resolution at sub 100 nm region, the depth resolution is only limited to 300 μm, which means the sample is required to be sufficiently thick. Even though the idea of slicing a 1 mm sample can be tempting, but in reality, the high radiation dose and the risk of radiation damage posed for those thick biological samples needs also to be considered. In addition, the sample preparation requires further investigation for the hard X-ray NMP. At this X-ray energy regime, heavy metal staining methods are usually required to enhance the contrast of certain biological structures. For a thick sample, this staining technique can be particularly challenging, due to the high absorption of the staining material. On the other hand, without staining, the structures will appear to be “clusters” like and become undistinguishable in the reconstruction, due to the similar refractive indices of those structures in the hard X-ray regime. Alternatively, soft X-ray perhaps is a more promising application for NMP. The combination of longer wavelength and high-resolution of soft X-ray regime offer a much better balance between the lateral and depth resolution according to Eq. 2.3. and has the potential to push the separation limit of NMP method to micron or even sub-micron region, therefore even with limited penetration power of soft X-ray, the DoF can still be extended by a factor of 2-5. Furthermore, the other advantage of soft X-ray is to generate contrast for those biological tissues without the need in staining.

This thesis, the introduction of multi-slice ptychography implementation in the near-field regime completes the trilogy of multi-slice ptychography, alongside far-field and Fourier multi-slice ptychography. NMP method offers distinct advantages over the other two multi-slice implementations, including the ability to extend both FoV and DoF for imaging large sample volume, reduced computational power requirement, and more relaxed experimental condition.

The optical implementation of NMP demonstrates significant potential to be applied to a wide range of biological samples, positioning it as a promising alternative to other existing optical slicing microscopy techniques to achieve high-resolution, label-free phase imaging. However, in order to fully realise the potential of NMP in the context of X-ray application, further exploration is required. While the current work provides a solid foundation for X-ray NMP, future investigations should focus on extending the method's application to the soft X-

ray wavelength regime which could effectively enhance the technique's effectiveness for large volume bio-imaging, especially when combined with ptycho-tomography.

Appendix I

Hu, Ziyang; Maiden, Andrew; Zhang, Yiqian; Li, Peng; Batey, Darren (2023). Near-field Multislice Ptychography. The University of Sheffield. Dataset. https://doi.org/10.15131/shef.data.21830094

Code 1: 3PIE algorithm for near-field cone-beam configuration

Dataset 1: Example datasets for Chapter 3 and 4

Hu, Ziyang; Maiden, Andrew (2024). modified 3PIE algorithm for near-field multi-slice ptychography. The University of Sheffield. Software. https://doi.org/10.15131/shef.data.25773630

Code 2: Modified 3PIE algorithm for near-field multi-slice ptychography

Hu, Ziyang (2024). Dataset for near-field multi-slice ptychography. The University of Sheffield. Dataset. https://doi.org/10.15131/shef.data.25833298

Dataset 2: Example datasets for Chapter 5

Appendix II

Hu, Ziyang (2024). Near-field Multi-slice Ptychography: Chapter 5: Multi-slice reconstruction. The University of Sheffield. https://doi.org/10.15131/shef.data.25416685

Media 1: Near-field multi-slice ptychography reconstruction of Lilium pollen grains with 400 diffraction patterns

Media 2: visualisation of 3D rendering of lily pollen

Media 3: Near-field multi-slice ptychography reconstruction of volvox colony with 400 diffraction patterns

Media 4: Near-field multi-slice ptychography reconstruction of a whole aphid with 400 diffraction patterns

Media 5: Near-field multi-slice ptychography reconstruction of a whole aphid with 100, 50 and 25 diffraction patterns

Media 6: Near-field multi-slice ptychography reconstruction of Lilium pollen grains with 400 diffraction patterns and 40x objective

References

[1] Z. Chen *et al.*, "Electron ptychography achieves atomic-resolution limits set by lattice vibrations," *Science,* vol. 372, no. 6544, pp. 826-831, 2021, doi: doi:10.1126/science.abg2533.

[2] A. M. Maiden, M. J. Humphry, and J. M. Rodenburg, "Ptychographic transmission microscopy in three dimensions using a multi-slice approach," *J. Opt. Soc. Am. A,* vol. 29, no. 8, pp. 1606-1614, 2012/08/01 2012, doi: 10.1364/JOSAA.29.001606.

[3] L. Tian and L. Waller, "3D intensity and phase imaging from light field measurements in an LED array microscope," *Optica,* vol. 2, no. 2, pp. 104-111, 2015/02/20 2015, doi: 10.1364/OPTICA.2.000104.

[4] A. Suzuki *et al.*, "High-Resolution Multislice X-Ray Ptychography of Extended Thick Objects," *Physical Review Letters,* vol. 112, no. 5, p. 053903, 02/04/ 2014, doi: 10.1103/PhysRevLett.112.053903.

[5] D. Gabor, "A New Microscopic Principle," *Nature,* vol. 161, pp. 777-778, 1948, doi: https://doi.org/10.1038/161777a0.

[6] D. Gabor, "Holography, 1948-1971," *Science,* vol. 177, no. 4046, pp. 299-313, 1972, doi: doi:10.1126/science.177.4046.299.

[7] D. Sayre, "Prospects for long-wavelength X-ray microscopy and diffraction," 1980.

[8] J. Miao, P. Charalambous, J. Kirz, and D. Sayre, "Extending the methodology of X-ray crystallography to allow imaging of micrometre-sized non-crystalline specimens," *Nature,* vol. 400, no. 6742, pp. 342-344, 1999/07/01 1999, doi: 10.1038/22498.

[9] H. M. L. Faulkner and J. M. Rodenburg, "Movable Aperture Lensless Transmission Microscopy: A Novel Phase Retrieval Algorithm," *Physical Review Letters,* vol. 93, no. 2, p. 023903, 07/09/ 2004, doi: 10.1103/PhysRevLett.93.023903.

[10] J. M. Rodenburg *et al.*, "Hard-X-Ray Lensless Imaging of Extended Objects," *Physical Review Letters,* vol. 98, no. 3, p. 034801, 01/18/ 2007, doi: 10.1103/PhysRevLett.98.034801.

[11] J. Rodenburg and A. Maiden, "Ptychography," in *Springer Handbook of Microscopy*, P. W. Hawkes and J. C. H. Spence Eds. Cham: Springer International Publishing, 2019, pp. 819-904.

[12] T. Wang *et al.*, "Optical ptychography for biomedical imaging: recent progress and future directions [Invited]," *Biomed. Opt. Express,* vol. 14, no. 2, pp. 489-532, 2023/02/01 2023, doi: 10.1364/BOE.480685.

[13] S. Jiang *et al.*, "Spatial- and Fourier-domain ptychography for high-throughput bio-imaging," *Nature Protocols,* vol. 18, no. 7, pp. 2051-2083, 2023/07/01 2023, doi: 10.1038/s41596-023-00829-4.

[14] M. Dierolf *et al.*, "Ptychographic X-ray computed tomography at the nanoscale," *Nature,* vol. 467, no. 7314, pp. 436-439, 2010/09/01 2010, doi: 10.1038/nature09419.

[15] P. J. Withers *et al.*, "X-ray computed tomography," *Nature Reviews Methods Primers,* vol. 1, no. 1, p. 18, 2021/02/25 2021, doi: 10.1038/s43586-021-00015-4.

[16] C. Zuo, J. Sun, J. Li, A. Asundi, and Q. Chen, "Wide-field high-resolution 3D microscopy with Fourier ptychographic diffraction tomography," *Optics and Lasers in Engineering,* vol. 128, p. 106003, 2020/05/01/ 2020, doi: https://doi.org/10.1016/j.optlaseng.2020.106003.

[17] A. D. Elliott, "Confocal Microscopy: Principles and Modern Practices," *Current Protocols in Cytometry,* vol. 92, no. 1, p. e68, 2020, doi: https://doi.org/10.1002/cpcy.68.

[18] A. M. Larson, "Multiphoton microscopy," *Nature Photonics,* vol. 5, no. 1, pp. 1-1, 2011/01/01 2011, doi: 10.1038/nphoton.an.2010.2.

[19] E. H. K. Stelzer *et al.*, "Light sheet fluorescence microscopy," *Nature Reviews Methods Primers,* vol. 1, no. 1, p. 73, 2021/11/03 2021, doi: 10.1038/s43586-021-00069-4.

[20] M. Stockmar *et al.*, "Near-field ptychography: phase retrieval for inline holography using a structured illumination," *Scientific Reports,* vol. 3, no. 1, p. 1927, 2013/05/31 2013, doi: 10.1038/srep01927.
[21] J. W. Goodman, *Introduction to Fourier optics*. Englewood: Roberts & Co., 2005.
[22] D. Paganin, *Coherent x-ray optics*. New York: Oxford University Press, 2006.
[23] D. G. Voelz, *Computational Fourier Optics: A MATLAB Tutorial*. Washington: Society of Photo-Optical Instrumentation Engineers, 2011.
[24] J. D. Schmidt, *Numerical simulation of optical wave propagation with examples in MATLAB*. Washington: Society of Photo-Optical Instrumentation Engineers, 2010.
[25] D. G. Voelz and M. C. Roggemann, "Digital simulation of scalar optical diffraction: revisiting chirp function sampling criteria and consequences," *Appl. Opt.,* vol. 48, no. 32, pp. 6132-6142, 2009/11/10 2009, doi: 10.1364/AO.48.006132.
[26] G. Brooker, *Modern Classical Optics*. New York: Oxford University Press, 2011.
[27] M. Born and E. Wolf, *Principles of optics: electromagnetic theory of propagation, interference and diffraction of light*, 7 ed. Cambridge: Cambridge Univ. Press, , 2006.
[28] E. Hecht, *Optics, Fourth Edition*. San Francisco: Addison, 2002.
[29] V. Friso van der and P. Franz, "Coherent x-ray scattering," *Journal of Physics: Condensed Matter,* vol. 16, no. 28, p. 5003, 2004/07/02 2004, doi: 10.1088/0953-8984/16/28/020.
[30] R. Caciuffo, S. Melone, F. Rustichelli, and A. Boeuf, "Monochromators for x-ray synchrotron radiation," *Physics Reports,* vol. 152, no. 1, pp. 1-71, 1987/08/01/ 1987, doi: https://doi.org/10.1016/0370-1573(87)90080-9.
[31] C. E. Shannon, "Communication in the Presence of Noise," *Proceedings of the IRE,* vol. 37, no. 1, pp. 10-21, 1949, doi: 10.1109/JRPROC.1949.232969.
[32] L. Mandel and E. Wolf, "Coherence Properties of Optical Fields," *Reviews of Modern Physics,* vol. 37, no. 2, pp. 231-287, 04/01/ 1965, doi: 10.1103/RevModPhys.37.231.
[33] W. Bragg, "A New Type of "X-Ray Microscope"," *Nature,* vol. 143, no. 678, 1939, doi: https://doi.org/10.1038/143678a0.
[34] H. C. K. Nugent, "Coherent lensless X-ray imaging," *Nature Photon,* vol. 4, pp. 833-839, 2010, doi: https://doi.org/10.1038/nphoton.2010.240.
[35] J. Miao, T. Ishikawa, I. K. Robinson, and M. M. Murnane, "Beyond crystallography: Diffractive imaging using coherent x-ray light sources," *Science,* vol. 348, no. 6234, pp. 530-535, 2015, doi: doi:10.1126/science.aaa1394.
[36] P. Thibault, M. Dierolf, O. Bunk, A. Menzel, and F. Pfeiffer, "Probe retrieval in ptychographic coherent diffractive imaging," *Ultramicroscopy,* vol. 109, no. 4, pp. 338-343, 2009/03/01/ 2009, doi: https://doi.org/10.1016/j.ultramic.2008.12.011.
[37] M. Kim, "Principles and techniques of digital holographic microscopy," *SPIE Reviews,* vol. 1, no. 1, p. 018005, 2010. [Online]. Available: https://doi.org/10.1117/6.0000006.
[38] M. Guizar-Sicairos and P. Thibault, "Ptychography: A solution to the phase problem," *Physics Today,* vol. 74, pp. 42-48, 09/01 2021, doi: 10.1063/PT.3.4835.
[39] W. Hoppe, "Beugung im inhomogenen Primarstrahlwellenfeld. I. Prinzip einer Phasenmessung von Elektronenbeungungsinterferenzen," *Acta Crystallographica Section A,* vol. 25, no. 4, pp. 495-501, 1969, doi: doi:10.1107/S0567739469001045.
[40] W. Hoppe and G. Strube, "Diffraction in inhomogeneous primary wave fields. 2. Optical experiments for phase determination of lattice interferences," *Acta Crystallogr. A,* vol. 25, pp. 502-507, 1969.
[41] W. Hoppe, "Diffraction in inhomogeneous primary wave fields. 3. Amplitude and phase determination for nonperiodic objects," *Acta Crystallographica Section a-Crystal Physics Diffraction Theoretical and General Crystallography,* pp. 508-&, 1969.
[42] R. Hegerl and W. Hoppe, "Dynamische Theorie der Kristallstrukturanalyse durch Elektronenbeugung im inhomogenen Primärstrahlwellenfeld," *Berichte der*

Bunsengesellschaft für physikalische Chemie, vol. 74, no. 11, pp. 1148-1154, 1970, doi: https://doi.org/10.1002/bbpc.19700741112.

[43] P. D. Nellist, B. C. McCallum, and J. M. Rodenburg, "Resolution beyond the 'information limit' in transmission electron microscopy," *Nature,* vol. 374, no. 6523, pp. 630-632, 1995/04/01 1995, doi: 10.1038/374630a0.

[44] J. M. Rodenburg, "Ptychography and Related Diffractive Imaging Methods," in *Advances in Imaging and Electron Physics*, vol. 150, Hawkes Ed.: Elsevier, 2008, pp. 87-184.

[45] R. W. Gerchberg, "A practical algorithm for the determination of phase from image and diffraction plane pictures," *Optik,* vol. 35, pp. 237-246, 1972.

[46] J. R. Fienup, "Phase retrieval algorithms: a comparison," *Appl. Opt.,* vol. 21, no. 15, pp. 2758-2769, 1982/08/01 1982, doi: 10.1364/AO.21.002758.

[47] J. R. Fienup, "Reconstruction of a complex-valued object from the modulus of its Fourier transform using a support constraint," *J. Opt. Soc. Am. A,* vol. 4, no. 1, pp. 118-123, 1987/01/01 1987, doi: 10.1364/JOSAA.4.000118.

[48] J. M. Rodenburg and H. M. L. Faulkner, "A phase retrieval algorithm for shifting illumination," *Applied Physics Letters,* vol. 85, no. 20, pp. 4795-4797, 2004, doi: 10.1063/1.1823034.

[49] M. Guizar-Sicairos and J. R. Fienup, "Phase retrieval with transverse translation diversity: a nonlinear optimization approach," *Opt. Express,* vol. 16, no. 10, pp. 7264-7278, 2008/05/12 2008, doi: 10.1364/OE.16.007264.

[50] V. Elser, I. Rankenburg, and P. Thibault, "Searching with iterated maps," *Proceedings of the National Academy of Sciences,* vol. 104, no. 2, pp. 418-423, 2007, doi: doi:10.1073/pnas.0606359104.

[51] A. M. Maiden and J. M. Rodenburg, "An improved ptychographical phase retrieval algorithm for diffractive imaging," *Ultramicroscopy,* vol. 109, no. 10, pp. 1256-1262, 2009/09/01/ 2009, doi: https://doi.org/10.1016/j.ultramic.2009.05.012.

[52] P. Thibault, M. Dierolf, A. Menzel, O. Bunk, C. David, and F. Pfeiffer, "High-Resolution Scanning X-ray Diffraction Microscopy," *Science,* vol. 321, no. 5887, pp. 379-382, 2008, doi: doi:10.1126/science.1158573.

[53] G. Zheng, R. Horstmeyer, and C. Yang, "Wide-field, high-resolution Fourier ptychographic microscopy," *Nature Photonics,* vol. 7, no. 9, pp. 739-745, 2013/09/01 2013, doi: 10.1038/nphoton.2013.187.

[54] Y. Jiang *et al.*, "Electron ptychography of 2D materials to deep sub-ångström resolution," (in eng), *Nature,* vol. 559, no. 7714, pp. 343-349, Jul 2018, doi: 10.1038/s41586-018-0298-5.

[55] K. X. Nguyen *et al.*, "Achieving sub-0.5-angstrom–resolution ptychography in an uncorrected electron microscope," *Science,* vol. 383, no. 6685, pp. 865-870, 2024, doi: doi:10.1126/science.adl2029.

[56] S. Jiang *et al.*, "Wide-field, high-resolution lensless on-chip microscopy via near-field blind ptychographic modulation," *Lab on a Chip,* 10.1039/C9LC01027K vol. 20, no. 6, pp. 1058-1065, 2020, doi: 10.1039/C9LC01027K.

[57] S. Jiang *et al.*, "Resolution-Enhanced Parallel Coded Ptychography for High-Throughput Optical Imaging," *ACS Photonics,* vol. 8, no. 11, pp. 3261-3271, 2021/11/17 2021, doi: 10.1021/acsphotonics.1c01085.

[58] A. M. Maiden, J. M. Rodenburg, and M. J. Humphry, "Optical ptychography: a practical implementation with useful resolution," *Opt. Lett.,* vol. 35, no. 15, pp. 2585-2587, 2010/08/01 2010, doi: 10.1364/OL.35.002585.

[59] P. Song *et al.*, "Super-resolution microscopy via ptychographic structured modulation of a diffuser," *Opt. Lett.,* vol. 44, no. 15, pp. 3645-3648, 2019/08/01 2019, doi: 10.1364/OL.44.003645.

[60] A. Maiden, J. M. Rodenburg, and M. J. Humphry, "A new method of high resolution, quantitative phase scanning microscopy," *Scanning Microscopy 2010,* vol. 7729, pp. 313-320, 2010/06/02 2010, doi: 10.1117/12.853339.

[61] S. McDermott and A. Maiden, "Near-field ptychographic microscope for quantitative phase imaging," *Opt. Express,* vol. 26, no. 19, pp. 25471-25480, 2018/09/17 2018, doi: 10.1364/OE.26.025471.
[62] X. Ou, R. Horstmeyer, C. Yang, and G. Zheng, "Quantitative phase imaging via Fourier ptychographic microscopy," *Opt. Lett.,* vol. 38, no. 22, pp. 4845-4848, 2013/11/15 2013, doi: 10.1364/OL.38.004845.
[63] L. Tian, X. Li, K. Ramchandran, and L. Waller, "Multiplexed coded illumination for Fourier Ptychography with an LED array microscope," *Biomed. Opt. Express,* vol. 5, no. 7, pp. 2376-2389, 2014/07/01 2014, doi: 10.1364/BOE.5.002376.
[64] D. R. Luke, "Relaxed averaged alternating reflections for diffraction imaging," *Inverse Problems,* vol. 21, no. 1, p. 37, 2004/11/09 2005, doi: 10.1088/0266-5611/21/1/004.
[65] S. Boyd, N. Parikh, E. Chu, B. Peleato, and J. Eckstein, "Distributed Optimization and Statistical Learning via the Alternating Direction Method of Multipliers," *Foundations and Trends® in Machine Learning,* vol. 3, no. 1, pp. 1-122, 2011, doi: 10.1561/2200000016.
[66] P. Thibault and M. Guizar-Sicairos, "Maximum-likelihood refinement for coherent diffractive imaging," *New Journal of Physics,* vol. 14, no. 6, p. 063004, 2012/06/07 2012, doi: 10.1088/1367-2630/14/6/063004.
[67] A. Maiden, D. Johnson, and P. Li, "Further improvements to the ptychographical iterative engine," *Optica,* vol. 4, no. 7, pp. 736-745, 2017/07/20 2017, doi: 10.1364/OPTICA.4.000736.
[68] A. M. Maiden, W. Mei, and P. Li, "WASP: weighted average of sequential projections for ptychographic phase retrieval," *Opt. Express,* vol. 32, no. 12, pp. 21327-21344, 2024/06/03 2024, doi: 10.1364/OE.516946.
[69] A. M. Maiden, M. J. Humphry, M. C. Sarahan, B. Kraus, and J. M. Rodenburg, "An annealing algorithm to correct positioning errors in ptychography," *Ultramicroscopy,* vol. 120, pp. 64-72, 2012/09/01/ 2012, doi: https://doi.org/10.1016/j.ultramic.2012.06.001.
[70] P. Thibault and A. Menzel, "Reconstructing state mixtures from diffraction measurements," *Nature,* vol. 494, no. 7435, pp. 68-71, 2013/02/01 2013, doi: 10.1038/nature11806.
[71] P. Li, T. Edo, D. Batey, J. Rodenburg, and A. Maiden, "Breaking ambiguities in mixed state ptychography," *Opt. Express,* vol. 24, no. 8, pp. 9038-9052, 2016/04/18 2016, doi: 10.1364/OE.24.009038.
[72] Z. Chen *et al.*, "Mixed-state electron ptychography enables sub-angstrom resolution imaging with picometer precision at low dose," *Nature Communications,* vol. 11, no. 1, p. 2994, 2020/06/12 2020, doi: 10.1038/s41467-020-16688-6.
[73] M. Stockmar *et al.*, "X-Ray Near-Field Ptychography for Optically Thick Specimens," *Physical Review Applied,* vol. 3, no. 1, p. 014005, 01/21/ 2015, doi: 10.1103/PhysRevApplied.3.014005.
[74] R. M. Clare, M. Stockmar, M. Dierolf, I. Zanette, and F. Pfeiffer, "Characterization of near-field ptychography," *Opt. Express,* vol. 23, no. 15, pp. 19728-19742, 2015/07/27 2015, doi: 10.1364/OE.23.019728.
[75] Y. Zhang, Z. Zhang, and A. Maiden, "Ptycho-cam: a ptychographic phase imaging add-on for opticalmicroscopy," *Appl. Opt.,* vol. 61, no. 10, pp. 2874-2880, 2022/04/01 2022, doi: 10.1364/AO.452835.
[76] H. Zhang *et al.*, "Near-field Fourier ptychography: super-resolution phase retrieval via speckle illumination," *Opt. Express,* vol. 27, no. 5, pp. 7498-7512, 2019/03/04 2019, doi: 10.1364/OE.27.007498.
[77] A. M. Maiden, M. C. Sarahan, M. D. Stagg, S. M. Schramm, and M. J. Humphry, "Quantitative electron phase imaging with high sensitivity and an unlimited field of view," *Scientific Reports,* vol. 5, no. 1, p. 14690, 2015/10/01 2015, doi: 10.1038/srep14690.
[78] F. Allars, P.-H. Lu, M. Kruth, R. E. Dunin-Borkowski, J. M. Rodenburg, and A. M. Maiden, "Efficient large field of view electron phase imaging using near-field electron ptychography

with a diffuser," *Ultramicroscopy,* vol. 231, p. 113257, 2021/12/01/ 2021, doi: https://doi.org/10.1016/j.ultramic.2021.113257.
[79] S. You, P.-H. Lu, T. Schachinger, A. Kovács, R. E. Dunin-Borkowski, and A. M. Maiden, "Lorentz near-field electron ptychography," *Applied Physics Letters,* vol. 123, no. 19, 2023, doi: 10.1063/5.0169788.
[80] X. Huang, H. Yan, R. Harder, Y. Hwu, I. K. Robinson, and Y. S. Chu, "Optimization of overlap uniformness for ptychography," *Opt. Express,* vol. 22, no. 10, pp. 12634-12644, 2014/05/19 2014, doi: 10.1364/OE.22.012634.
[81] M. Dierolf *et al.*, "Ptychographic coherent diffractive imaging of weakly scattering specimens," *New Journal of Physics,* vol. 12, no. 3, p. 035017, 2010/03/31 2010, doi: 10.1088/1367-2630/12/3/035017.
[82] S. Liu *et al.*, "Periodic Artifacts Generation and Suppression in X-ray Ptychography," *Photonics,* vol. 10, no. 5, p. 532, 2023. [Online]. Available: https://www.mdpi.com/2304-6732/10/5/532.
[83] O. Bunk, M. Dierolf, S. Kynde, I. Johnson, O. Marti, and F. Pfeiffer, "Influence of the overlap parameter on the convergence of the ptychographical iterative engine," *Ultramicroscopy,* vol. 108, no. 5, pp. 481-487, 2008/04/01/ 2008, doi: https://doi.org/10.1016/j.ultramic.2007.08.003.
[84] Z. Hu, "Step Size Influence on Defocused Beam Ptychography," in *Imaging and Applied Optics Congress 2022 (3D, AOA, COSI, ISA, pcAOP)*, Vancouver, British Columbia, 2022/07/11 2022: Optica Publishing Group, in Technical Digest Series, p. CTh3C.3, doi: 10.1364/COSI.2022.CTh3C.3. [Online]. Available: https://opg.optica.org/abstract.cfm?URI=COSI-2022-CTh3C.3
[85] E. R. Shanblatt *et al.*, "Forward model for propagation-based x-ray phase contrast imaging in parallel- and cone-beam geometry," *Opt. Express,* vol. 27, no. 4, pp. 4504-4521, 2019/02/18 2019, doi: 10.1364/OE.27.004504.
[86] R. Horstmeyer, J. Chung, X. Ou, G. Zheng, and C. Yang, "Diffraction tomography with Fourier ptychography," *Optica,* vol. 3, no. 8, pp. 827-835, 2016/08/20 2016, doi: 10.1364/OPTICA.3.000827.
[87] V. S. C. Kuppili *et al.*, "Ptychotomography at DLS Coherence Beamline I13," *Journal of Physics: Conference Series,* vol. 849, no. 1, p. 012031, 2017/06/01 2017, doi: 10.1088/1742-6596/849/1/012031.
[88] J. M. Cowley and A. F. Moodie, "The scattering of electrons by atoms and crystals. I. A new theoretical approach," *Acta Crystallographica,* vol. 10, pp. 609-619, 1957.
[89] J. M. Cowley, "CHAPTER 11 - Multi-slice approaches," in *Diffraction Physics (Third Edition)*, J. M. Cowley Ed. Amsterdam: North-Holland, 1995, pp. 231-254.
[90] T. M. Godden, R. Suman, M. J. Humphry, J. M. Rodenburg, and A. M. Maiden, "Ptychographic microscope for three-dimensional imaging," *Opt. Express,* vol. 22, no. 10, pp. 12513-12523, 2014/05/19 2014, doi: 10.1364/OE.22.012513.
[91] S. Chowdhury *et al.*, "High-resolution 3D refractive index microscopy of multiple-scattering samples from intensity images," *Optica,* vol. 6, no. 9, pp. 1211-1219, 2019/09/20 2019, doi: 10.1364/OPTICA.6.001211.
[92] E. H. R. Tsai, I. Usov, A. Diaz, A. Menzel, and M. Guizar-Sicairos, "X-ray ptychography with extended depth of field," *Opt. Express,* vol. 24, no. 25, pp. 29089-29108, 2016/12/12 2016, doi: 10.1364/OE.24.029089.
[93] S. Gao *et al.*, "Electron ptychographic microscopy for three-dimensional imaging," *Nature Communications,* vol. 8, no. 1, p. 163, 2017/07/31 2017, doi: 10.1038/s41467-017-00150-1.
[94] M. Chen, D. Ren, H.-Y. Liu, S. Chowdhury, and L. Waller, "Multi-layer Born multiple-scattering model for 3D phase microscopy," *Optica,* vol. 7, no. 5, pp. 394-403, 2020/05/20 2020, doi: 10.1364/OPTICA.383030.

[95] M. Holler *et al.*, "X-ray ptychographic computed tomography at 16 nm isotropic 3D resolution," *Scientific Reports,* vol. 4, no. 1, p. 3857, 2014/01/24 2014, doi: 10.1038/srep03857.
[96] P. Li and A. Maiden, "Optical ptychography with extended depth of field," *Journal of Physics: Conference Series,* vol. 902, no. 1, p. 012015, 2017/09/01 2017, doi: 10.1088/1742-6596/902/1/012015.
[97] M. Stockmar *et al.*, "X-ray nanotomography using near-field ptychography," *Opt. Express,* vol. 23, no. 10, pp. 12720-12731, 2015/05/18 2015, doi: 10.1364/OE.23.012720.
[98] M. Du, Z. Di, D. Gursoy, R. P. Xian, Y. Kozorovitskiy, and C. Jacobsen, "Upscaling X-ray nanoimaging to macroscopic specimens," *Journal of Applied Crystallography,* vol. 54, no. 2, pp. 386-401, 2021, doi: doi:10.1107/S1600576721000194.
[99] S. H. Shahmoradian *et al.*, "Three-Dimensional Imaging of Biological Tissue by Cryo X-Ray Ptychography," *Scientific Reports,* vol. 7, no. 1, p. 6291, 2017/07/24 2017, doi: 10.1038/s41598-017-05587-4.
[100] C. Bosch *et al.*, "Functional and multiscale 3D structural investigation of brain tissue through correlative in vivo physiology, synchrotron microtomography and volume electron microscopy," *Nature Communications,* vol. 13, no. 1, p. 2923, 2022/05/25 2022, doi: 10.1038/s41467-022-30199-6.
[101] H. Öztürk *et al.*, "Multi-slice ptychography with large numerical aperture multilayer Laue lenses," *Optica,* vol. 5, no. 5, pp. 601-607, 2018/05/20 2018, doi: 10.1364/OPTICA.5.000601.
[102] C. Rau, "Imaging with Coherent Synchrotron Radiation: X-ray Imaging and Coherence Beamline (I13) at Diamond Light Source," *Synchrotron Radiation News,* vol. 30, no. 5, pp. 19-25, 2017/09/03 2017, doi: 10.1080/08940886.2017.1364530.
[103] K. C. Lee, K. Lee, J. Jung, S. H. Lee, D. Kim, and S. A. Lee, "A Smartphone-Based Fourier Ptychographic Microscope Using the Display Screen for Illumination," *ACS Photonics,* vol. 8, no. 5, pp. 1307-1315, 2021/05/19 2021, doi: 10.1021/acsphotonics.1c00350.
[104] S. Jiang *et al.*, "Wide-field, high-resolution lensless on-chip microscopy via near-field blind ptychographic modulation," *Lab on a chip,* 2019.
[105] Z. Hu, Y. Zhang, P. Li, D. Batey, and A. Maiden, "Near-field multi-slice ptychography: quantitative phase imaging of optically thick samples with visible light and X-rays," *Opt. Express,* vol. 31, no. 10, pp. 15791-15809, 2023/05/08 2023, doi: 10.1364/OE.487002.
[106] C. T. Putkunz *et al.*, "Phase-Diverse Coherent Diffractive Imaging: High Sensitivity with Low Dose," *Physical Review Letters,* vol. 106, no. 1, p. 013903, 01/07/ 2011, doi: 10.1103/PhysRevLett.106.013903.
[107] M. Guizar-Sicairos, M. Holler, A. Diaz, J. Vila-Comamala, O. Bunk, and A. Menzel, "Role of the illumination spatial-frequency spectrum for ptychography," *Physical Review B,* vol. 86, no. 10, p. 100103, 09/24/ 2012, doi: 10.1103/PhysRevB.86.100103.
[108] B. C. McCallum and J. M. Rodenburg, "Two-dimensional demonstration of Wigner phase-retrieval microscopy in the STEM configuration," *Ultramicroscopy,* vol. 45, no. 3, pp. 371-380, 1992/11/01/ 1992, doi: https://doi.org/10.1016/0304-3991(92)90149-E.
[109] P. Li and A. Maiden, "Multi-slice ptychographic tomography," *Scientific Reports,* vol. 8, no. 1, p. 2049, 2018/02/01 2018, doi: 10.1038/s41598-018-20530-x.